# Ultrafast imaging of Bessel beam generated nano-plasmas within dielectrics

Mostafa Hassan

**THÈSE DE DOCTORAT DE L'ÉTABLISSEMENT UNIVERSITÉ BOURGOGNE FRANCHE-COMTÉ**

**PRÉPARÉE À L'UNIVERSITÉ DE BOURGOGNE FRANCHE-COMTÉ**

École doctorale n°37

Sciences Pour l'Ingénieur et Microtechniques

Doctorat d'Optique et Photonique

par

MOSTAFA HASSAN

# Ultrafast imaging of Bessel beam generated nano-plasmas within dielectrics

## Imagerie ultrarapide de nano-plasmas générés par un faisceau de Bessel dans les diélectriques

Thèse présentée et soutenue à Besançon, le 19 décembre 2022

Composition du Jury :

| | | |
|---|---|---|
| JACQUOT MAXIME | Professeur des Universités à l'Université Bourgogne Franche-Comté | Président du jury |
| BELLOUARD YVES | Professeur associé à l'École Polytechnique Fédérale de Lausanne (EPFL) | Rapporteur |
| JEDRKIEWICZ OTTAVIA | Chargée de Recherche CNR à l'Istituto di Fotonica e Nanotecnologie | Rapporteur |
| LECLER SYLVAIN | Professeur des Universités à l'INSA Strasbourg | Examinateur |
| COURVOISIER FRANÇOIS | Directeur de Recherche CNRS à l'Institut FEMTO-ST | Directeur de thèse |

école doctorale **sciences pour l'ingénieur et microtechniques**

**Title:** Ultrafast imaging of Bessel beam generated nano-plasmas within dielectrics

**Keywords:** Bessel beams, femtosecond laser, ultrafast laser ablation

**Abstract:**

Ultra-intense femtosecond lasers are widely used for nano and micro-material processing. Explaining the laser-matter interaction is needed to control the processing. In this context, non-diffracting beams, such as Bessel beams, provided substantial advantages regarding the stability of the non-linear propagation within dielectrics. They allowed the generation of extremely high aspect ratio nanovoids. However, conventional models describing Bessel-dielectric interaction fail to explain experimental observations. Therefore, this thesis aims to develop a set of techniques to retrieve the parameters of laser-generated plasmas. The first part develops an approach to shape the polarization of the Bessel beam along its propagation based on spatially-varying waveplates. The second part of this work is dedicated to the imaging of the interaction between the plasma generated by the onset of the pulse and the trailing part inside sapphire. We confirmed a generation of nano-plasma with a density exceeding the critical density, and a diameter of typically 200 nm. Then, the third part of this work focuses on imaging the plasma using a pump-probe approach. This new concept is based on shaping the probe as a higher-order Bessel beam. The plasma parameters are extracted from a set of measurements of reflectivity in amplitude and phase for different orders and angles of the probe pulse.

**Titre :** Ultrafast imaging of Bessel beam generated nano-plasmas within dielectrics

**Mots-clés :** Faisceaux de Bessel, laser femtoseconde, Ablation par impulsions ultrabrèves

**Résumé :**

Les lasers femtoseconde ultra-intense sont largement utilisés pour le traitement des matériaux à l'échelle micro et nanométrique. Dans ce contexte, il est nécessaire de contrôler l'interaction laser-matière. Les faisceaux non diffractants, tels que les faisceaux de Bessel, offrent des avantages substantiels en ce qui concerne la stabilité de la propagation non linéaire dans les diélectriques. Ils ont permis la génération de nano-vides de rapport d'aspect extrêmement élevé. Cependant, les modèles conventionnels décrivant l'interaction Bessel-diélectrique ne parviennent pas à expliquer les observations expérimentales. Par conséquent, cette thèse vise à développer un ensemble de techniques pour retrouver les paramètres des plasmas générés par laser. La première partie développe une approche pour façonner la polarisation du faisceau de Bessel le long de sa propagation grâce à des lames demi-onde variant dans l'espace. La deuxième partie de ce travail est dédiée à l'imagerie de l'interaction entre le plasma généré par le début de l'impulsion et la majeure partie de l'impulsion. Nous avons confirmé une génération de nano-plasma avec une densité dépassant la densité critique, et un diamètre de typiquement 200 nm. La troisième partie de ce travail se concentre sur l'imagerie du plasma en utilisant une approche pompe-sonde. Ce nouveau concept est basé sur la mise en forme de la sonde comme un faisceau de Bessel d'ordre supérieur. Les paramètres du plasma sont extraits d'un ensemble de mesures de réflectivité en amplitude et en phase pour différents ordres et angles de l'impulsion de la sonde.

UBFC UNIVERSITÉ BOURGOGNE FRANCHE-COMTÉ

Université Bourgogne Franche-Comté
32, avenue de l'Observatoire
25000 Besançon, France

”Much more money in the Arabian Gulf region, but life quality is better in Europe, science and progress are more in America, and family, friends, and loved ones are in a dilapidated home country whose condition we are unsatisfied.

That is how we struggle with life, we leave things for the sake of things, and we do not know which is more important, what we leave or try to realize.

Then with the passage of age, we discover that we want to realize what we have left or leave what we have realized.

Some of everything may be better than realizing some and leaving some.

However, we need contentment much more than we need the things around us.”

***Ahmed Khaled Tawfik 1962 - 2018***

# ACKNOWLEDGMENTS

During the thesis work, I met many people who have contributed directly and indirectly to the outcome of this work. Unfortunately, I cannot individually name them all in the next couple of lines. I thank first of all Yves Bellouard and Ottavia Jedrkiewicz, who agreed to review this manuscript: thank you for their patient reading and the time they devoted to my work. Thanks also to Sylvain Lecler and Maxime Jacquot for being members of my thesis jury.

François Courvoisier, I will never thank you enough for the quality of your supervision, for all knowledge you transmitted to me related to the work and daily life, for the mutual trust built with time, for your listening and patience, and finally for the friendly relationship. Thank you too much for improving my skills in general throughout the whole working period. It is always an absolute pleasure to work with you. Thank you!

I sincerely thank all my team members, who I worked with almost daily during the last three years: the experimentalists for the constructive discussions about the experimental obstacles during the group meetings. A special thanks to Remi Meyer, who built the optical setup I used during my work, for nice welcoming me, well training me, and transmitting the tips and tricks of the experimental work. Great thanks to Valeria-Viviana Belloni, who is the lab companion, for the mutual collaboration, support and advice during the work. I enjoyed working with you and I wish you good luck in writing your thesis manuscript. Also, I would like to thank Christian Vetter, Luc Froehly, Luca Furfaro, and Cyril Billet for providing technical support during the work. You have improved a lot my technical and personal skills. Thank you.

I want to thank the numerical team: Kazem Ardaneh, Remo Giust, and Pierre-Jean Charpin for giving me the knowledge and information related to the theoretical part of the work. To Valérie Fauvez, thank you very much for the perfect control of the administration procedures.

In the end, I warmly thank my family for their patience with my usual absence and keep supporting me during the three years.

Thanks to you all!

# CONTENTS

# General Introduction

Ultrafast lasers have opened the way to different fields for research and applications in chemistry, biology, material science, and physics. Recently, ultrafast lasers have been widely used in the industrial chain, especially in the field of materials processing (drilling, cutting, surface texturing) because of the highly localized interaction of the short pulses with matter. Thus, understanding the laser-matter interactions is necessary to improve several existing applications and implement new ones. The interaction of an ultrafast laser pulse with dielectric materials is a complex process involving many phenomena producing changes in the medium when the pulse energy is high enough. That change can be transient or permanent. The effect on the target materials depends on the laser parameters, such as pulse duration, polarization and power.

The high peak power creates field strength that is enough, in transparent dielectrics, to promote electrons from the valance band to the conduction band, which creates a plasma. The formed plasma is of interest because it is the way the laser pulse energy is coupled into the medium. However, it acts as an absorber and meanwhile defocuses the beam. The propagation of the intense Gaussian beams is highly nonlinear because of the sequence of self-focusing due to Kerr effect and defocusing due to the plasma formation. Non-diffracting beams like Bessel beams can undergo less distortion during the nonlinear propagation.

The advantage of the Bessel Beams has been reported in the field of ultrafast laser processing of transparent materials, they appear as an excellent mean to control the process of energy deposition: high aspect ratio nanochannels with almost uniform nanometers have been demonstrated in a single shot in our group in 2010. Since that time, our group is interested in the understanding of Bessel beam induced-nanochannel formation. Several approaches were tried to study the generated plasma. Hitherto, no model could self-constantly reproduce experimental results, which was however crucial to the development of further applications.

This thesis work is positioned experimentally to study the interactions of a femtosecond laser pulse spatially shaped into a Bessel beam, with dielectrics. The work contains two main parts: controlling the Bessel beam parameters for laser micro-processing applications and studying the generated plasma from the laser-matter interaction. The question of the control of the effective intensity is solved thanks to the Bessel beams, whose intensity profile remains stable even in the filamentation regime when the focusing angle is strong enough. On the other hand, the question of the distribution and dynamics of the plasma remained unresolved.

Our work on laser-matter interaction in the femtosecond regime in the case of Bessel beams is divided into two independent lines of work: Bessel beam polarization effect on the nanograting formation, and the laser-plasma interaction from the fundamental point of view.

Before embarking on the presentation of this thesis work, we review the state of art concerning laser-matter interaction phenomena, particularly for the femtosecond regime and the case of Bessel beams. Chapter 1 presents the main phenomena at work and plasma generation in transparent media by femtosecond pulses. We introduce Bessel beams, their properties, and the experimental methods used for their shaping. In the end, we present some applications of using Bessel beams in laser micro-machining.

In a previous work of the group, we observed a relation between the formed nanochannel transverse orientation and the incident pulse polarization. Therefore, we are interested in studying the effect of varying the Bessel beam polarization along its propagation axis on the formation process. In chapter 2, we present an effective way to control the Bessel beam polarization along the propagation as a collaboration with Matthieu Lancry from the University of Paris-Saclay. In the beginning of the chapter, we briefly show the usage of ultrafast lasers for inducing nanogratings. Then, we explain our approach by passing through the concept, detailing the experimental setup, the method used to determine polarization, and the measurements of the polarization along the propagation. Finally, we present characterization results of nanogratings written in Fused Silica by a polarized-shaped Bessel beam.

Because it is not possible to image the plasma optically, the team developed a beam sectioning technique to identify the localization of absorption via the measurement of the fluence profile of a single Bessel pulse. This was performed at pulse energy above the channel formation threshold. In parallel, previous group members modelled the nonlinear propagation of the Bessel beam within dielectrics using different approaches. One of the models showed that to achieve the same level of energy absorption, the beam is strongly defocused during propagation, which is not the case in the experimental observations. With a much more powerful and computationally-intensive model, the group showed that it is possible with a resonance absorption phenomenon because of the generation of over-critical plasma, but the numerical fluence profile predicted a shifting in the Bessel lobes not seen in the experimental profile. Therefore, chapter 3 is oriented toward the investigation of laser-plasma interaction experimentally to investigate if that incompatibility is due to technical issue or not, to answer whether the generated plasma density using a highly intense ultrafast Bessel pulse is over-critical or under-critical. We start the chapter by gathering the needed information from the literature about laser-induced plasma and laser-plasma interaction. After that, we present the method used for simulating the interaction and extracting numerical data. Then, the experimental setup is also detailed. Moreover, a comparison between the experiment and numerical results is shown.

We estimated in chapter 3 that Bessel beams with a conical angle of 26° generate plasma with a typical diameter of 200nm, which exceeds the limits of the current techniques. Therefore, for further work, we propose in the last chapter a sensitive pump-probe technique that can retrieve the generated nanoplasma parameters, in a temporal domain.

At the beginning of chapter 4, we briefly overview the current imaging techniques and their limitations. Then, we introduce the concept of the new pump-probe approach, which is based on shaping both beams spatially to detect changes in the medium on the nanoscale. The main work done in this chapter is solving the challenges we faced during the experimental work, for instance, the superposition of the two beams in time and space. We finish the chapter by presenting preliminary results obtained as proof of principle.

# 1

# STATE OF THE ART: ULTRAFAST LASERS FOR MICRO AND NANO PROCESSING

Laser processing is a crucial enabling technology for many industrial systems. Ultrafast lasers enabled a technological leap in the laser processing field due to ultra-high resolution of micro and nanofabrication [Sugioka and Cheng, 2014]. The pulse duration of ultrafast lasers range is typically from tens of femtoseconds to tens of picoseconds. Femtosecond lasers with very short pulse durations ($\leq$ 200 fs) are conventionally used in fundamental research while picosecond and sub-picosecond lasers are mainly used for industrial applications.

Thanks to the ultrashort duration of the pulse, the intensity of ultrafast lasers easily achieves several tens of PW/cm$^2$, which can induce nonlinear effects in transparent materials. Our laboratory has used Bessel beams, which is a specific beam shape that creates an extremely high aspect ratio nano-needle of laser light, to generate a high aspect ratio nanochannel in glass and sapphire with only a single pulse [Bhuyan et al., 2010].

This thesis is mainly oriented toward the processes that occur within dielectrics, such as glass, fused silica, and sapphire. Therefore, this chapter reviews the usage of ultrafast lasers in the field of laser materials processing, especially those linked to the propagation inside dielectrics. In the first section, we review the fundamentals of ultrafast laser-matter interaction. After that, Bessel beams and their properties are presented in the second section. Then, we explore applications using Bessel pulses and the outline of this work.

## 1.1/ ULTRAFAST LASERS FOR MATERIAL PROCESSING

Ultrafast lasers have provided promising advantages in the field of laser processing. The short duration of the pulses reduces the heat-affected zone around the targeted regions during the processing [Momma et al., 1996]. This feature leads to a dramatic improvement in many processing applications, such as high-precision micro-cutting of biological cells (i.e. LASIK surgery [Dausinger et al., 2004]), tissues [Yanik et al., 2004], and more hard materials such as semiconductors [Bärsch et al., 2003] and steel [Chichkov et al., 1996]. Moreover, the high peak power reached in ultrafast laser pulses

allows for ionizing the bulk of transparent materials, which makes possible internal processing without modifying the surfaces. Depending on the pulse energy, ultrafast lasers can induce different kinds of modifications within dielectrics, for instance, waveguides with low powers [Davis et al., 1996], nanogratings [Florea and Winick, 2003] and voids [Juodkazis et al., 2006] using higher power. In this subsection, we briefly review laser processing applications.

### 1.1.1/ LASER DRILLING

As mentioned in the introduction of this section, ultrafast lasers reduce the formation of the heat-affected zone during the ablation process. The laser ablation process involves a long sequence of different physical phenomena: the laser pulse energy is coupled into the medium via ionization and/or free electron excitation (we will explain the process in detail further). Rethfeld et al. have reported that the choice of the pulse duration is an important parameter, conditioning the energy transfer mechanisms between the pulse and the medium and the type of transitions within the material [Rethfeld et al., 2017]. As shown in figure 1.1, the ablation behaves differently in the metal (steel) for different pulse durations. We can see that reducing the pulse duration reduces the material melting defect around the processing region.

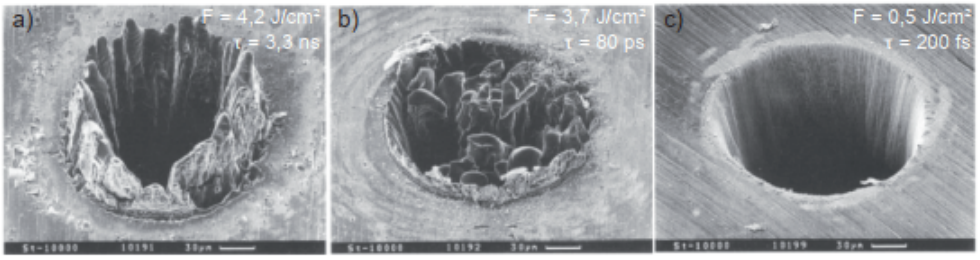


Figure 1.1: Comparison of machining in steel by a 780 nm laser, with pulse durations varying between (a) 3.3 ns, (b) 80 ps, and (c) 200 fs ($10^4$ pulses in each case). The femtosecond case shows the absence of melt and a restricted region around the crater where the material is modified compared to the other two cases. Figure from [Chichkov et al., 1996].

### 1.1.2/ SURFACE STRUCTURING

Different research works have shown ultrafast laser ability to texture material surfaces [Sakabe et al., 2009]. The laser parameters, such as the beam's profile and intensity, control the formation of various textures on the micro and nanoscale. One of the well-known textured structures is periodic surface ripple [Emmony et al., 1973]. These structures are usually caused by the interference of the incident laser beam with the scattered one on surface defects. The generated ripples are oriented perpendicular or parallel to the beam polarization depending on the intensity regime. The periodicity spacing is given by $\lambda/n(1 \pm \sin\theta)$, where $\lambda$ is the laser wavelength, $n$ is the material refractive index, and $\theta$ is the incident light angle [Jain et al., 1981].

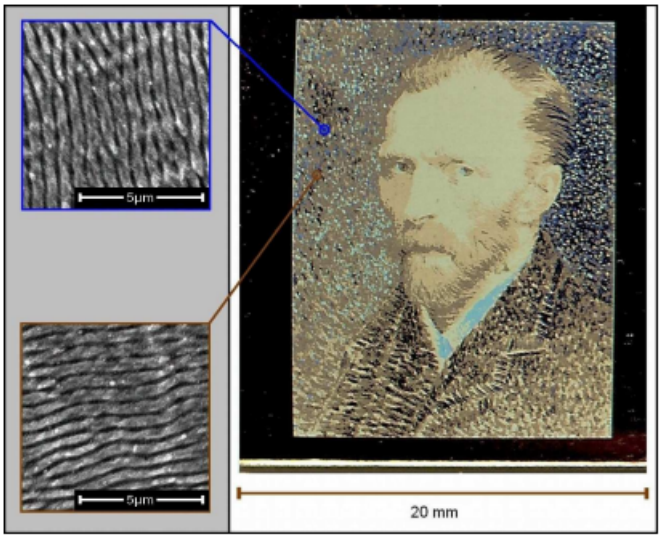


Figure 1.2: An example of controlled-orientation nanostructures written by femtosecond laser on a stainless steel sample. Figure from [Dusser et al., 2010].

### 1.1.3/ INTERNAL STRUCTURING WITHIN DIELECTRICS

At the region of focus of high-focusing optical elements, the laser pulse becomes exceptionally intense, inducing nonlinear interactions between the laser and the medium. That makes it possible to transfer the pulse energy into transparent materials and modify its characteristics. Three types of modifications have been observed, as shown in figure 1.3: (a) index modification, (b) voids by micro-explosions, and (c) crystalline modification. In 1996, Davis et al. reported the ability to modify the glass's refractive index for writing waveguides using an ultrashort pulse [Davis et al., 1996]. In comparison, Juodkazis et al. observed an opening void within a bulk of Sapphire due to micro-explosions induced by higher pulse energy [Juodkazis et al., 2006]. In contrast, by controlling the polarization, a low-density periodic structure aligned perpendicular to the laser polarization direction has been revealed in backscattering measurements [Shimotsuma et al., 2003]. Nevertheless, these modifications are directly linked to the laser parameters, such as pulse energy and duration, wavelength, polarization direction and laser repetition rate.

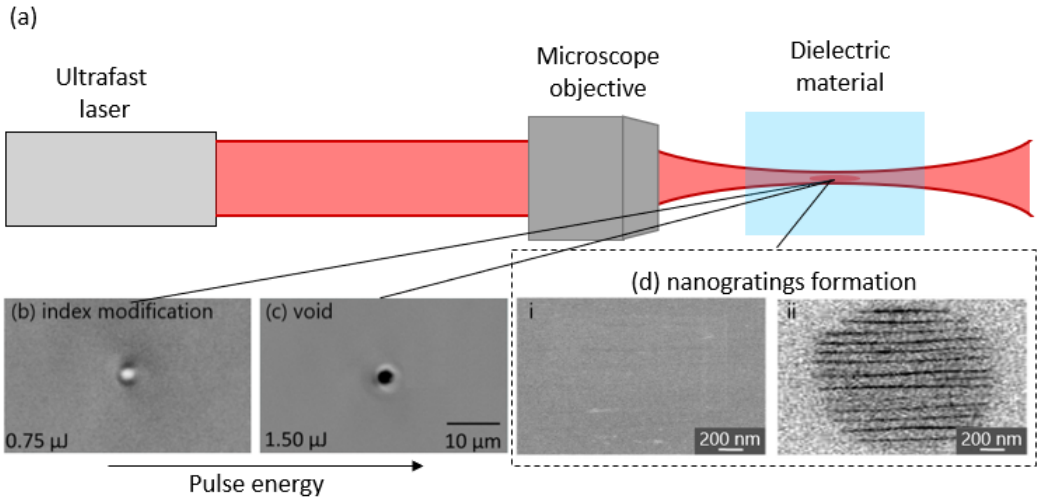


Figure 1.3: Internal structuring within dielectrics. (a) concept scheme, (b-d.i) SEM images, (b-c) Increasing the pulse energy to occur voids, Figures from [Hernandez-Rueda et al., 2017], (b) index modification, (c) void, (d) nanogratings formation that is made usually using the accumulation of pulses, Figures from [Shimotsuma et al., 2003], (d.i) secondary electron image, and (d.ii) backscattering electron image.

## 1.2/ ULTRAFAST LASER-MATTER INTERACTIONS

We have seen that the transformation of the material highly depends on the pulse energy that is absorbed. Therefore, understanding the interaction of ultrafast laser and matter is critical to control the energy deposition inside the materials. This section will briefly review the main phenomena occurring when an intense ultrafast laser pulse propagates within a dielectric material.

### 1.2.1/ PHOTOIONIZATION

Photoionization is the process of exciting an electron from the valence band to the conduction band by absorption of photons. The bandgap energy $E_g$ in dielectrics is much higher than the single-photon absorbed energy $\hbar\omega \ll E_g$. Thanks to the laser's high intensity, a simultaneous absorption of multiples photons makes it possible to excite an electron from the valence band to the conduction band with an absorption rate $\sigma I^m$ where m is the smallest number of the absorbed photons to occur the excitation, $m\hbar\omega \geqslant E_g$ as shown in (fig.1.4a). The excited free-electron in the conduction band may absorb additional photons as in (fig.1.4b), due to collisional processes (3-body interaction e-photon-phonon), and reach a higher energy state. If the electron energy exceeds typically twice the bandgap energy, it can ionize another electron from the valance band. This absorption is called impact ionization (fig.1.4c) [Couairon and Mysyrowicz, 2007]. Moreover, it can lead to avalanche ionization when the pulse duration is sufficiently long so that the process of nonlinear ionization, free-electron excitation and impact ionization, can repeat[Vogel et al., 2008].

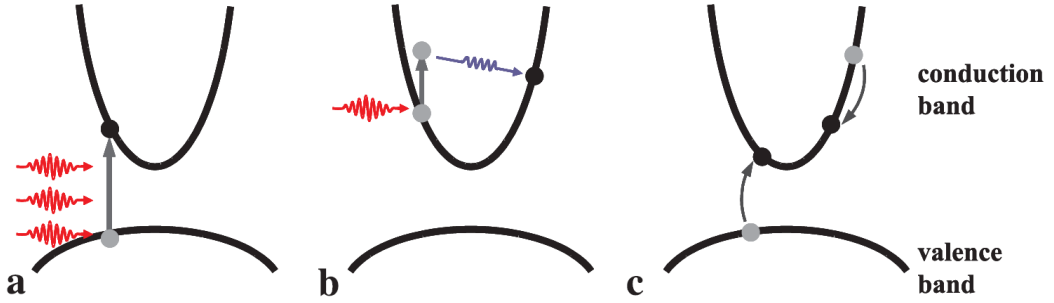


Figure 1.4: Photoionization phenomena of a) multiphoton ionization, b) free carrier absorption, and c) avalanche ionization. Figure from[Mao et al., 2004].

### 1.2.2/ NONLINEAR PROPAGATION

Several nonlinear phenomena occur when an ultrafast laser pulse propagates inside a transparent material. We can understand the nonlinear interaction by studying the response of the medium.
The propagation equation is written as [Couairon et al., 2011]:

$$\nabla \times (\nabla \times \mathbf{E}) + \frac{1}{c^2}\frac{\partial^2 \mathbf{E}}{\partial t^2} = -\mu_0 \frac{\partial^2 \mathbf{P}}{\partial t^2} \tag{1.1}$$

where $\mathbf{P}$ is the polarization of the medium, and it contains the complete information about the response of the medium while:

$$\mathbf{P} = \epsilon_0 \chi \mathbf{E} \tag{1.2}$$

The polarization $\mathbf{P}$ is usually written as a Taylor expansion to identify its different orders:

$$\mathbf{P} = \epsilon_0 \chi^{(1)}\mathbf{E} + \epsilon_0 \chi^{(2)}\mathbf{E}\mathbf{E} + \epsilon_0 \chi^{(3)}\mathbf{E}\mathbf{E}\mathbf{E} + ...$$

where $\chi$ is the susceptibility of the medium, and the index of refraction is $n = \sqrt{1+\chi}$. In this section, I will present some of these phenomena.

#### 1.2.2.1/ KERR SELF-FOCUSING

The Kerr effect can be physically interpreted as the deformation of the electronic clouds of the medium by the electromagnetic field $\mathbf{E}$ [Kelley, 1965]. In the center-symmetric materials, such as fused silica and sapphire, $\chi^{(2)} = 0$ and the first non-linear term is a contribution related to $\chi^{(3)}$:

$$\mathbf{P} \simeq \epsilon_0 \chi^{(1)}\mathbf{E} + \frac{3}{4}\epsilon_0 \chi^{(3)}\mathbf{E}^3$$

or,

$$\mathbf{P} \simeq \epsilon_0 \left(\chi^{(1)} + \frac{3}{4}\chi^{(3)}\mathbf{E}^2\right)\mathbf{E}$$

This equation seems as Eq. 1.2 with a different susceptibility term. The susceptibility here is a non-linear term that depends on the square of the amplitude of the field.

$$\chi = \chi_{LIN} + \chi_{NL} = \chi^{(1)} + \frac{3}{4}\chi^{(3)}\mathbf{E}^2$$

and since:

$$n = \sqrt{1+\chi} = \sqrt{1 + \chi^{(1)} + \frac{3}{4}\chi^{(3)}\mathbf{E}^2}$$

which means that the refractive index of a material $n$ becomes dependent on the laser intensity $I$.

$$n = n_0 + n_2 I \tag{1.3}$$

where $n_0$ is the linear refractive index, $n_2 = 3\chi^{(3)}/8n_0$ is the nonlinear refractive index, and $I = |\mathbf{E}|^2$ is the laser intensity. From Eq. 1.3, the refractive index $n$ increases if $n_2 > 0$ which means that the material will act as a focusing lens leading to an increase of the beam intensity [Hora, 1986].

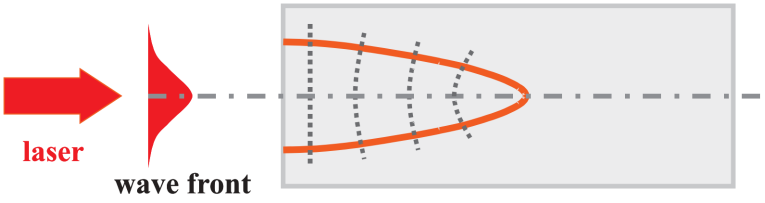


Figure 1.5: Self-focusing effect phenomenon. Figure from [Mao et al., 2004].

#### 1.2.2.2/ PLASMA SELF-DEFOCUSING

The nonlinear ionization effect occurs because of the very high intensity. This process generates electron-hole plasma. The presence of plasma decreases the refractive index. When $\omega_p/\omega \ll n_0$, the refractive index can be written as follows [Shen, 1975]:

$$n = n_0 - \frac{N}{2n_0 N_c} \tag{1.4}$$

where $N$ is the laser-generated plasma density, and $N_c = \omega^2 \epsilon_0 m^*/e^2$ is the critical plasma density when the plasma frequency equals to the laser frequency. The new refractive index profile acts as a diverging lens and the beam starts defocusing on the propagation axis.

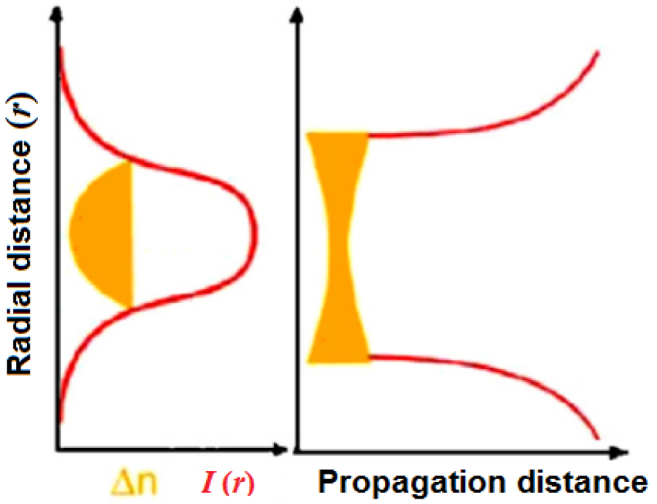


Figure 1.6: Self-defocusing phenomenon. Figure from [Couairon and Mysyrowicz, 2007].

### 1.2.3/ FILAMENTATION

#### 1.2.3.1/ DEFINITION

In the experiments, a transverse light formed along with the nonlinear propagation, called filamentation [Shen, 1975]. This observation has opened new applied research areas because the filament is formed by the sequence between nonlinear self-focusing and self-defocusing, as shown in figure 1.7. Thus, the filaments give typical order of magnitude of intensities and the generated plasma density in the case of air and gases and the case of transparent solids.

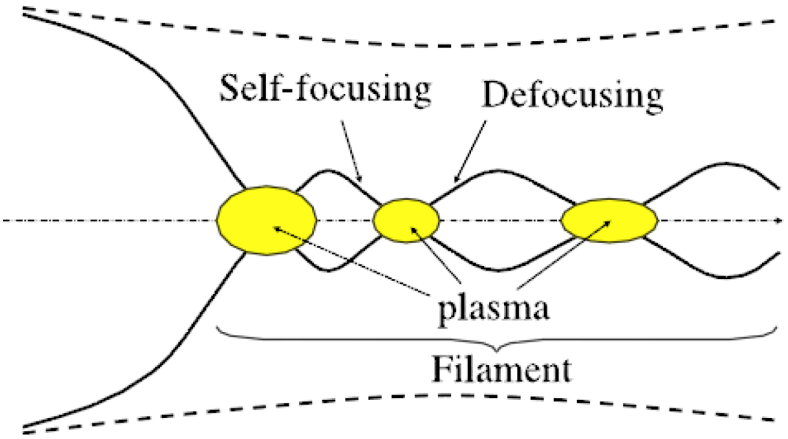


Figure 1.7: Filamentation phenomenon occurred by a cycle of nonlinear focusing and defocusing effects. Figure from [Couairon and Mysyrowicz, 2007].

#### 1.2.3.2/ FILAMENT IN SOLIDS

The femtosecond laser technology has provided longer filament lengths due to confining a significant amount of energy in an ultrashort time frame. In 1995, a study on the nonlinear propagation of a 50 mJ, 200 fs laser pulse in the air reported that laser pulses could remain transversely localized in space for a distance longer than 20 m [Braun et al., 1995]. Another experiment showed the possibility of forming a 2 km filament in the air [Couairon and Mysyrowicz, 2007]. Filamentation is also possible in liquids and solids. A French team created a 2 cm filament inside a dielectric material by using a 2 $\mu$J 160 fs Gaussian beam in fused Silica [Tzortzakis et al., 2001]. Tzortzakis et al. used a femtosecond laser source with a central wavelength $\lambda = 800$ nm focused by a lens with $f = 80mm$ as shown in (fig.1.8a). A self-guided light channel has formed over a distance exceeding 10 mm (fig.1.8c).

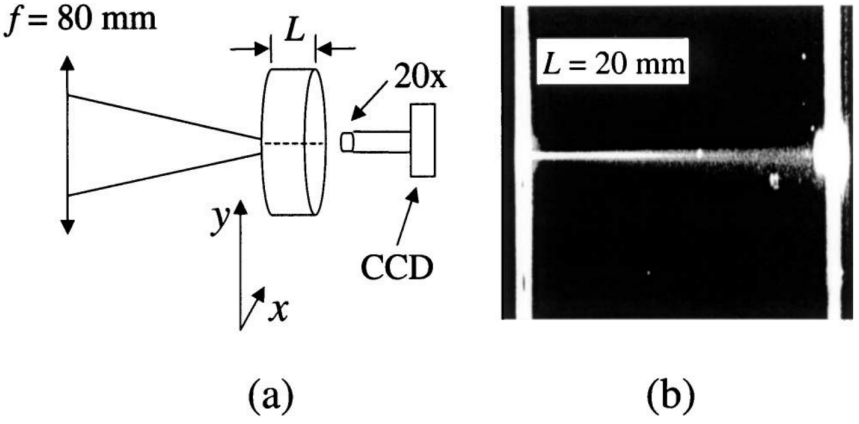


Figure 1.8: Forming self-guided filaments in fused silica with thickness L (a) scheme of the used setup and (b) A transverse photograph of the filament. Figure from [Tzortzakis et al., 2001].

.

Many models describe the light filaments [Couairon et al., 2011]. The nonlinear propagation equation, Eq.1.5, is usually used for numerical simulation to model the nonlinear propagation. Our group also used this model to describe the laser-matter interaction within solids, and we will see this model's limits later in the simulations of our particular setup.

$$\frac{\partial A}{\partial z} = \frac{i}{2k}\nabla_{\perp}^2 A - i\frac{k^{(2)}}{2}\frac{\partial^2 A}{\partial t^2} + [N_{Kerr}(|A^2|) + N_{PI}(|A^2|) + N_{Plasma}(\rho)]A \tag{1.5}$$

Eq.1.5 describes the propagation of the envelope $A$ whether in gases, transparent liquids or solids. The diffraction is accounted for as a linear effect by the term in $\nabla_{\perp}^2$. The nonlinear effects are taken into account and notationed as Kerr non-linearity $N_{Kerr}$, photoionization $N_{PI}$, and laser-induced plasma $N_{Plasma}$ where $\rho$ is the plasma density.
Eq.1.5 has to be solved together with a plasma-make equation:

$$\frac{\partial \rho}{\partial t} = [W_{PI} + W_{ava}\rho](1 - \frac{\rho}{\rho_{at}}) - \frac{\rho}{\tau_r} \tag{1.6}$$

where $W_{ava}$ is the avalanche ionization and $\tau_r$ is the relaxation time of the free-electron.

As an example, figure 1.9 shows filaments generated along the propagation axis of a focused Gaussian beam inside fused silica. As we can see in figure 1.8 (a), the length of the filament is much larger than its transverse diameter. Moreover, the filamentation highly transforms the pulse in space and time. As shown in figure 1.9 (b), this phenomenon is highly nonlinear, and a weak perturbation significantly impacts the final density distribution of the plasma in space. Thus, it is difficult to predict. As we will see later, non-diffracting beams, such as Bessel beams, are beneficial to use instead [Polesana et al., 2008].

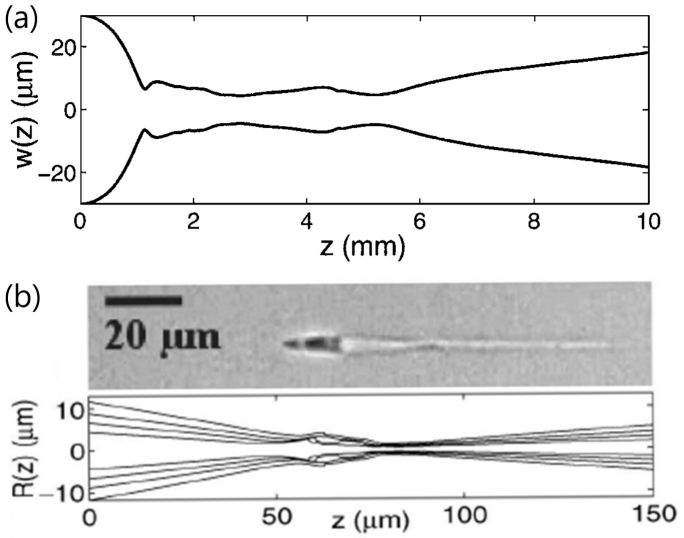


Figure 1.9: Focused Gaussian beam generates filament along its propagation inside fused silica. (a) calculated filament [Tzortzakis et al., 2001]. (b) demonstration of the distortion induced due to the filamentation [Sudrie et al., 2002].

#### 1.2.3.3/ FILAMENTS USAGE FOR MATERIAL PROCESSING

There is a wide range of applications based on filamentation, such as THz radiation[Bitman et al., 2012], light detection and ranging (LIDAR) [Iwasaki et al., 2003], controlled electric discharge [Clerici et al., 2015], plasma waveguide [Durfee et al., 1995], and laser machining [Tzortzakis et al., 2001]. In this thesis work, we mainly focus on the laser applications in the laser processing of glass.

In transparent materials, the Kerr effect is a thousand times higher than the one in air, and the density of the material is three orders of magnitude higher leading to the generation of plasmas that are much denser in solids in comparison with gases. The diameter of the plasma channel generated in the dielectrics is typically 10% of the plasma diameter in the air. Therefore, the filament's length in dielectrics is on the millimetre scale with a diameter of typically 1-10 $\mu$m [Couairon and Mysyrowicz, 2007].

The filamentation formed in glass is demonstrated for a wide range of laser wavelengths from infrared IR to ultraviolet UV [Tzortzakis et al., 2006]. Karimelahi et al. have reported that reducing the wavelength generates higher plasma density and shorter filament length by comparing the results obtained by IR and green wavelengths [Karimelahi et al., 2013].

In the filamentation regime, several modifications were induced in dielectrics using Gaussian ultrafast pulses. In figure 1.10, we briefly present examples of these modifications from the literature. The modified structures in figure 1.10 (i.e. elongated voids, microchannels, and series of voids) are not explainable by the Gaussian beam propagation alone. The pulse propagates in a nonlinear regime. The generated filament seems responsible for reshaping the beam and forming these unexpected structures [Luo et al., 2001].

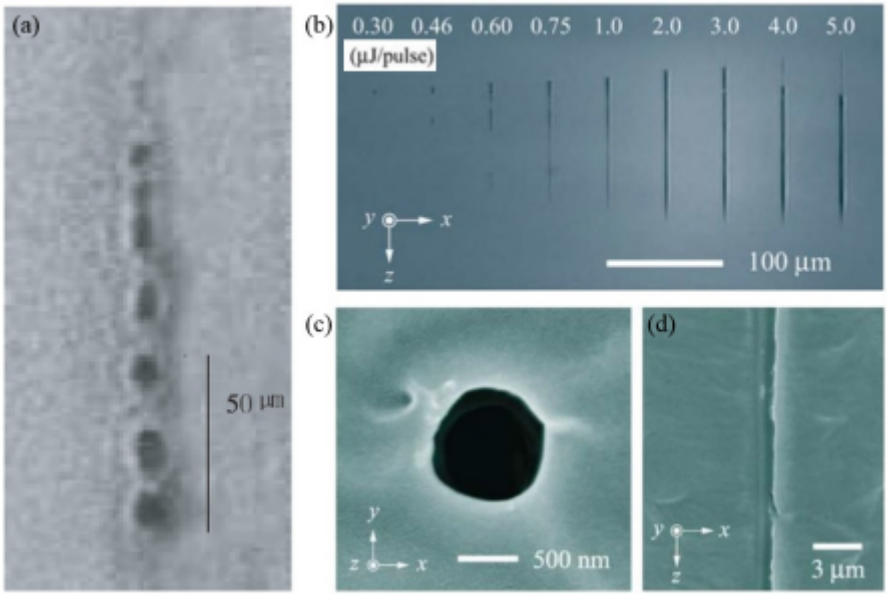


Figure 1.10: Modifications induced in dielectrics by filaments of Gaussian ultrafast pulses. (a) Series of non-periodic voids created in fused silica glass [Luo et al., 2001]. (b-d) Channels within PMMA [Sowa et al., 2005] (b) Set of channels using different pulse energies. (c-d) SEM images of the 2 $\mu$J channel in PMMA. (c) transverse view, while (d) the longitudinal view.

## 1.3/ Non-diffracting Bessel beams

Although Gaussian beams are widely used for laser micro-nano structuring, beam shaping provided new features and opportunities [Sanner et al., 2007]. We aim to study the Bessel beam's interactions with dielectrics because of their invariant intensity distribution in order to improve the use of such beams in laser machining.

### 1.3.1/ Definition

The Bessel beam is a non-diffracting beam. It is a cylindrically-symmetric interference field that occurs by applying a conical phase to a plane wave. In the 1980s, Durnin demonstrated that the Bessel beam is a solution to the Helmholtz equation that is characterized by an invariant intensity profile. This profile is characterized by an intense central core, surrounded by several lobes of lower intensity. The amplitude pattern is described theoretically using the infinite energy solution [Durnin et al., 1987] as:

$$A(r, z, t) = J_0(k_0 \sin\theta r) e^{ik_0 \cos\theta z} \tag{1.7}$$

where $k_0$ is the wavevector and $\theta$ is the conical angle, called the Bessel angle. Thus, the Fourier transform of a Bessel beam is a ring with a radius of $k_0 \sin\theta$, and the annulus width is inversely proportional to the length of the Bessel beam. This solution, similar to plane waves, carries an infinite amount of energy, while experimentally, we can generate only an apodized solution.

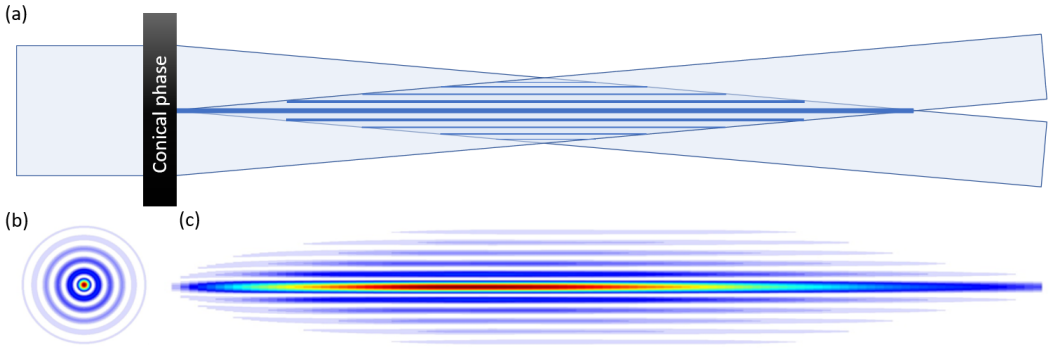


Figure 1.11: (a) A Bessel beam is a cylindrically-symmetric field of interference and can be for instance generated using an axicon lens. (b) Example of a transverse cross-section of the intensity distribution of a Bessel-Gauss beam. (c) Longitudinal cross-section of the intensity distribution. The intensity scales from blue (low) to red (high).

**Zeroth-order Bessel beams:** Generally, laser beams have a Gaussian profile; therefore, in practice, the Bessel beams obtained experimentally are shaped from a Gaussian beam and are often referred to as Bessel-Gaussian beams. Therefore, the field at the beginning of the interference field (i.e. conical phase and Gaussian amplitude distribution in the starting plane) is of the following form:

$$A(r, z = 0) = A_0 \, e^{ik_0 r^2/2q} e^{-ik_0 r \sin\gamma} \tag{1.8}$$

where $\gamma$ is the conical angle, and $q$ is the complex radius of the Gaussian waist.

The intensity evolution of the Bessel core as a function of the propagation distance z follows [Jarutis et al., 2000]:

$$I(z) = 4P_0 k_0 z \sin^2\theta e^{-2(z\sin\theta/\omega_0)^2}/\omega_0^2 \tag{1.9}$$

where $P_0$ is the Gaussian beam power and $\omega_0$ is its beam waist.

### 1.3.2/ Difference between Bessel and Gaussian beams

Here, we will see that the length and the diameter of the central core of the Bessel beam can be independently controlled, which is in contrast with Gaussian beams.

Considering a laser source emits a collimated Gaussian at wavelength $\lambda$ with beam waist $\omega$, as shown in figure 1.12. In the spherical lens case, the beam focuses along the propagation axes $z$ with a beam waist $\omega(z)$ represented as [Self, 1983]:

$$\omega(z) = \omega_0 \left[1 + (z/z_R)^2\right]^{1/2} \tag{1.10}$$

where $\omega_0$ is the beam waist at the focal point and $z_R$ is the Rayleigh length which is the distance from $\omega_0$ to the double of its area cross section (i.e. $\omega(z_R) = \sqrt{2}\omega_0$) from Eq. 1.10. The Rayleigh length is described as [Self, 1983]:

$$z_R = \frac{\pi\omega_0^2}{\lambda}$$

In that case, the highly intense region (depth of focus) to induce nonlinear interactions is double that of the Rayleigh length.

$$depth\ of\ focus = 2\ z_R$$

And the beam diameter **D** at the focal point (i.e. $D = 2\ \omega_0$) is given by:

$$D \simeq \frac{4\lambda}{\pi\ \Theta_{focus}}$$

where the focusing angle $\Theta_{focus} = \frac{\omega}{f}$ while $f$ is the focal length.

Importantly, Gaussian beams have only one free parameter. In contrast, Bessel beams have two. In a Bessel beam, Bessel depth of focus $z_{max}$ is defined as:

$$depth\ of\ focus\ [z_{max}] \approx \omega / \tan(\theta)$$

contrary to the Gaussian beam, the Bessel core diameter is given as:

$$FWHM = 2.27/(k \sin\theta)$$

which means that the Bessel core diameter does not depend on the beam diameter $\omega$ [Tiwari et al., 2012].

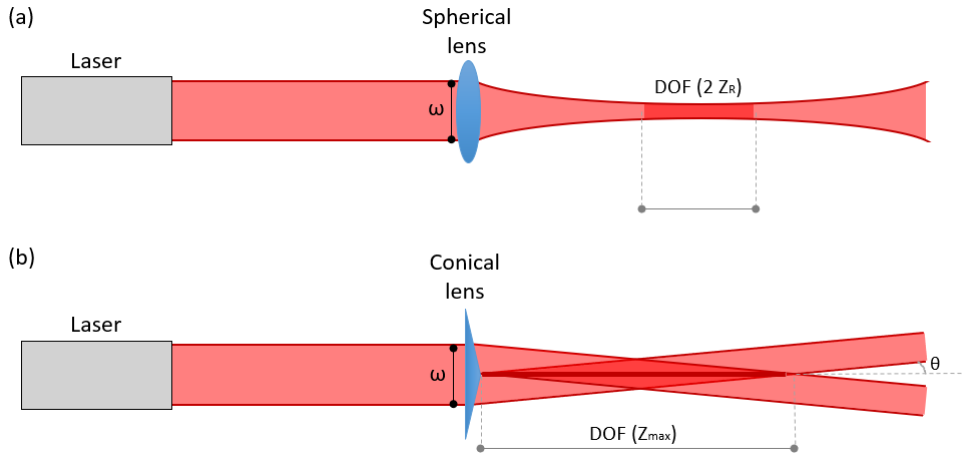


Figure 1.12: A comparison between a Gaussian laser beam affected by: (a) spherical lens and (b) conical lens. The depth of focus is noted as DOF.

**High-order Bessel beams:** These Bessel beams are vortex beams that possess an angular momentum [Lapointe, 1992]. Indeed, we can obtain a higher-order Bessel by adding a vortex phase $e^{im\theta}$ to the previous equation 1.8.

The high-order Bessel beams are characterized by an integer $m$ and the infinite-energy solution is $J_m e^{im\phi}$. In the initial plane of a higher-order Bessel-Gauss, the amplitude reads:

$$A(r, \theta, z = 0) = A_0 \, e^{ik_0 r^2/2q} e^{-ik_0 r \sin\gamma} e^{im\theta} \tag{1.11}$$

Figure 1.13 presents a transverse profile at the peak intensity of the Bessel beam with different orders. As we see in the figure, the vortex amplitude controls the diameter of the Bessel intense core in the higher-order case (i.e. $m \neq 0$). However, the negative orders (i.e. $m < 0$ ) produce exactly the same intensity profiles (only the phase rotation is in the reverse direction).

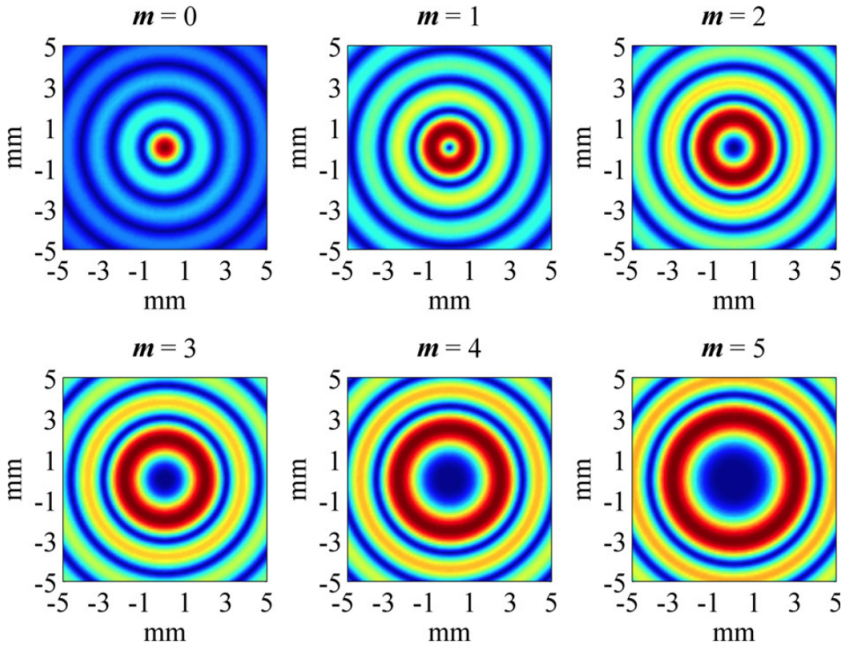


Figure 1.13: Transverse profile of an ideal high-order Bessel beams. Figure from [Mitri, 2008]

### 1.3.3/ BESSEL BEAM SHAPING METHODS

As explained before, the Gaussian beam is shaped into a Bessel beam by applying a conical phase in its propagation path. Moreover, it is possible to shape the beam in direct space and Fourier space. Thus, there are several techniques have been developed in order to generate these beams, such as spatial light modulators (SLM) [Chattrapiban et al., 2003], diffractive optical elements [Amako et al., 2003], and transmissive [Grunwald et al., 2004] or axicons [Boucher et al., 2018]. In this section, we briefly review the different configurations and techniques for generating Bessel beams.

#### 1.3.3.1/ CONFIGURATION OF BESSEL GENERATION

The key to generate a Bessel beam is producing a conical superposition of plane waves. Experimentally, we can achieve this conical interference in two different ways.

**Direct-space shaping:** The first method aims to apply a conical phase $\Phi(r)$ to the plane wave or the Gaussian beam, as shown in figure 1.14. The axicons can generate Bessel beams with an angle reasonably higher than the spatial light modulators (SLMs) and diffractive elements typically some degrees compared to some mrad on the other side. However, SLMs have a huge advantage for research purposes in that it is programmable, which helps get more control over the generated Bessel beam.

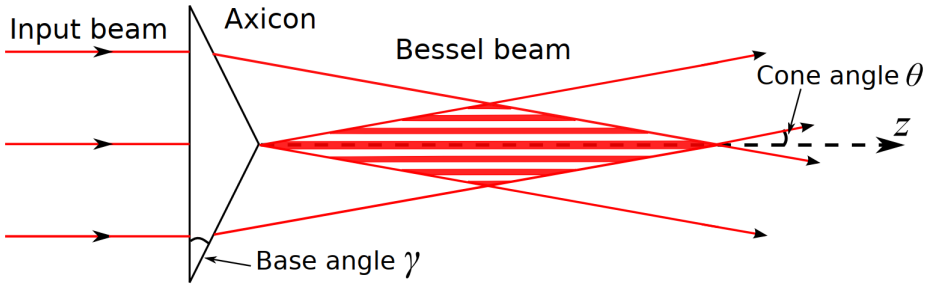


Figure 1.14: Bessel beam generation using an axicon. Figure from [Ouadghiri Idrissi, 2018]

**Fourier-space shaping:** This approach allows generating a Bessel on a two-step procedure: first, we can obtain a ring pattern equivalent to a Bessel beam distribution in the far field using an annular aperture, for instance, after that this ring is focused using a spherical lens placed at a distance equal to its focal length. As shown in figure 1.15, a conical interference occurs which means a generation of Bessel beam [Durnin et al., 1987].

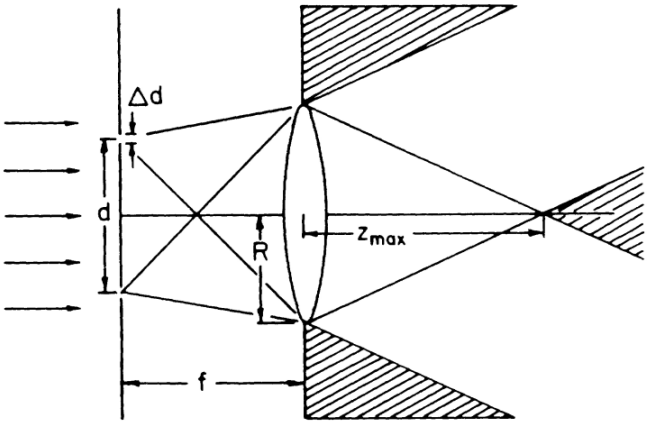


Figure 1.15: Bessel beam generation using an annular aperture. Figure from [Durnin et al., 1987]

#### 1.3.3.2/ BESSEL BEAM GENERATION USING SLMS

It is possible to replace many optical elements with a flexible and computer-controllable optical solution. The spatial light modulator (SLM) is a device whose function is to modulate the wavefront. The modulation is ensured by a matrix of liquid crystals, addressed optically or electronically: the orientation of the liquid crystals locally modifies the refractive index (along 1 polarization direction) and, hence, the optical delay that an optical field undergoes in transmission. This modulation is independent pixel per pixel, unlike in a deformable mirror. The SLM then represents a pure phase object acting as a programmable hologram. Therefore, an SLM allows imposing on an incident beam an arbitrary phase profile in two dimensions, dynamic and sampled by the dimension of the pixels of the device. Since 1993, SLMs have been widely used as Bessel beam generators in scientific research [Davis et al., 1993, Froehly et al., 2014].

Hamamatsu photonics company provides LCOS-SLMs (liquid crystals on silicon SLM). Its active surface is fabricated as a matrix of pixels. Thanks to LCOS-SLM high resolution up to 1024×1280 and $2\pi$ sampling level of 256, we can generate Bessel beams experimentally in direct-space and Fourier-space configurations.

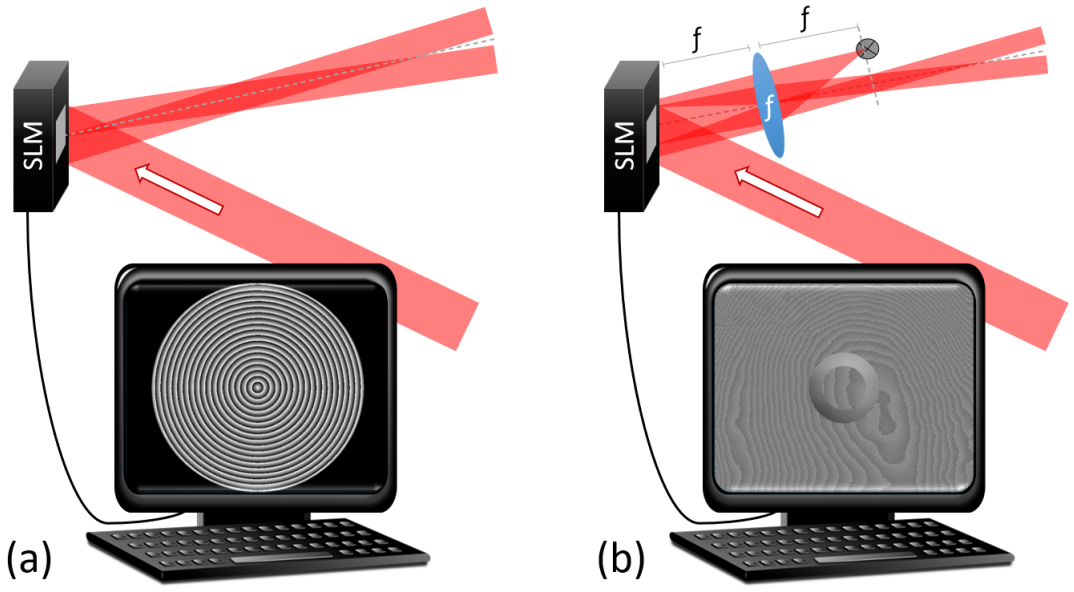


Figure 1.16: Bessel beam generation using SLMs: (a) In direct-space and (b) In Fourier-space.

**High order Bessel beam generation:** The scheme in figure 1.17 shows the last version of our experimental setup. In our work, an amplified Ti:Sapphire laser system at 800 nm wavelength and a pulse duration of around 100 fs is used. We use spatial light modulators to shape the emitted Gaussian beam into a Bessel beam due to their advantage in the research of programming the applied phase mask as needed. The spatial light modulator is used to create a first Bessel beam with a very low cone angle due to the limited resolution of the SLM; this first Bessel beam is demagnified using a telescopic arrangement that combines a lens and a microscope objective. Then, a high cone angle Bessel beam is generated with an angle of 26° for the material processing.

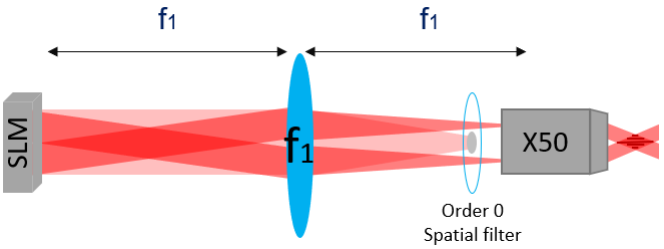


Figure 1.17: Single-shot setup scheme: From left to right, SLM to obtain Bessel beam, demagnification telescope 200:1 using a lens with focal lens $f_1$ = 970 mm and microscope objective ×50, and $0^{th}$ order spatial filter to clip the unmodulated part from the SLM.

## 1.4/ BESSEL BEAMS FOR LASER MICRO-MACHINING

Bessel beams are used in various applications such as electrical discharge guiding [Clerici et al., 2015], laser-generated plasma waveguides [Durfee et al., 1995], laser ablation, and materials processing [Amako et al., 2003].

### 1.4.1/ BESSEL BEAM FILAMENTATION

The filament caused by the nonlinear propagation of Bessel beams is different than the one induced by the Gaussian beam. As stated before, the interplay between Kerr's self-focusing and nonlinear losses forms the Gaussian filaments. Polesana et al have identified three different regimes for the nonlinear propagation of Bessel beams inside dielectrics [Polesana et al., 2008]. The first type corresponds to weakly nonlinear Bessel beams, which do not undergo any losses. The second type leads to a quasiperiodic deposition of energy on the material along the filament. The third type corresponds to continuous longitudinal laser energy deposition; which generates a homogeneous plasma channel.

The third family is the most interesting for micro-fabrication. It is indeed the regime where enough losses occur in the central lobe to stabilize the dynamics. A conical flow of energy, oriented from the lateral lobes to the central one, compensates for the energy loss. This regime corresponds to the monochromatic Nonlinear Unbalanced Bessel Beams (NLUBB). Indeed, a Bessel beam's interference is a superposition of two cylindrical Hankel waves with equal weights, one propagating inward and the other propagating outward [Porras et al., 2004]. In the NLUBB, energy loss within the central lobe reduces the weighting coefficient for the outward component. This reduces the contrast of the fringes and implies a net energy flow towards the centre.

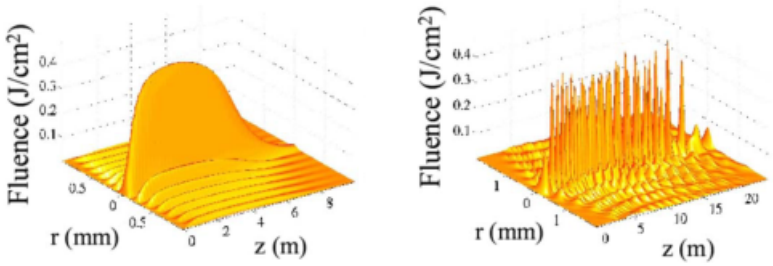


Figure 1.18: Numerical simulation of the filamentation caused by Bessel beam (left) and Gaussian beam (right). Figure from [Polesana et al., 2008]

The propagation-invariant NLUBB solution was proposed as an attractor to the filamentation regime [Porras et al., 2004]. This solution cannot be found for all input parameters, but the operating window, in terms of peak power, is wider when the cone angle is increased. Indeed, for higher peak powers, nonlinear losses are higher, reducing the impact of Kerr nonlinear dynamics. This has a significant impact on applications to laser materials processing: high powers are needed to generate high plasma densities.

### 1.4.2/ HIGH ASPECT RATIO DIELECTRIC MATERIALS PROCESSING

Interestingly, during the laser processing using Gaussian beams, Juodkazis S. et al. observed voids opening using a strong focusing, typically with numerical apertures close to or above one [Juodkazis et al., 2006]. Similarly, Bessel beams can open voids using the lower numerical apertures and relatively lower energies than those needed with Gaussian beams. In figure 1.19, we can see that a single laser pulse is enough to generate a high aspect ratio nanochannel inside a glass, which was first demonstrated in our group [Bhuyan et al., 2010].

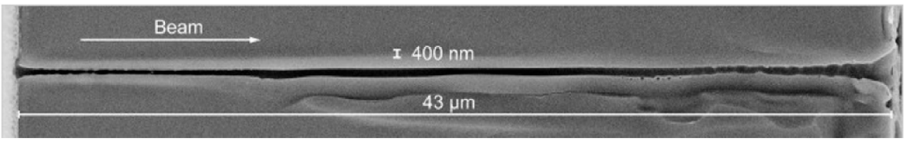


Figure 1.19: A nanochannel open by single-shot Bessel pulse. Figure from [Bhuyan et al., 2010].

Moreover, figure 1.20 shows that a single Bessel pulse can induce smooth voids with a high aspect ratio of hundreds of nanometers in diameter and tens of micrometres long within sapphire $Al_2O_3$ [Rapp et al., 2016].

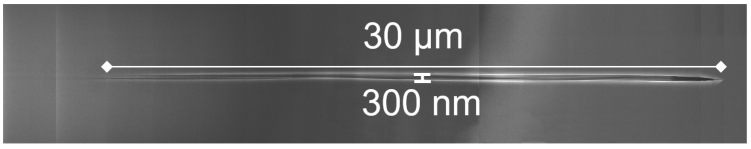


Figure 1.20: Nanovoid induced by a single pulse of Bessel beam inside sapphire. Figure from [Rapp et al., 2016].

Demonstrating a high-precision nanochannel obtained by single-shot Bessel pulse has pushed our group to go forward in research to target different industrial applications such as laser-glass cutting with flat or rounded edges [figure 1.21 (a)] and the drilling of through glass vias (TGVs) for 3D integrated circuits [figure 1.21 (b)]. Because the electronic signals transfer from one 2D silicon chip to another chip placed on top requires that through vias with diameters in the 5-30 $\mu$m range and length of typically 30 $\mu$m.

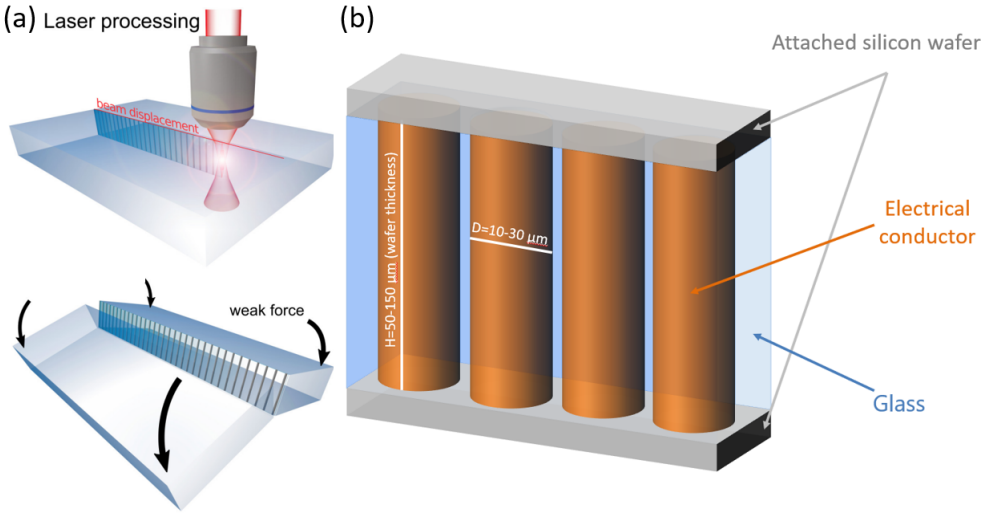


Figure 1.21: Applications of material processing: (a) Glass cutting (figure from [Meyer et al., 2017]) and (b) through glass vias.

#### 1.4.2.1/ Influence of the parameters of the Bessel beam

Experimentally, the choice of input conditions impacts the dynamics of Bessel filaments. For instance, the Bessel beam length allows controlling the damage length. In this context, R. Meyer et al. reported the longest modification up to 1 cm in thick glass using a Bessel beam propagating for a distance over 8 mm and mJ pulse energy [Meyer et al., 2019].

The pulse duration has a significant impact on the processing. The picosecond pulses enhance the damage in fused silica compared to femtosecond ones [Bhuyan et al., 2015]. However, Mitra et al. have reported a channel with an aspect ratio 1200:1 for 50 fs pulse duration in borosilicate [Mitra et al., 2015].

The laser wavelength has a weak influence on the process: similar results have been

reported with pulses at 800 nm and 1030 nm central wavelength.

However, in the latter case, even increasing the pulse energy does not allow for drilling vias with diameters exceeding 1 $\mu$m, as shown in Figure 1.13. Cylindrical tubes of light, shaped as higher-order Bessel beams, did not provide the opportunity to open cylindrical voids, in contrast with what the shape could make expect [Xie et al., 2015]. Therefore, more understanding is needed for the laser-plasma interaction.

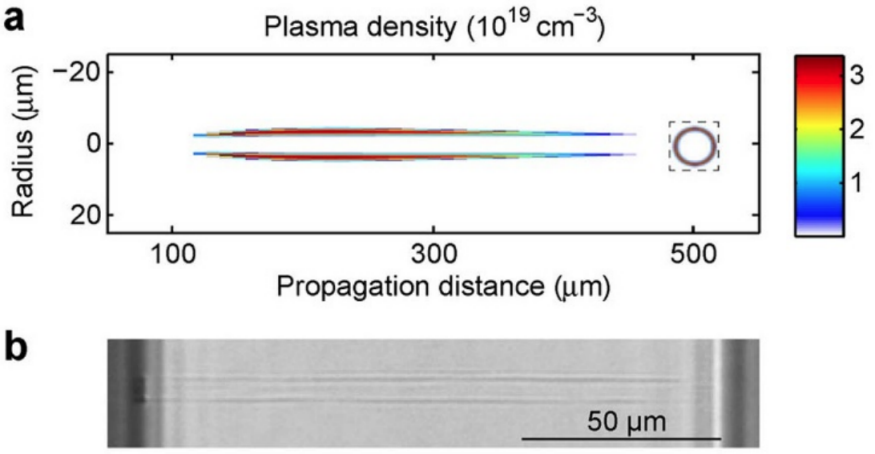


Figure 1.22: Generation of a tubular plasma. (a) The plasma density distribution. (b) A side view of a tubular damage in the glass.

### 1.4.2.2/ LASER-INDUCED PLASMA DYNAMICS

If we look at the time scale of laser-dielectrics interactions [Gattass and Mazur, 2008] (see figure 1.23), we can distinguish three main categories:

- The processes of creation of free charges, whose characteristic times are at ten picoseconds.
- Coupling processes of the hot free-electron plasma with the lattice establishes local thermodynamic equilibrium.
- Energy relaxation processes in the form of phase transitions and thermomechanical diffusion.

As we can see in figure 1.23, during the laser pulse propagation in the dielectric, the Bessel beam creates a plasma of free electrons and ions. After that, the hot electron gas transfers its energy to the relaxed lattice, which undergoes a rapid phase change (melting, evaporation, atomization) followed by a channel opening. Therefore, the main challenge is to characterize the energy and plasma densities created by the laser pulse itself.

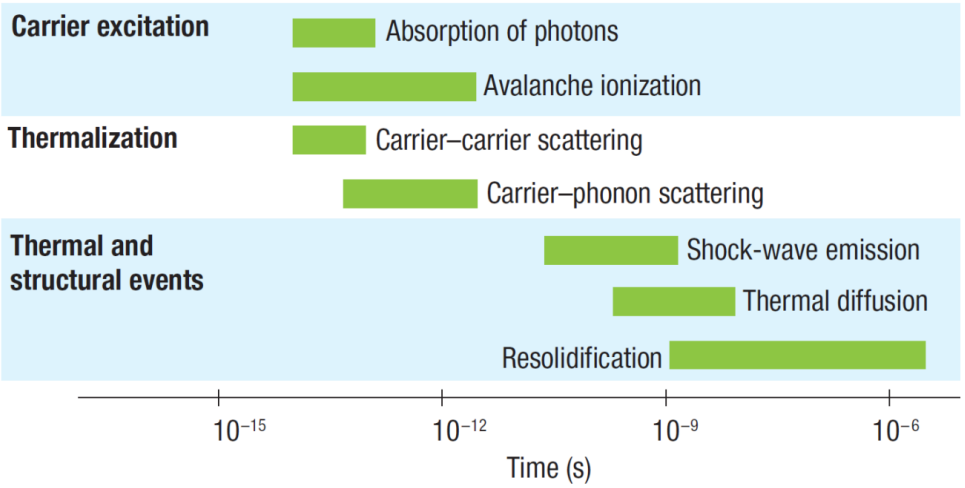


Figure 1.23: The physical phenomena timescale for the laser-dielectrics interaction. Figure from [Gattass and Mazur, 2008]

### 1.4.2.3/ VOID FORMATION IN DIELECTRICS

In the literature, as we can see in figure 1.24, there are two hypotheses made to explain the mechanism of void formation in the bulk of dielectrics. In the first mechanism, the intense pulse creates a plasma whose density largely exceeds the critical density (see section 3.2). In this case, as shown in figure 1.24(a), the void opening is produced by a microexplosion by the relaxation of the hot plasma and on a typical timescale of hundreds of picoseconds [Juodkazis et al., 2006]. On the contrary, recently, Bhuyan et al reported that, in fused silica, the void opening seems to be very slow ($\mu$s timescale), as shown in figure 1.24(b and c). This group explains the void formation by cavitation inside a liquid phase. In this case, the plasma density would not need to exceed the critical density to reach liquefaction [Bhuyan et al., 2017].

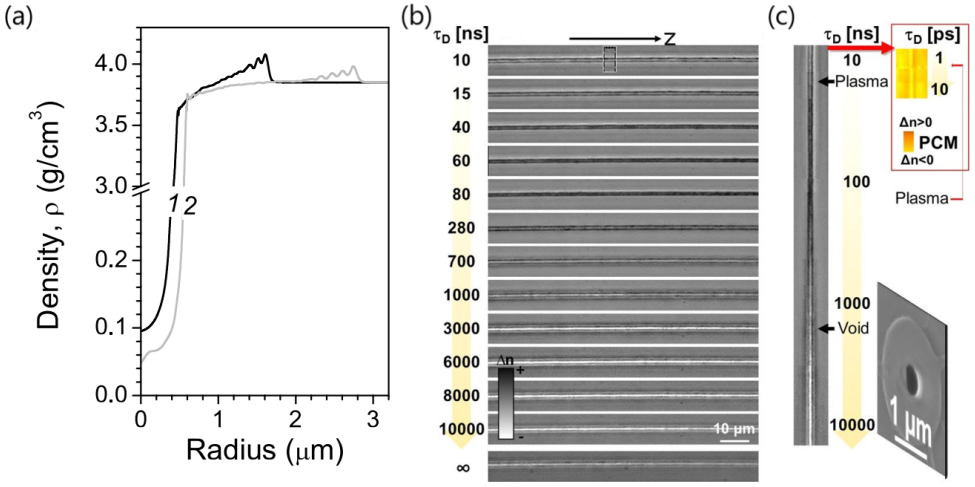


Figure 1.24: Opening void within dielectrics sequence. (a) Density profile of a volume with 130 nm radius at (1) 100 ps and (2) 200 ps. Figure from [Juodkazis et al., 2006]. (b-c) Time-resolved images of the index change. Figure from [Somayaji et al., 2020].

The challenging work concerns the investigation of the Spatio-temporal process of plasma creation under the conditions where a nanochannel can form. Indeed, we need the information on the actual plasma profile produced. In 2016, our group obtained experimental results for linear and non-linear propagation of a high-angle Bessel beam in fused silica by reconstructing the fluence profile obtained by scanning the beam(the technique is explained in detail in chapter 3). In figure 1.25 (b), we can see that the fluence profile is globally not affected by the formation of the plasma nor by the effects of self-focusing: the beam structure in the non-linear regime is almost identical to the linear case, and the side lobes remain in both cases well parallel to the central lobe. Comparing the experimental results with those brought by the resolution of the non-linear Schrödinger equation coupling the laser pulse to the plasma [Sudrie et al., 2002], an incompatibility of description appeared when conventional parameters of fused silica were used. The transverse fluence profile modelled is much broader than the one observed experimentally when the mean collision time between electrons ( parameter $\tau_c$) is 1 fs 1.25(c). The investigation of I. Ouadghiri thesis has shown that relatively accurate modelling of the dynamics of the ionization has only a little influence on the transverse profile. Only when an irrealistic collision time of 15 as is chosen, the numerical profile resembles to the experimental one (see figure 1.25(d)).

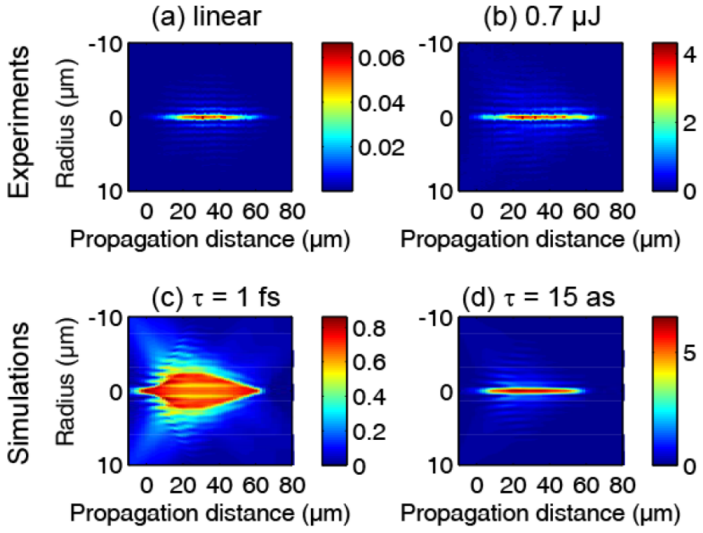


Figure 1.25: Fluence profiles of Bessel nonlinear propagation in J/cm$^2$ (a-b) linear and nonlinear experimental maps and (c-d) simulations with nonlinear Schrödinger model for $\tau_c$ = 1 fs and 15 as, respectively. Figure from [Xie et al., 2016]

We are interested in studying the generated plasma, because it is the first phenomenon of the laser-dielectrics interaction, as shown in figure 1.23. We need a reasonably fast enough technique to characterize it.

R. Meyer, the former PhD student in our group, has developed an interferometric pump-probe setup that visualises the index modification of several dielectrics on a timescale in the sub-picosecond regime (the technique is explained in detail in chapter 4) [Meyer, 2020]. He presented a complex time-resolving approach for building a hologram of the probe pulse that propagates collinearly with the pump Bessel pulse. However, retrieving the holographic signal was extremely difficult because the laser-generated plasma was apparently very small and highly opaque to the 400 nm probe pulse.

## 1.5/ CONTRIBUTION OF MY THESIS

Although many scientific works aim to understand the plasma generated by laser-matter interactions, the amount of energy deposited by ultra-fast Bessel pulse into the material is unclear. That is because the plasmas induced by Bessel beams are too small; thus, the previous imaging techniques failed.

Therefore, in this thesis work, we propose two strategies to quantify the generated plasma: the first is to combine a set of diagnostics and reproduce them using advanced simulations of laser-plasma interaction. The second is to develop a new technique, similar to ellipsometry, to measure the plasma using a probe shaped as a Bessel beam, which would not be blocked /diffracted on the nano-plasma.

# 2

# POLARIZATION SHAPED BESSEL BEAM

Bessel beams have many advantages, as described in the first chapter, particularly for laser materials processing. However, all these applications were performed using a fixed polarization state. It would be exciting to offer the possibility of controlling polarization along the propagation. Indeed, ionization and laser-plasma interaction are phenomena influenced by the polarization state. An example can be the generation of nanogratings in the multiple pulse irradiation regime inside fused silica: polarizing elements can be laser-written for several applications. Polarization-shaped Bessel beams could offer a new degree of freedom for such applications.

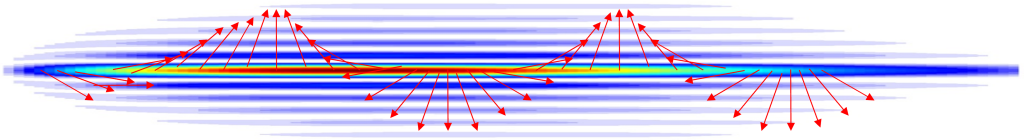

This chapter is dedicated to developing a new technique to shape the polarization state of the central core of the Bessel beam along its propagation. We first discuss the current laser writing of nanogratings inside fused silica and their limitations. Then, we present our approach for shaping the polarization, including the concept, experimental setup and calculation of the polarization state. After that, proof of principle is shown by comparing the results obtained by writing several structures with different parameters.

## 2.1/ INTRODUCTION

As we saw in section 1.1 about the use of ultrafast lasers for material processing, femtosecond lasers allowed 3D structures by inducing permanent modifications of the material structure inside the glass. The modification induced can be of different types: refractive index change, birefringence, ions migration, nanovoid arrays and periodic nanostructures. Laser-induced self-organized periodic nanostructures in glass are one of the most promising phenomena for creating on-demand optical functions. The periodic structure of the nanogratings is birefringent: the light speed is different between parallel and perpendicular directions to the nanograting array, as shown in figure 2.1. This has attracted enormous attention in the optics community because of the unique properties of the produced nanogratings, which we will explain in more detail in other sections. Besides, the self-assembly property of nanograting remarkably simplifies the fabrication process,

which requests femtosecond laser irradiation to cooperate with the movement of the microscale motion platform. These properties are highly favourable for future applications of nanograting in preparing integrated optical elements on a large scale.

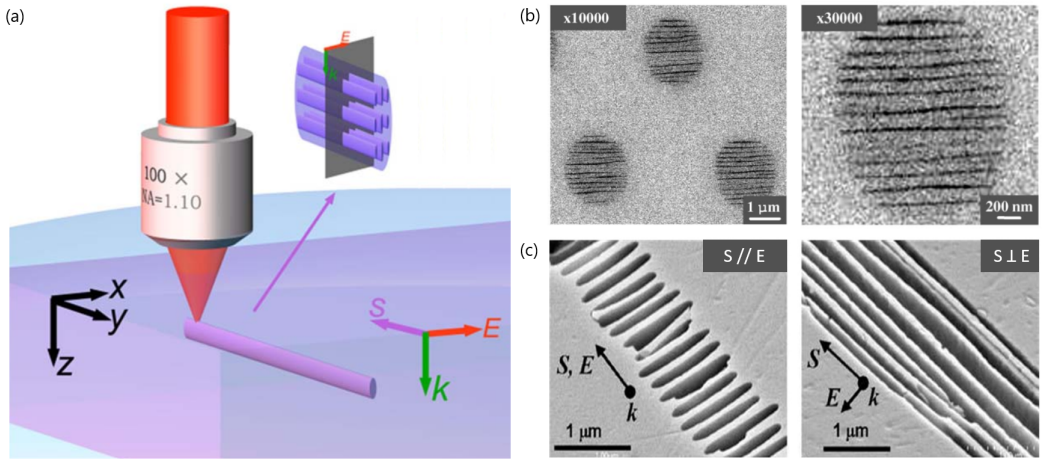


Figure 2.1: Principle of writing nanograting within glass: (a) Schematic illustration of femtosecond laser direct writing setup. Figure from [Liao et al., 2015] (b) backscattering electron images of nanograting structure. Figure from [Shimotsuma et al., 2003] (c) SEM images of nanograting grooves obtained by etching for 20min in 0.5% HF. Figure from [Hnatovsky et al., 2006]. While the laser propagation direction is k, the polarization direction is E, and the writing direction is perpendicular direction S.

In this section, we first briefly introduce the parameters and the relevant phenomena of laser-induced nanogratings. Then, considering the fast development, we show some potential applications based on forming nanogratings inside glass.

### 2.1.1/ LASER-INDUCED NANOGRATING

#### 2.1.1.1/ PARAMETERS AFFECTING NANOGRATING FORMATION

Many parameters related to the laser source affect the formation process of nanograting, such as wavelength [Beresna et al., 2013], pulse duration [Guo et al., 2004], pulse energy [Poumellec et al., 2011], repetition rate [Richter et al., 2012], polarization [Zhang et al., 2014a], pulse front tilt [Bulgakova et al., 2013] and scanning direction [Salter and Booth, 2012]. Moreover, the transparent material is one of the most critical keys to nanograting formation. The structure and characteristics of the material are changing, leading to different laser parameters needed for the processing. Several groups have investigated new materials to enhance the nanogratings [Komatsu and Honma, 2019], such as $\beta$-$BaB_2O_4$ [Miura et al., 2000], $Ba_2TiSi_2O_8$ [Zhu et al., 2007], or $LiNbO_3$ [Cao et al., 2019].

**Polarization direction:** In 1999, Kazansky et al. observed anisotropic scattering by femtosecond laser irradiation in germanium-doped silica glass for the first time [Kazansky et al., 1999]. After four years, as shown in figure 2.1 (b), Shimotsuma et al.

have confirmed the formation of nanograting on the focal plane vertical to the laser propagation direction [Shimotsuma et al., 2003]. Lancry et al. have analyzed induced tracks in fused silica using scanning electron microscopy (SEM) with nm resolution. They reported that nanostructures are porous nanoplanes with an average index lower than the one of the silica ($\Delta n \simeq 0.20$) [Lancry et al., 2013]. Further research showed that the modified regions induced by the laser are much more vulnerable to the strong acids and will be easily removed during the etching process, as in figure 2.1 (c) and leaving periodic grooves. As we mentioned before, the direction of nanograting arrays is always perpendicular to the laser polarization. Thus, the rotation of laser polarization rotates the nanograting axis. This leads to a variation of the intensity of white light transmitted through crossed polarizers [Zhang et al., 2014a], as can be seen in figure 2.2 (b).

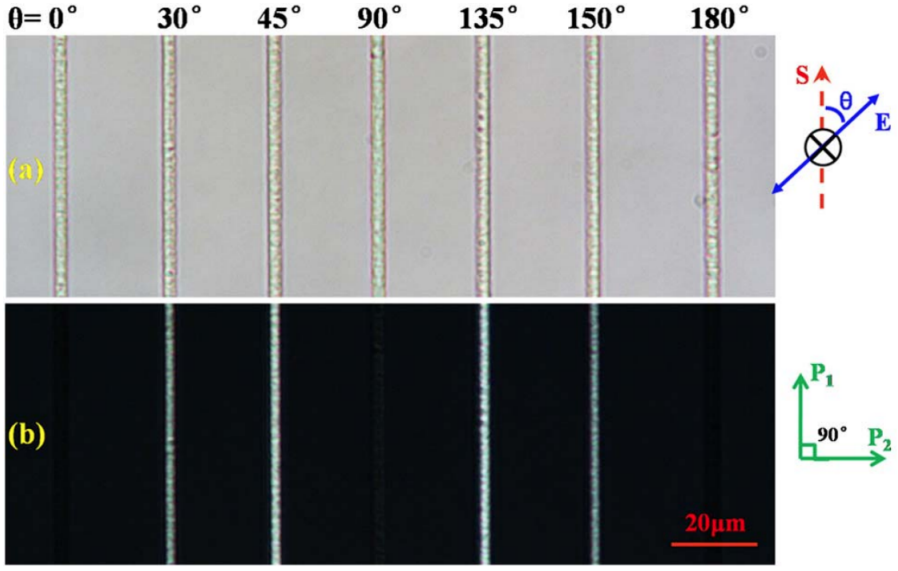


Figure 2.2: Optical microscope images of the horizontal lines fabricated by translating the sample perpendicular to the laser propagation direction: (a) in bright field and (b) between crossed polarizers. Figure from [Zhang et al., 2014a]

Zhang et al. have observed that the optical birefringence varies with the laser polarization by looking at the sample under an optical microscope in a bright field and between crossed polarizers, as shown in Figure 2.2. They obtained maximum intensity, hence the strongest birefringence during the crossed polarizers measurement in 45° and 135° cases.

**Energy deposition:** As discussed in the previous chapter, the interaction of the laser-transparent materials is a nonlinear process; the energy that transfers from the laser pulses to transparent materials is a nonlinear photoionization process whose intensity is closely related to the incident pulse energy. Thus, the pulse energy is essential in determining the laser modification regime [Poumellec et al., 2011]. The intensity thresholds generally measure the effect of pulse energy on structural modification in various processing conditions. As the incident pulse energy increases, more free electrons are generated, forming more defects, excitons and nanoplasma density that will, in turn, strongly interact with subsequent pulses. Excessive pulse energy will lead to ablation and melting,

destroying nanograting patterns. Therefore, nanograting formation needs proper processing windows.

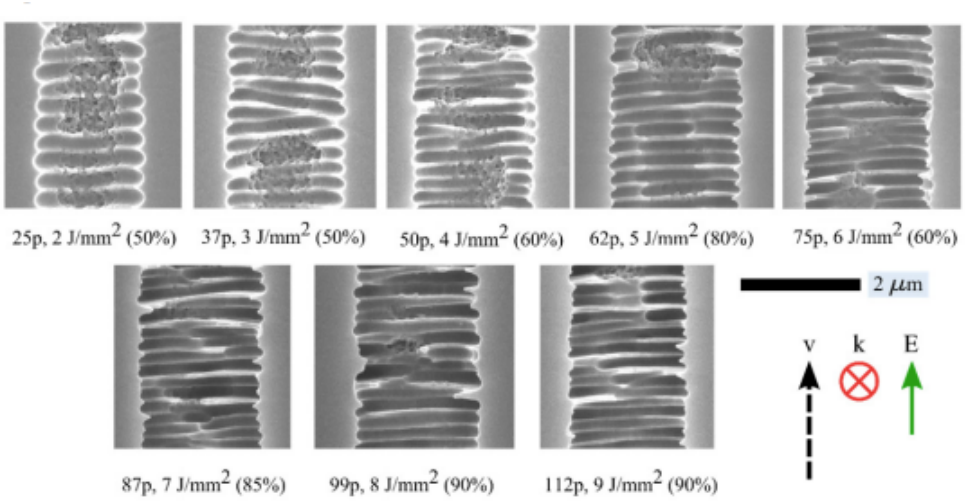


Figure 2.3: Induced self-organized nanogratings using different energy depositions by overlapping the pulses with a pulse energy of 180 nJ. The parameters of number of overlapping pulses, energy deposition and the volumetric percentage of the laser-affected zone below the surface are provided for each case. Figure from [Groothoff et al., 2015].

**Scanning direction:** When nanogratings are produced through the relative motion between laser beam and sample, structural differences have been observed with the change of scanning direction [Kazansky et al., 2007, Zhang et al., 2013]. Such direction-dependent structural difference has been understood in the framework of anisotropic laser energy distribution derived from the pulse front tilt (PFT) [Kazansky et al., 2007], which is usually caused by focal asymmetry, angular dispersion, such as the one induced by grating compressor misalignment. [Salter and Booth, 2012]. Since its discovery, various control methods for pulse front tilt have been proposed by different groups, including using the grating compressor, simultaneous spatial and temporal focusing (SSTF) or liquid crystal phase-only spatial light modulator (SLM) [Vitek et al., 2010]. Pulse front tilt is now considered as a vital parameter to regulate laser-matter interactions and generate scanning direction-dependent structural features [Poumellec et al., 2008].

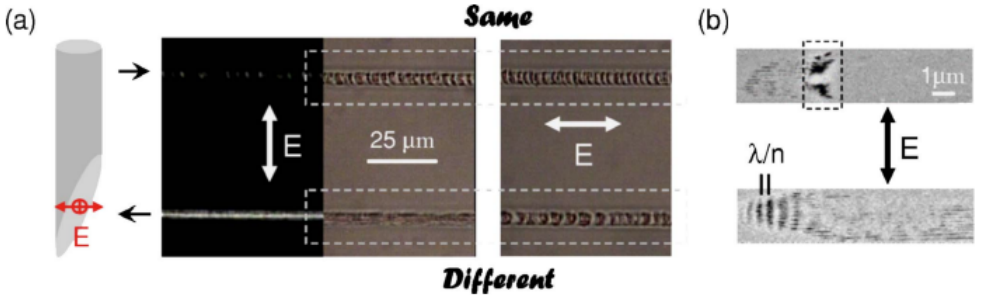


Figure 2.4: Lines written in one direction with orthogonal polarizations, considering the pulse front tilted along the writing direction. (a) Crossed-polarized and differential interference contrast images, (b) SEM images. Figure from [Kazansky et al., 2007].

#### 2.1.1.2/ APPLICATIONS OF FEMTOSECOND LASER INDUCED NANOGRATINGS

Recently, there have been many applications implemented based on laser-induced nanogratings. Kazansky's group reported the first nanograting-based diffractive element, a Fresnel zone plate produced by femtosecond direct writing in silica glass [Bricchi et al., 2002]. Following this work, more polarization-sensitive optical elements have been demonstrated, including waveplate [Richter et al., 2015], microreflector [Mills et al., 2002], light attenuator [Zhang et al., 2013], optical vortex converter [Beresna et al., 2011] and computer-generated geometric phase Fourier hologram [Drevinskas and Kazansky, 2017]. Moreover, optical birefringence demonstrates significant advantages in optical data storage. As the birefringence of nanogratings can be described by retardance and slow axis direction, it is feasible to independently control these parameters by regulating the intensity and the polarization of the incident beam, such that the nanograting-based data storage can provide two more memory dimensions than conventional structure based memory elements, namely a 5D data storage (3 coordinates, the slow axis direction, and retardance) [Nolte et al., 2013, Zhang et al., 2014b]. The higher sensitivity to HF or KOH etching can be used to process mechanical or fluidic components mode of glass [Tičkūnas et al., 2017].

### 2.1.2/ CONTROL OF BESSEL BEAM POLARIZATION

The idea of controlling the Bessel beam's polarization was reported for the first time in 2001. Tervo et al. have introduced an approach that permits Bessel fields to be radially and azimuthally polarized by combining generalized polarization gratings and diffractive axicons [Tervo and Turunen, 2001]. Some approaches have allowed the generation of Bessel beams with a spatial distribution of polarization, named vectorial Bessel beams. The typical cases have radial or azimuthal polarization states [Niv et al., 2004, Ornigotti and Aiello, 2013, Dudley et al., 2013]. Again, these polarization patterns remain constant along with the propagation distance.

In 2015, Moreno et al. presented a novel approach to modulate the polarization state of the Bessel beam over its propagation, from linear polarization to a circular one and back to a linear polarization [Moreno et al., 2015]. In addition to the phase mask that creates a Bessel beam, they added a phase shift between two orthogonal linear polarizations as a function of radius $\Phi(r)$, as shown in figure 2.5. In this case, the first part of the line focus, closer to the axicon, will be linearly polarized at -45°. In comparison, the final part of the line focus remains polarized at 45°, thus creating two line segments with orthogonal polarizations.

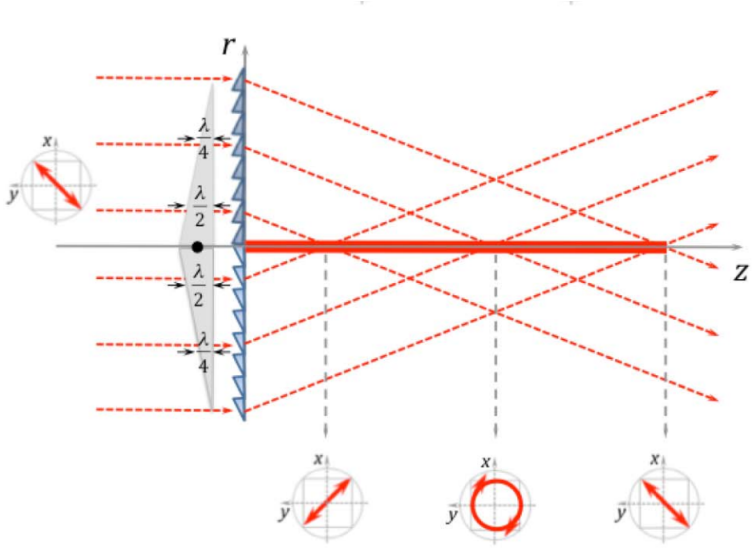


Figure 2.5: A scheme for producing a continuous variation of the state of polarization along the propagation distance. Figure from [Moreno et al., 2015].

However, this approach requires the ability to modulate the two components of the electric field. This cannot be achieved with a single liquid crystal SLM because it can modulate only one linear polarization component (parallel to the LC director). Hence, they built an experimental setup designed to modulate two orthogonal polarization components. In the optical architecture sketched in figure 2.6, a linearly polarized light beam is launched onto a transmissive parallel-aligned liquid crystal display (LCD), with the polarization direction at 45° with respect to the LC director axis. This way, the incoming beam is divided into two linear components with equal power, one parallel and another perpendicular to the LC director. While the first one is sensitive to the voltage applied to the display, the second remains unaffected. Then, inserting a quarter-waveplate, oriented at 45° with respect to the LC director, in the path of the not affected part twice, it becomes vertical linear polarization, and the phase pattern will modulate it.

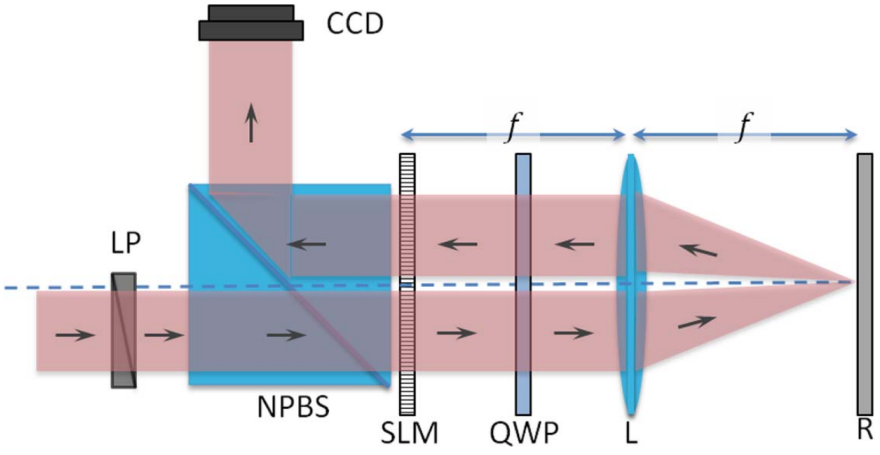


Figure 2.6: An optical system to modulate two orthogonal polarization components. Figure from [Moreno et al., 2015].

Controlling the polarization by dividing the beam and recombining it again has been developed and reported using different techniques. Li et al. have introduced the spatial spectrum approach to generate Bessel beams possessing variant axial intensities [Li et al., 2016]. Using the Sagnac interferometer, they superimpose two linearly polarized Bessel beams. Overall, it makes a rotating linear polarization with distance, as shown in figure 2.7.

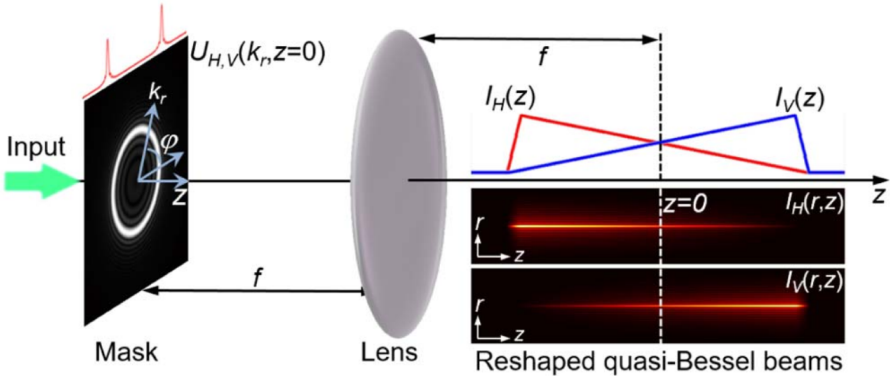


Figure 2.7: Schematic of reshaping the axial intensity distributions of quasi-Bessel beams. Figure from [Li et al., 2016]

Lü et al. proposed another recent technique of splitting and overlapping the beam [Lü et al., 2020], as shown in figure 2.8. Lü split the beam using SLM's phase mask. Then quarter wave plates were inserted between the two lenses of the 4f-system to change the polarization of the split two beams into circular polarization but in opposite directions, clockwise/anti-clockwise. In the end, the two beams are recombined by a phase-only Ronchi grating (RG) placed at the rear focal plane of L2. By controlling the power ratio between the beams using the pixel displacements on the mask, it becomes feasible to control the polarization orientation locally.

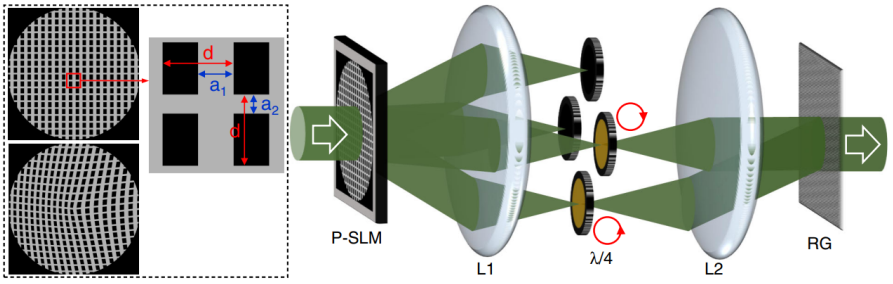


Figure 2.8: Schematic to control the polarization orientation locally. Figure from [Lü et al., 2020]

## 2.2/ OUR APPROACH: POLARIZATION-SHAPED BESSEL BEAM

### 2.2.1/ THE CONCEPT

In the previous chapter, we have described how Bessel beams can be generated by adding a conical phase to a Gaussian beam. From a geometrical optics point of view, we can remark that, in a Bessel beam, the photons within a crown at the input plane (beginning of the interference) focus at a specific distance on the optical axis, as shown in figure 2.9. In 2017, Müller et al. investigated segmented Bessel beams created by placing different ring apertures behind an axicon illuminated with a plane wave [Müller et al., 2017]. These different segments can be considered as independent, and we can modify them in amplitude, phase or polarization. Regarding amplitude, I. Ouadghiri-Idrissi, a former PhD student in our group, provided several phase masks to control the Bessel beam on-axis intensity [Ouadghiri Idrissi, 2018].

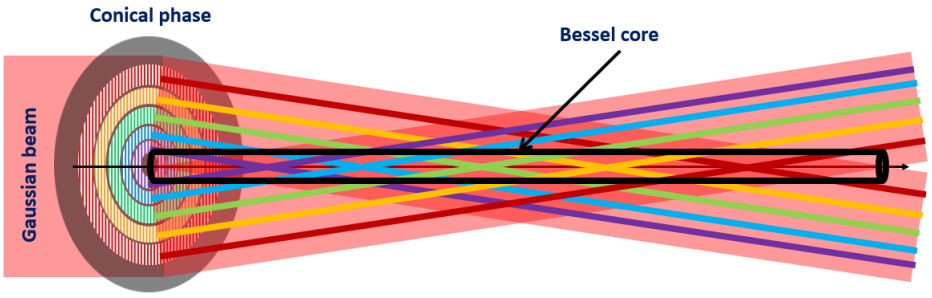


Figure 2.9: The different segments of the central core are related to independent crowns in the input plane.

To control the polarization along the propagation, we need segmented waveplates. These segmented waveplates can be generated using laser-induced nanogratings. The orientation of the nanogratings can be held using the input polarization of the Gaussian beam. Collaborators produced the waveplates at ICMMO Paris-Saclay University. The idea is to use special waveplates which rotate the polarization step by step versus radius. In figure 2.10, we show the segmented waveplate: the central polarization is $P_0$ and is modified by the step of $\Delta P$ at each ring. The ring width corresponds to the distance on which the conical phase is increased by $2\pi$ (see figure 2.6).

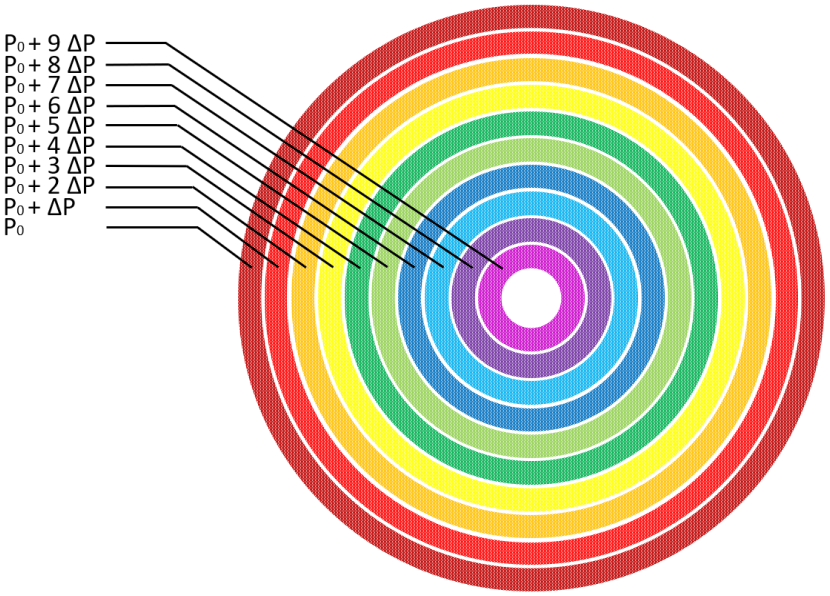


Figure 2.10: The special waveplates fabrication scheme, where $P_0$ is the zero rotation of the laser polarization annulus and $\Delta$P is the polarization rotation step.

The team at Paris-Saclay University has fabricated two waveplates: $WP_1$ rotates the polarization from 0° to 90° while $WP_2$ rotates the polarization from 0° to 180° on ten steps with $\Delta P$ of 10° and 20°, respectively. The number of steps is adjusted to match the number of independent segments inside the Bessel beam generated by our spatial light modulator. Figure 2.11 shows the concept of rotating the Bessel core polarization in a ramp from 90° to 0° using a waveplate fabricated from 5 annuli sharing the plate's centre. These annuli rotate the polarization by 90°, 60°, 40°, 20°, and 0°, and they are represented in colours: purple, blue, green, yellow, and red, respectively. The polarization axis of the part of the beam passing through the inner purple ring is rotated by 90°. This part focuses on the purple line's path at a specific distance, leading to a change in that zone's polarization of the Bessel beam to 90°. The next part of the beam's polarization rotates to 60° by the blue annulus. Until the end of the Bessel, the polarization of the Bessel core's end follows the outer red ring rotation. $WP_2$ is fabricated with the same concept and dimensions but a doubled rotation step between each annulus ($\Delta P_{WP_2} = 2\Delta P_{WP_1}$) in order to achieve a rotation of 180°.

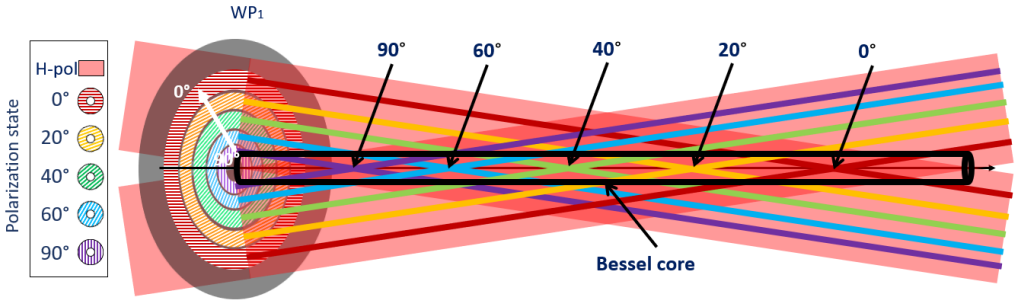


Figure 2.11: The concept of shaping the polarization of Bessel beam using $WP_1$. At the center of the waveplate, an area has no nanogratings for fabrication constraints.

### 2.2.2/ EXPERIMENTAL SETUP

Conventionally, our group forms Bessel beams by imaging the SLM with high magnification [Froehly et al., 2014]. As explained in the concept section, we need to insert the waveplates at the beginning of the interference plane. That means in the current setup, we would insert the waveplates either in front of the SLM or between the two microscope objectives. The first solution is not possible because we will also change the polarization of the input beam to the SLM while it requires linear horizontal plans. The second option is not doable for two reasons: first, the width of the demagnified beam will not be suitable for the waveplate size and second reason, we need to avoid damaging the waveplates. Therefore, the solution is to produce an image of the SLM plane using a 1:1 telescope.

As shown in figure 2.12 (a), we inserted a 1:1 telescope using a pair of lenses with focal distance $f_1 = 1\ m$. We use a homemade imaging system consisting of a magnification telescope 1:111 (microscope objective $\times$ 50 + lens with $f4 = 400\ mm$ ) and a CCD camera. We build the Bessel beam scan profiles, as shown in figure 2.12 (b), by moving the entire imaging system (the collecting microscope objective + lens + CCD) step by step and recording, for each propagation distance, the intensity distribution pattern on the camera, as the one on the left of figure 2.12(b), with extracting the intensity vector at Y = 0 $\mu$m.

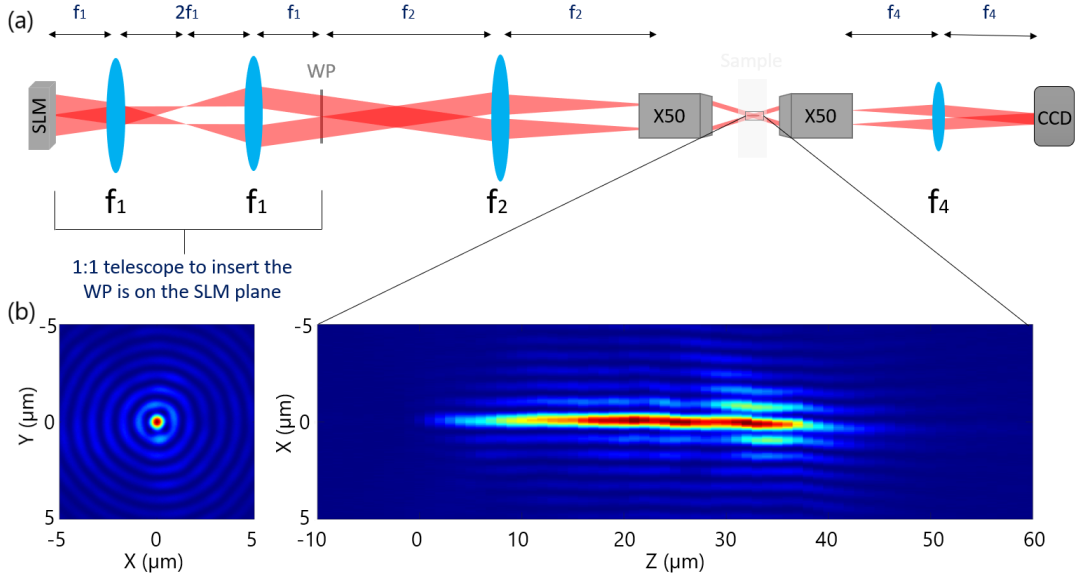


Figure 2.12: (a) Developed setup scheme: by adding 1:1 telescope to previous scheme 1.17 and (b) cross sections of the Bessel beam (left) XY-plane at z = 26 $\mu$m and (right) XZ-plane at y = 0 $\mu$m, where the beam propagates in the z-direction.

### 2.2.3/ CHARACTERIZATION OF THE POLARIZATION STATE

In order to characterize the polarization direction, we used the Stokes polarimetry method [Milione et al., 2014]. For that, we measure the intensities on the CCD camera $I_0(r,\phi)$, $I_{45}(r,\phi)$, $I_{90}(r,\phi)$, and $I_{135}(r,\phi)$ which are passing through an analyzer with transmission axis angle fixed at 0°, 45°, 90°, and 135°, respectively. In our case, the fields are fully polarized and we assume they have a linear polarization. Therefore we can compute the first two Stokes parameters $S_1$ and $S_2$, given by:

$$S_1(r,\phi) = I_0(r,\phi) - I_{90}(r,\phi),$$

$$S_2(r,\phi) = I_{45}(r,\phi) - I_{180}(r,\phi),$$

Then, the linear polarization state $\psi$ is given as:

$$\psi(r,\phi) = \frac{1}{2}\tan^{-1}\left(\frac{S_2(r,\phi)}{S_3(r,\phi)}\right). \tag{2.1}$$

We verified the concept section by determining the polarization state at the beginning of the interference plane (SLM plane) and along the propagation axis. To do so, we inserted an analyzer just in front of the camera to get $I_0$, $I_{45}$, $I_{90}$, and $I_{135}$ for the equation 2.1.

#### 2.2.3.1/ POLARIZATION STATE AT THE SLM PLANE

In the experiment, we find the SLM plane by moving the imaging system, which is placed on a motorized stage, back and forth until we visualize the SLM plane, where the beginning of the Bessel core with a movement precision of 1 $\mu$m. Figure 2.13 shows the polarization state at the beginning of the Bessel beam plane (i.e. at z = 0) using $WP_1$ on the left and $WP_2$ on the right. We can see a good match between the obtained results and the waveplate fabrication specifications shown in figure 2.10. We observe a progressive rotation of the polarization axis from the centre to the sides, excluding a defect region at the waveplates' centre due to fabrication limitations in the technique used by our collaborators. Figure 2.13 (left) concerns the polarization state at the SLM plane using $WP_1$. The polarization rotates from 90° to 0° versus radius. Also, the $WP_2$ rotates the SLM plane polarization as designed from 180° to 0°, as shown in figure 2.13 (right). These results predict a polarization rotation along the Bessel beam propagation.

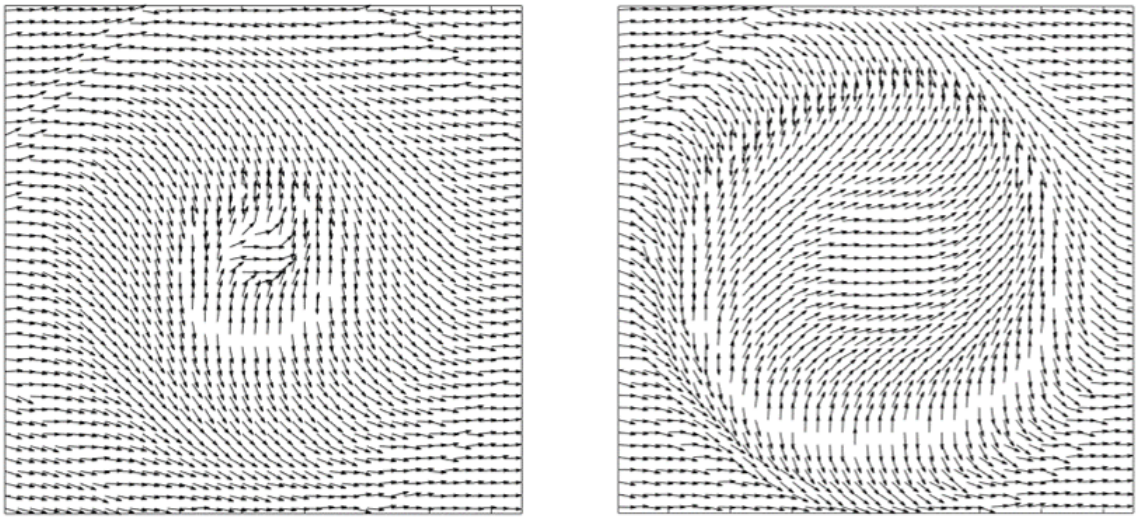

Figure 2.13: The polarization state at SLM plane using $WP_1$ on left and $WP_2$ on the right.

#### 2.2.3.2/ EVOLUTION OF THE POLARIZATION ALONG THE PROPAGATION

The beam intensity distribution has been recorded using the beam scan technique (see section 2.2.2), and a cross-section is shown in figure 2.14 (a). The intensity profile after inserting $WP_1$ is very similar to the one before inserting the waveplate shown in figure 2.12 (b). However, we observed a drop in the intensity around a propagation distance of 8 and 35 $\mu$m. These declines are the beam diffraction on the inner and outer edges of the effective area on the waveplate. The central defect region induces the inner periphery, while the outer edge is due to the larger beam waist at the SLM plane than the effective area diameter.
Figure 2.14 (b) presents an XZ cross-section colour map of the polarization state along the beam scan in subfigure (a). For the material processing, we apply a numerical threshold to focus on the polarization state of the high-intense part of the beam, which is the Bessel beam's core. As shown in figure 2.14 (c), we obtained an excellent agreement between expected and experimental polarization rotation from 90° to 0° along with the Bessel beam propagation, taking into consideration the defect and the effective diameters of the waveplate.

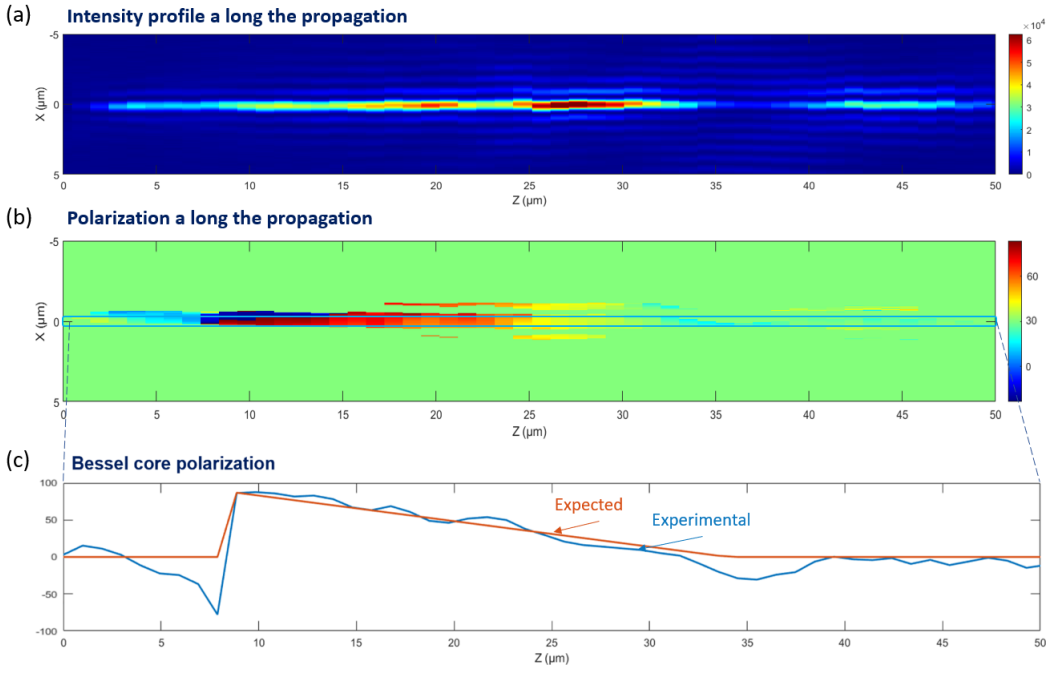


Figure 2.14: Polarization shaped Bessel beam using $WP_1$: (a) beam scan while ignoring the polarization state, (b) the polarization state along the propagation, and (c) comparison between the Bessel core polarization experimental and expected results.

By replacing $WP_1$ with $WP_2$, we obtained a polarization rotation from 180° to 0°, as shown in figure 2.15. Because of the two waveplates are identical in terms of size, we observed the same intensity drop at 35 $\mu$m of the propagation distance 2.15 (a). Figure 2.15 (b) shows the variation of the Bessel's polarization direction from 180° to 0° in a color map. Also, we have obtained a reasonable agreement between expected and experimental polarization rotation, as shown in figure 2.15 (c).

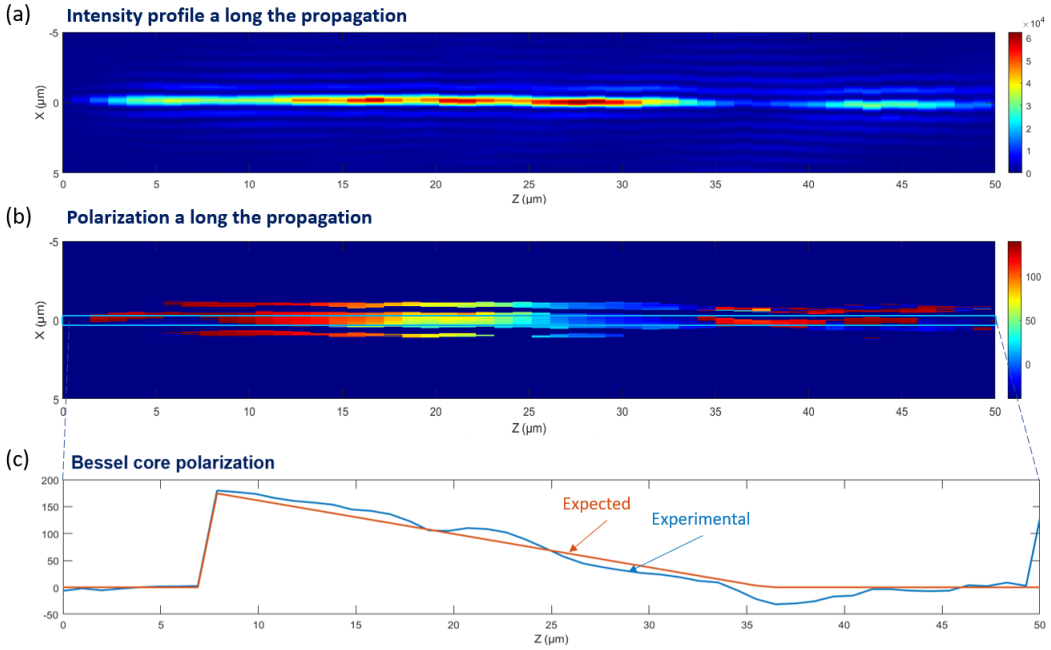


Figure 2.15: Polarization shaped Bessel beam using $WP_2$: (a) beam scan while ignoring the polarization state, (b) the polarization state along the propagation, and (c) comparison between the Bessel core polarization experimental and expected results.

These figures have been obtained from five beam scans for each waveplate. Four beam scans are acquired with rotating the analyzer transmission axis to 0°, 45°, 90°, and 135° for the polarization state calculations. The analyzer is removed to get the last beam scan to measure the full-beam intensity profile, as shown in figures 2.14 (a) and 2.15 (a).

## 2.3/ LASER INSCRIPTION OF SPATIALLY-VARYING NANOGRATINGS IN FUSED SILICA

This section shows the ability to induce nanogratings by a direct-writing technique using a femtosecond laser shaped in a Bessel beam with longitudinally-varying polarization. We confirm by this part that polarization-shaped Bessel beams can be usefully exploited to control the orientation of nanogratings created by the multiple shot irradiations in fused silica. In order to evaluate the advantage of using polarization-shaped Bessel, we wrote the nanogratings with different scanning strategies, energies, writing directions and polarization states. Moreover, we used two polarization states for the comparison and quantify the effect of using polarization-shaped Bessel beams: a fixed linear polarization that is oriented at 45° direction and linear polarization rotates along the propagation from 90° to 0° using $WP_1$ (Bessel $WP_1$).

### 2.3.1/ SAMPLE PROCESSING

The idea is to use the polarization-shaped Bessel beam to write nanograting in fused silica. To quantify the achievements obtained, we need to write several nanograting by

changing as much as possible the effecting parameters explained in the introduction. Thus, we wrote small squares 50 $\mu$m $\times$ 50 $\mu$m (with different writing directions), large squares 200 $\mu$m $\times$ 200 $\mu$m, and long lines 3mm. These structures were repeated on a scale of energies from 200 nJ to 1.8 $\mu$J.

We used the developed processing system which is shown in figure 2.12 (a) to write the nanograting structures within a 400 $\mu$m thick fused silica. The structures were inscribed by a significant overlap of pulses at the writing speed of 10 $\mu$m/s considering the 1 kHz repetition rate of the laser source, at a depth of $\approx$ 100 $\mu$m from the sample back surface.

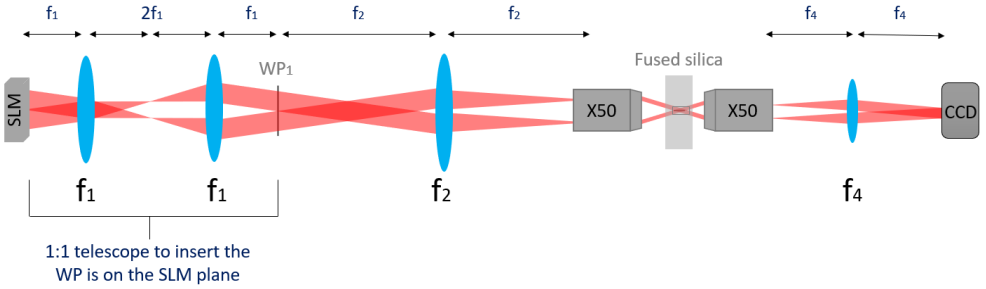


Figure 2.16: The same setup shown in figure 2.12 to inscribe spatially-varying nanogratings by using $WP_1$ within fused silica with thickness of 400 $\mu$m at depth of $\approx$ 100 $\mu$m.

### 2.3.2/ Sample characterization at Paris-Saclay University

The characterization of the sample, which is presented in this section, has been performed by our collaborators at Paris-Saclay University. Our collaborators characterized the nanogratings created by 45° linearly polarized Bessel beam and Bessel $WP_1$ optically by measuring the optical rotation, the total linear birefringence, and the circular birefringence. Moreover, they used SEM to extract a side-cut of the nanograting.

- **Optical rotation**, also known as polarization rotation, is the rotation of the polarization orientation about the optical axis of the linearly polarized light as it travels through certain materials.
- **Total linear birefringence** is the difference in refractive index between linearly polarized light with orthogonal planes of polarization.
- **Circular birefringence** is the difference in refractive index between left and right circularly polarized light.

#### 2.3.2.1/ Optical characterization of the nanogratings

The team at Paris-Saclay University used a Senarmont microscope to measure the optical rotation, and Mueller spectroscope for the total linear birefringence and circular birefringence measurements [Tian, 2020]. As shown in figure 2.17, the energy threshold of creating nanograting to induce optical rotation is 0.5 $\mu$J. As one can expect, at that energy, the rotation of the linear polarization axis is almost negligible in the case of the 45°

linearly polarized Bessel beam around 2°. On the contrary, in the case of Bessel $WP_1$, the rotation is much higher, about 10°. However, the rotation increases in both cases by increasing the processing energy to 28° using Bessel $WP_1$ and surprisingly to 13° using the 45° linearly polarized Bessel beam at 1.8 $\mu$J.

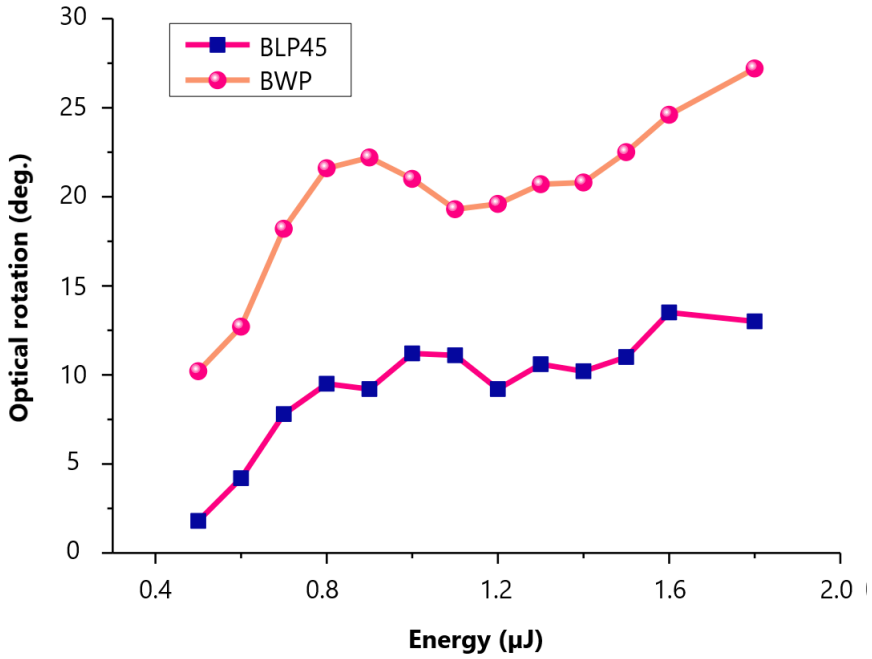


Figure 2.17: Comparison of the optical rotation of nanogratings obtained by Bessel beam linearly polarized and oriented at 45° (BLP45) and Bessel beam polarization-shaped by $WP_1$ (BWP). Figure from Paris-Saclay University's report (Jiafeng Lu and Matthieu Lancry, ICCMO).

Figure 2.18 shows the measurements of the circular birefringence (CB) and the total linear birefringence (TLB) which are obtained at Paris-Saclay University. As we can see:

- The total linear birefringence exhibits an increasing-decline trend according to energy increase.
- The 45° linearly polarized Bessel beam has larger total linear birefringence than Bessel $WP_1$ by a factor of 4 to 5 times.
- Circular birefringence also shows an increasing decline trend at energy increase.
- Bessel $WP_1$ has larger circular birefringence than the 45° linearly polarized Bessel beam 2-3 times.

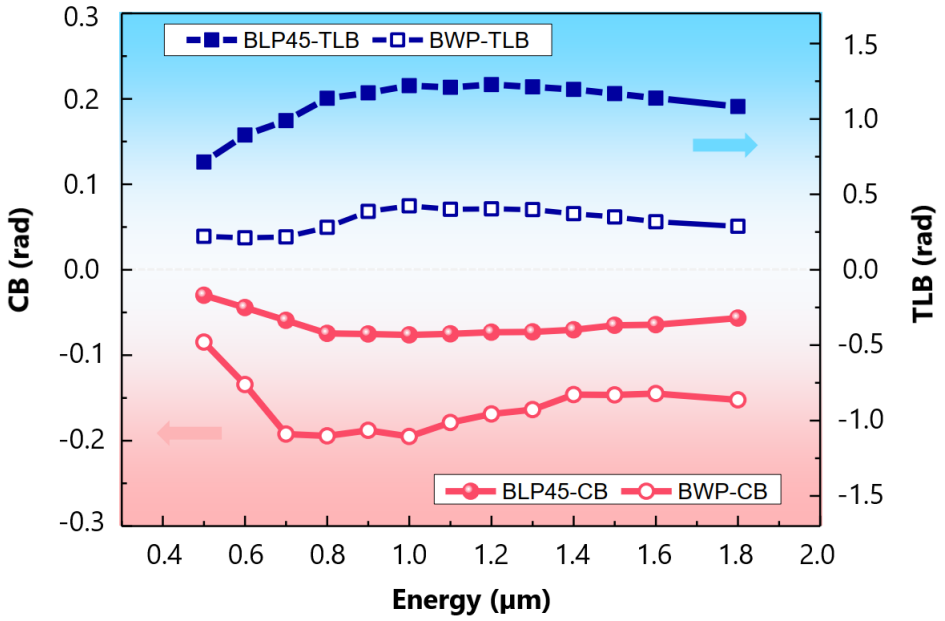


Figure 2.18: Comparison between circular birefringence (CB) in red and total linear birefringence (TLB) in blue of nanogratings obtained by Bessel beam linearly polarized and oriented at 45° (BLP45) and Bessel beam polarization-shaped by $WP_1$ (Bessel $WP_1$). Figure from Paris-Saclay University's report (Jiafeng Lu and Matthieu Lancry, ICCMO).

These results show an enhancement of circular birefringence by using a polarized varying beam rather than using a 45° linearly polarized beam. On the other hand, Bessel $WP_1$ owns a much lower total linear birefringence by a factor of five. This is very attractive for applications since it is important to be able and generate optical rotation without inducing linear birefringence.

#### 2.3.2.2/ STRUCTURE CHARACTERIZATION OF THE NANOGRATINGS

SEM images confirmed the creation of nanogratings that rotate with the polarization rotation. As we can see in figure 2.19, the 45° linearly polarized Bessel beam propagates from left to right with pulse energy of 1 $\mu$J and creates nanogratings look like a combination between nano-lines and nano-pores.

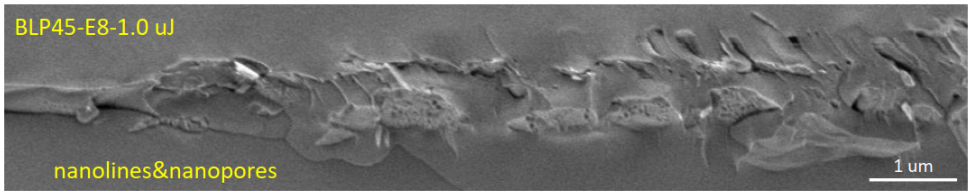


Figure 2.19: The nanogratings created by the 45° linearly polarized Bessel beam. Figure from Paris-Saclay University's report (Jiafeng Lu and Matthieu Lancry, ICCMO).

On the other hand, the nanogratings obtained using Bessel $WP_1$, as shown in figure 2.20, are rotating and follow the polarization rotation in the figure 2.14. Figure 2.20 shows the cross-section of the nanogratings structure that has been produced using 1 $\mu$J of polarization-shaped Bessel beam. The subfigures b-d focus on three separate regions corresponding to writing at 90° polarization, at the mid-range of the polarization change, and 0° polarization regions, respectively. In region (b), where the beginning of the polarization-shaped Bessel beam is, we obtained a nanopores region because of the 90° polarization. The region (c) shows a combination between nano-lines and nanopores and looks as the one wrote by the 45° linearly polarized Bessel beam. After that, until the end, region (d) of nanolayers indicates writing with 0° polarization.

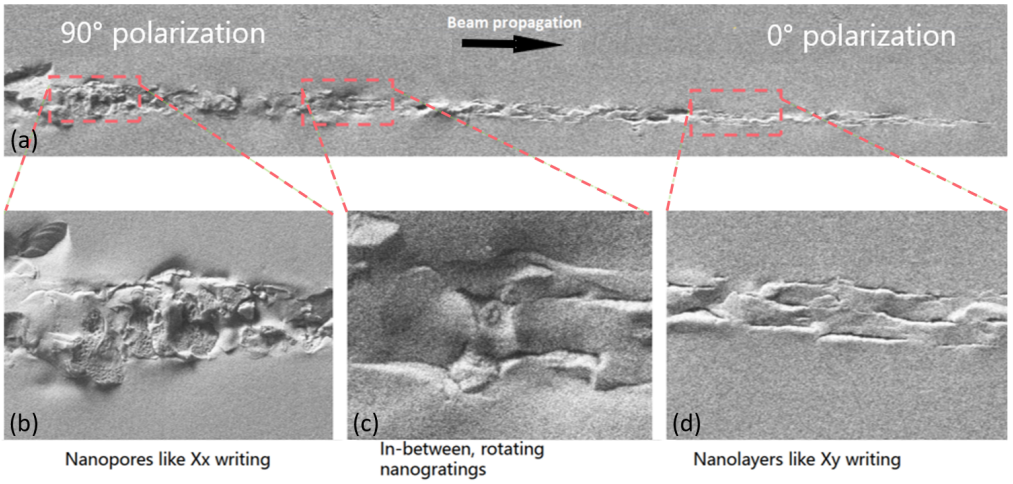


Figure 2.20: The nanogratings obtained by Bessel $WP_1$. b, c, and d are referring to the region of 90° polarization, at the mid-range of the polarization ramp, and 0° polarization, respectively. SEM figures from Paris-Saclay University's report (Jiafeng Lu and Matthieu Lancry, ICCMO).

## 2.4/ CONCLUSION

We demonstrated the polarization shaping of an optical pulse along its propagation. We successfully generated femtosecond Bessel beams with a length exceeding 60 $\mu$m for a submicron focal spot diameter, where the axis of the linear polarization continuously rotates from zero up to 180 degrees.

We use the laser-induced nanogratings technique to create a polarization-shaping element, which controls the polarization distribution of a diffraction-free Bessel beam. As seen in the optical characterization results in figure 2.18, the circular birefringence in the case of Bessel $WP_1$ is almost double that of the 45° linearly polarized Bessel beam case, while the total linear birefringence is reduced five times between Bessel $WP_1$ and 45° linearly polarized Bessel beam. Such a polarized-shaped beam can be effectively used to induce nanogratings that rotate along the propagation axis. We believe that this approach will be extremely useful to control the writing of arbitrary optical components.

# 3

# RESONANCE ABSORPTION WITH ULTRAFAST LASER PULSE INTERACTION WITHIN THE BULK OF DIELECTRICS

Since 2010, our group reported the formation of high-aspect nano-channels using ultrafast Bessel beams within the glass as shown in figure 1.19. Our group then studied the formation process to gather the knowledge of controlling the dimensions of the channel for several applications. As we saw in the first chapter, when laser pulses are focused within focal spots of a few $\mu$m, the intensities are commonly in the range of $10^{14}$ W/cm$^2$. At these intensities, the laser pulses ionize the sample and turn it into plasma. The generated plasma density is the critical aspect of laser material processing because the final material modification depends on the total deposited energy density which scales with the plasma density.

As mentioned in chapter 1, a key aspect to understand the mechanism of nanochannel formation is to identify if the plasma created is below or above the critical density. The critical density corresponds to the density at which the material's permittivity is zero at the laser wavelength.

In the first section, we introduce our group's previous work to understand the energy deposition, and the plasma formation mechanism including the obstacles we faced. As well known, the direct measurement of the plasma density inside the bulk cannot be performed via optical techniques when the plasma reaches the critical density at sub-wavelength scales (this will be investigated in chapter 4). Therefore, in the first part, we show the typical experimental diagnostics we can perform to obtain an indirect estimation of the plasma peak density and width by observing the fluence distribution of the laser pulse after its interaction with the sample. To understand the experimental results, we need a numerical tool to simulate the interaction and compare the results with the experimental ones. Subsections 3.1.1 and 3.1.2 present the simulation results obtained using the non-linear Schrödinger equation and particle-in-cell methods, respectively.

The particle-in-cell simulation results were promising and more reliable than the non-linear Schrödinger equation one. As we will see, the diagnostics in PIC simulations were fitting the experimental results except that the fluence distribution in the near field showed few disagreements. One of my contributions here was to demonstrate that positioning in the imaging of the near field is crucial, which can solve the problem.

In section two, we will therefore first review how a plane wave interacts is a plasma gradient before presenting the particle in cell simulation results.

Section 3 introduces the thesis work approach to characterize indirectly the plasma density. We present the parameters used in the simulation of the particle-in-cell method, an overview on the experimental setup we use for the diagnostics, and the reason of the disagreement between the experimental and numerical results.

Then, we present the diagnostics we performed to describe the plasma density. We explain the experimental high-absorption using the PIC simulation. Moreover, we detected the emission of the second harmonic single which is predicted by PIC simulations. In the last experimental PhD thesis of the group by Remi Meyer, the second harmonic generation was observed but with a high distortion by the background noise [Meyer, 2020]. We developed the setup to obtain more reliable results so that it could be used as another diagnostic to be compared with PIC simulations.

## 3.1/ PLASMA FORMATION BY INTENSE ULTRAFAST BESSEL BEAMS

For observing the laser-plasma interactions experimentally, the group used the beam sectioning technique (see section 2.2.2) that allows a 3D reconstruction of the fluence distribution of the Bessel beam during its nonlinear propagation inside dielectrics [Xie et al., 2015]. At each step of the imaging system movement, we image the sample back surface and shot with a single laser pulse at energies above the threshold of the nano-channel formation. As shown in figure 3.1, we observed that the direct-space fluence distribution of the Bessel beam nonlinear propagation with a Bessel angle of $26°$ (figure 3.1(b)) seems exactly as the linear case (figure 3.1(a)) but with the absorption of the laser energy of typically 50% over the Bessel beam length [Xie et al., 2016] (figure 3.1(c)) by integrating the field on the CCD camera.

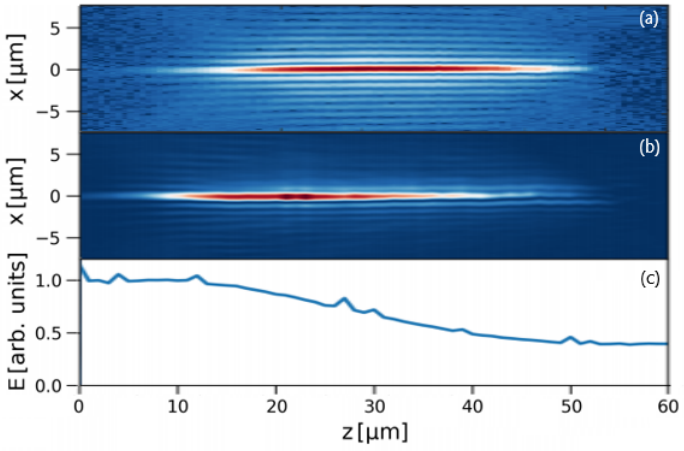


Figure 3.1: The experimental fluence distribution of Bessel beam with a cone angle of $26°$ within fused silica. (a) the linear regime, (b) non-linear regime, and (c) absorption along the propagation.

This value of $\approx$ 50% absorption is in excellent agreement with the results of Hoyo et al, in our group, where, with the same cone angle, the absorption was measured using a pair

of photodiodes [del Hoyo et al., 2020].

The fluence distribution map of figure 3.1 can be compared to numerical simulations. Our group started to study the nonlinear propagation of Bessel beams in dielectrics using the non-linear Schrödinger equation method.

### 3.1.1/ Comparison of the non-linear Schrödinger equation simulation with experimental results

Figure 3.2 shows the simulation results obtained by solving the non-linear Schrödinger equation combined to a plasma rate equation [Sudrie et al., 2002, Ouadghiri Idrissi, 2018]. The simulation results, as shown in figure 3.2, showed that the beam undergoes a strong defocusing: the lobes are shifted by more than 2 $\mu$m during the pulse duration. This is in contrast with the experimental results of Fig3.1. Therefore, we can say that the non-linear Schrödinger equation method fails to simulate the generated plasma and Bessel beam-plasma interaction.

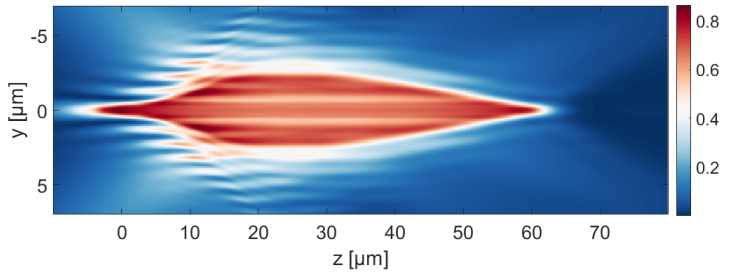


Figure 3.2: The nonlinear propagation intensity profile of Bessel beam with a cone angle of $26°$ obtained from the non-linear Schrödinger equation simulation. Figure from [Xie et al., 2016]

Thus, the group started to simulate the laser-plasma interaction using a particle-in-cell (PIC) code [Ardaneh et al., 2021]. The PIC simulation can provide several diagnostics to compare with experimentally, such as the fluence distribution of the direct and Fourier spaces of the Bessel beams during their nonlinear propagation, the overall absorption, and the second harmonic generation emission pattern.

### 3.1.2/ Comparison of the PIC simulation with experimental results

In our group, Ardaneh et al. estimated the typical plasma parameters, diameter and peak density, by comparing experimental diagnostics to first principles Particle-In-Cell (PIC) simulations using the 3D massively parallel code EPOCH [Arber et al., 2015]. The PIC code solves Maxwell's equation together with the trajectories of individual particles. This approach assumed that a pre-plasma has been generated early within the pulse. And then, they modelled the interaction of the main pulse with this pre-plasma with ignoring the ionization during this modelling [Ardaneh et al., 2022a]. The PIC simulation result, as shown in figure 3.3, shows that it is possible to obtain 50% absorption with a defocusing that is nearly negligible only if the plasma is over-critical and the plasma is about 200 nm in diameter.

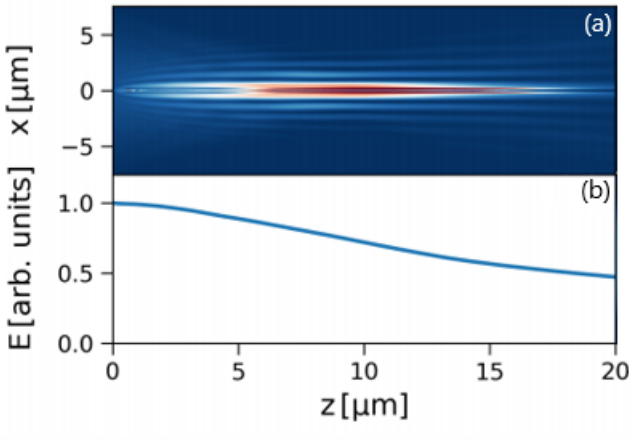


Figure 3.3: The nonlinear propagation intensity profile of Bessel beam inside 400 $\mu$m thick fused silica obtained from the PIC simulation, where (a) the fluence distribution and (b) the absorption along the propagation.

However, two key aspects could not be resolved. In brief, the PIC results of the fluence distribution show that a zero intensity region appears at the centre of the Bessel beam core, as shown in figure 3.7, and the outer Bessel beam lobes are shifting, as shown in figure 3.7, because of the wave-turning phenomenon. In contrast, the experimental results did not show any of them.

Therefore, the objective was to understand the reason of the two discrepancies (zero lobe shift) and the absence of the hole at the center of the fluence distribution. To provide a better understanding of the simulation results, we first review in the next section how the plasma is generated and how the laser interacts with a plasma with a density gradient.

## 3.2/ LASER-PLASMA INTERACTIONS

### 3.2.1/ PROPAGATION OF ELECTROMAGNETIC WAVES IN A PLASMA

In analyzing the laser-solid matter interaction, one has to consider several physical processes that occur in the solid matter under the influence of the electromagnetic field of the laser pulse. In the case of ultrashort, femtosecond laser pulses, the fast coupling of the laser field to the solid matter leads to rapid ionization within the first laser pulse cycles.

Depending on the pulse intensity, the ionization process occurs with different ionization rates and electron densities $n_e$. In this section, we will assume a plasma with spatially varying density with a characteristic scale length L, for instance, an exponential decay:

$$n_e(z) = n_{ec} exp\left(-\frac{z}{L}\right) \tag{3.1}$$

where $n_{ec}$ is the valence electron density in the solid and $L = |\nabla n_e(z)/n_{ec}|^{-1}$ is the scale length of the plasma profile.

The propagation of the laser electromagnetic field of frequency $\omega_L$ through the plasma is described by the dispersion relation, which can be derived in different approximations ac-

counting for the particular laser-plasma interaction conditions. Assuming the laser pulse propagation is perpendicular to a cold, collisionless plasma in the vacuum along the $z$-axis, the dispersion relation reads [Kruer, 2003]:

$$\omega_L^2 = \omega_p^2 + c^2 k^2 \tag{3.2}$$

where $\omega_p$ is the plasma frequency and given as:

$$\omega_p^2 = \frac{n_e e^2}{\epsilon_0 m_e}$$

The physical constants in the formula above are $e$- the electron charge, $m_e$- electron mass and $\epsilon_0$- the vacuum permittivity. The plasma frequency $\omega_p$ can be modified considering a plasma within dielectric has permittivity $\epsilon_\infty$ as [Cardona and Peter, 2005]:

$$\omega_p^2 = \frac{n_e e^2}{\epsilon_0 m_e \epsilon_\infty}$$

According to the dispersion relation 3.2 in a profile characterized by an electron density distribution $n_e(z)$, the laser can propagate ($k > 0$) up to a density called *critical density* $n_{ec}$ defined by the condition $\omega_L = \omega_p$ and given by the formula:

$$n_{ec} = \frac{\epsilon_0 m_e \epsilon_\infty}{e^2} . \omega_L^2 \tag{3.3}$$

### 3.2.2/ LASER INTERACTION WITH PLASMA GRADIENT

We briefly present here the interaction of a laser beam (plane wave) with a plasma gradient. Let us consider that the laser propagates and interacts with the plasma density at an angle. As shown in figure 3.4, the plasma-vacuum interface is chosen at $z = 0$, where the angle between the propagation vector $k$ and the plasma density is defined as $\theta_0$. Assuming that the laser propagates in the y-z plane (i.e., there are no variations in the x-direction). Thus, the wave vectors at vacuum-plasma interface are $k_y = (\omega/c)\sin\theta_0$ and $k_z = (\omega/c)\cos\theta_0$. Moreover, the electromagnetic field is defined as:

- s-polarization: $E = [E_x(y,z), 0, 0]; B = [0, B_y(y,z), B_z(y,z)]$
- p-polarization: $E = [0, E_y(y,z), E_z(y,z]; B = [B_x(y,z), 0, 0]$

The dispersion relation 3.2 becomes:

$$\omega_L^2 = \omega_p^2 + (k_y^2 + k_z^2)c^2$$

Solving the wave equations for the electromagnetic fields, one finds that there is an exponential decay of the field amplitude in the z-direction. This decay is seen as a refraction with a change in the direction of wave propagation and is called a turning wave phenomenon, as shown in figure 3.4. We analyze the interaction by solving Maxwell's equation for S and P-polarizations.

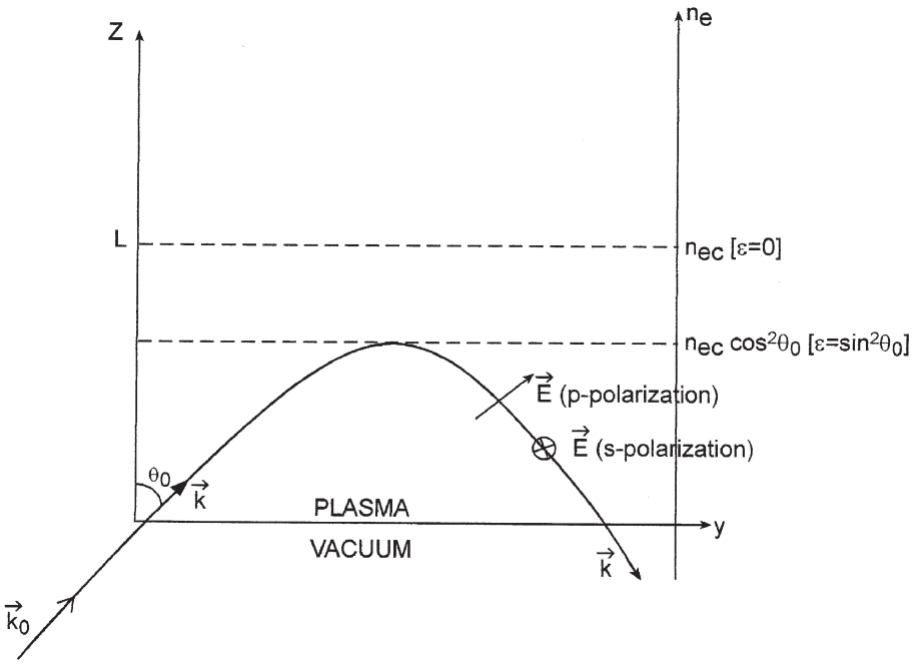


Figure 3.4: A sketch of a linearly polarized laser obliquely incident onto a plasma gradient $n_e(z)$ and the critical density $n_{ec}$. Figure from [Eliezer, 2002]

#### 3.2.2.1/ S-POLARIZATION

In this case, the electric field is in the x-direction and the wave equation becomes:

$$\frac{\partial^2 E_x}{\partial y^2} + \frac{\partial^2 E_x}{\partial z^2} + \frac{\omega^2 \epsilon(z)}{c^2} E_x = 0 \tag{3.4}$$

Since the dielectric function $\epsilon$ of the plasma is a function of z alone, $k_y$ must be conserved. Thus, the electric field can be written in the form

$$E_x = E(z) exp\left(\frac{i\omega y sin\theta_0}{c}\right) \tag{3.5}$$

Substituting Eq. 3.5 in Eq. 3.4 then gives

$$\frac{d^2 E(z)}{dz^2} + \frac{\omega^2}{c^2}\left(\epsilon(z) - sin^2\theta_0\right) E(z) = 0$$

Since $\epsilon = 1 - \omega_{pe}^2(z)/\omega^2$, reflection takes place where the plasma frequency $\omega_{pe} = \omega \cos\theta_0$. This means that the obliquely incident light wave reflects at a density lower than the critical density $n_e = n_{ec} cos^2\theta_0$ (i.e. in a plasma with a linear density profile, $n_e = n_{ec} z/L$, the wave reflects at $z = L cos^2\theta_0$. Moreover, the turning point occurs at a lower density when the incidence angle $\theta_0$ is increased.

The absorption coefficient is given as [Eliezer, 2002]:

$$f_a = 1 - \frac{I_{out}}{I_{in}} = 1 - exp\left(-\frac{32 v_c L cos^5\theta_0}{15c}\right) \tag{3.6}$$

where $v_c$ is the plasma collision frequency. Equation 3.6 is frequently used in the literature in order to understand the experimental results for the inverse Bremsstrahlung absorption.

#### 3.2.2.2/ P-POLARIZATION AND RESONANCE ABSORPTION

In this case, the wave-turning phenomenon occurs, but at the same time, another phenomenon occurs resonance absorption. As mentioned before, in the p-polarization case, there is a component of the electric vector which oscillates electrons along the direction of the density gradient. Since this oscillation generates fluctuations in charge density which the plasma can resonantly enhance, the wave is no longer purely electromagnetic. Part of the energy of the incident light wave is transferred to an electrostatic oscillation (electron plasma wave) in the vicinity of the critical surface, i.e. where the permittivity tends to zero, a phenomenon termed resonance absorption [Denisov, 1957]. The electron plasma wave is longitudinal: the electric field is parallel to the oscillation, in contrast with transverse electromagnetic waves. We remark that longitudinal electron plasma wave is bound to the plasma and, therefore, cannot propagate to a camera.

To determine the energy transfer to the excited plasma, we need to evaluate the amount of the electric field $E_d$, that pushes the electrons to oscillate along the density gradient at the critical density. i.e. the field that drives the resonance [Kruer, 2003].

$$E_d = \frac{E_{FS}}{\sqrt{2\pi\omega L/c}}\phi(\tau) \tag{3.7}$$

where $E_{FS}$ is the electric field of the light wave in free space and $\phi(\tau) \simeq 2.3\tau exp(-2\tau^3/3)$ with $\tau = (\omega L/c)^{1/3}\sin\theta_0$, as shown in figure 3.5. At a low incidence angle, the longitudinal component of the field is negligible, hence it cannot generate a significant electron plasma wave amplitude. On the other hand, very high incidence angles produce high longitudinal fields, but the amplitude of the evanescent input field decays very fast after the turning point: in this case, the amplitude of the driving field at the critical surface is again negligible. Between these two limits, there is an optimum angle of incidence given approximately by $(\omega L/c)^{1/3}\sin\theta_0 \simeq 0.8)$, as shown in figure 3.5.

The absorbed energy flux $I_{abs}$ is

$$I_{abs} \simeq \frac{\omega L E_d^2}{8} \tag{3.8}$$

Hence, the absorption coefficient is given as [Forslund et al., 1975]:

$$f_a = \frac{\omega L E_d^2}{8E_{in}^2} \tag{3.9}$$

The damping of this electron plasma wave is possible either by collisional or collision-less processes. However, the absorption due to resonance absorption is larger than the one due to inverse Bremsstrahlung for the following conditions: high plasma temperatures, i.e. high laser intensities; longer laser wavelength, and short plasma scale length, $L$, which is our case.

For a plasma dimension much higher than the laser wavelength, the resonant absorption is confined to a light incidence almost perpendicular ($\theta_0 \approx 0°$). In contrast, small plasma scales have peak resonance absorption at about $25°$ (see figure 3.5). The high electric field near the critical surface in these cases can accelerate electrons to energies much higher than the plasma temperature. Importantly, resonance absorption

and non-Maxwellian electron distribution can be physically captured by PIC codes in contrast with most of the other simulation codes.

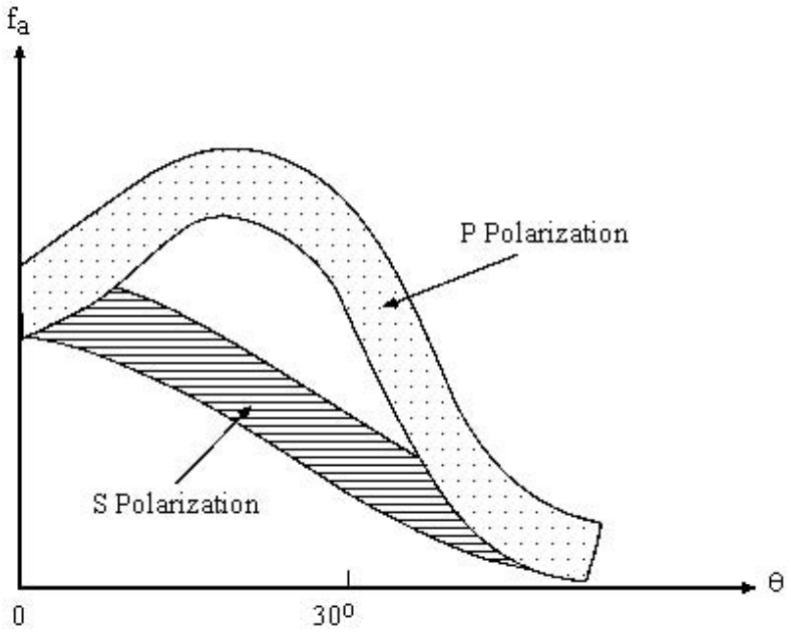


Figure 3.5: A sketch of absorption fraction for a p-polarized laser versus an s-polarized laser for a given laser intensity. Figure from [Eliezer, 2002]

## 3.3/ INDIRECT CHARACTERIZATION OF THE LASER-INDUCED PLASMA DENSITY

This section presents more details about our approach including the PIC simulation, the experimental setup overview, and the challenges we faced to enhance the quality of the experimental results.

### 3.3.1/ PARTICLE-IN-CELL SIMULATION RESULTS

The particle-in-cell method solves Maxwell's equations and the trajectories for groups of electrons. Ardaneh applied a conical phase $\Phi(r) = -(2\pi/\lambda)r\sin\theta_0$ to a Gaussian beam with a waist of $10\ \mu m$, as the experimental case, with a wavelength of $\lambda = 0.8\ \mu$m, and conical angle $\theta_0 = 25°$. The pulse duration of the beam is a Gaussian function with an FWHM of 100 fs. Moreover, he cropped the Gaussian beam window and reduced the Bessel beam length to $\approx 18\ \mu m$, to optimize the simulation run time. The peak intensity in the Bessel beam is set on the same order magnitude as in the experiments at $6 \times 10^{14}\ W/cm^2$ in absence of plasma.

Then, to match the far field distribution diagnostic, he defined the plasma as elliptical rods (the bigger diameter is in the polarization direction) with a plasma critical diameter of 200 nm in the X (polarization) direction and 70 nm in the Y direction. He has obtained results very similar to the experimental ones in terms of overall pulse absorption and

structure of the fields within fused silica and sapphire (figure 3.6). In the experimental investigation section, we use only sapphire samples.

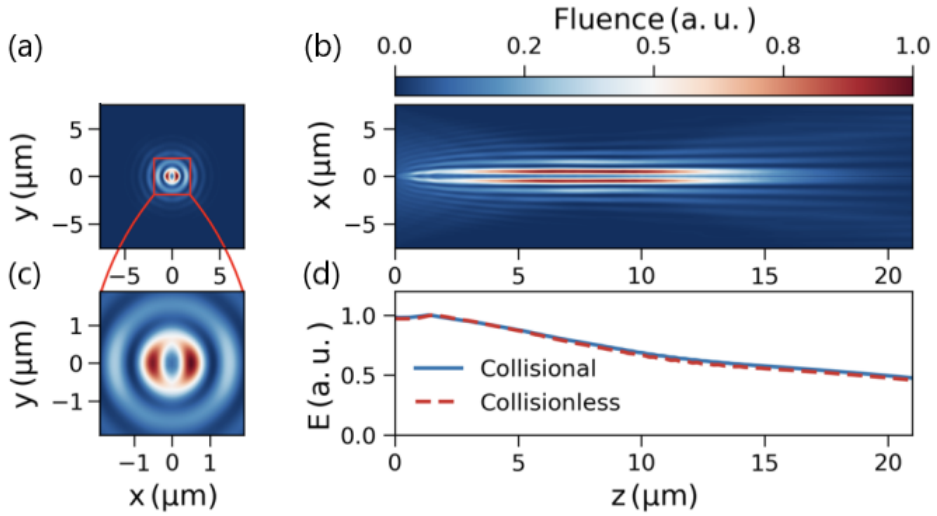


Figure 3.6: PIC simulation of the Bessel beam nonlinear propagation within sapphire, (a, and c) XY cross-sections, (b) XZ cross-sections, and (d) absorption along the propagation.

Figure 3.7 shows the numerical XY-cuts of the Bessel beam in (a) linear and (b) nonlinear regimes. As we see, we obtained a lobe shift of ≈ 250 nm because of the presence of a plasma with diameter ≈ 250 nm at the turning point density ($n(r) = 0.08\ n_{cr}$) for the Bessel beam angle.

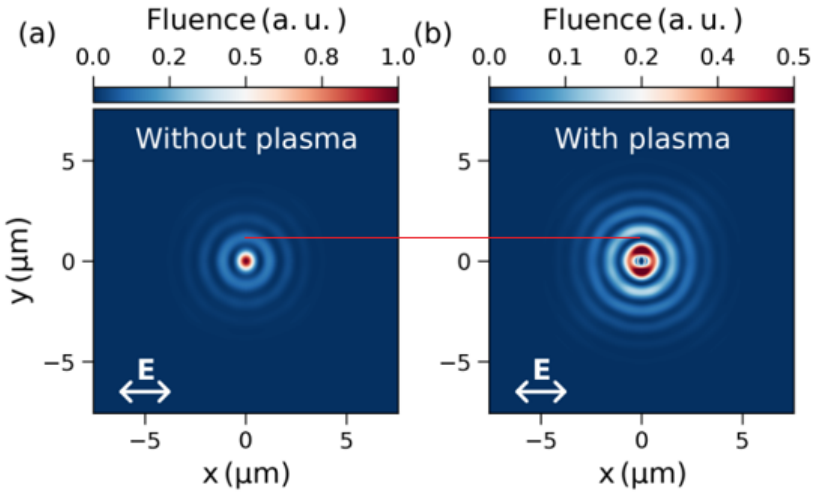


Figure 3.7: XY cross-section to show the central lobe of the Bessel beam and the Bessel beam lobe shift inside sapphire ($Al_2O_3$) by comparing between the PIC simulations: (a) without plasma and (b) with circular plasma rod.

### 3.3.2/ EXPERIMENTAL SETUP OVERVIEW

We use the same setup for the nanochannel formation which has been detailed in chapter 1, as shown in figure 1.17. We shape 120 fs Gaussian beam into a Bessel beam using SLM and a telescope with a de-magnification factor of 200 which produces a Bessel beam with cone angle 26°. The Bessel beam is imaged using a 100 times magnification telescope and CCD camera, as shown in figure 3.8. Then, after we ensure that the Bessel beam is well aligned with respect to the imaging system, we insert a dielectric sample perpendicularly to the beam with an angle smaller than 0.2 mrad.

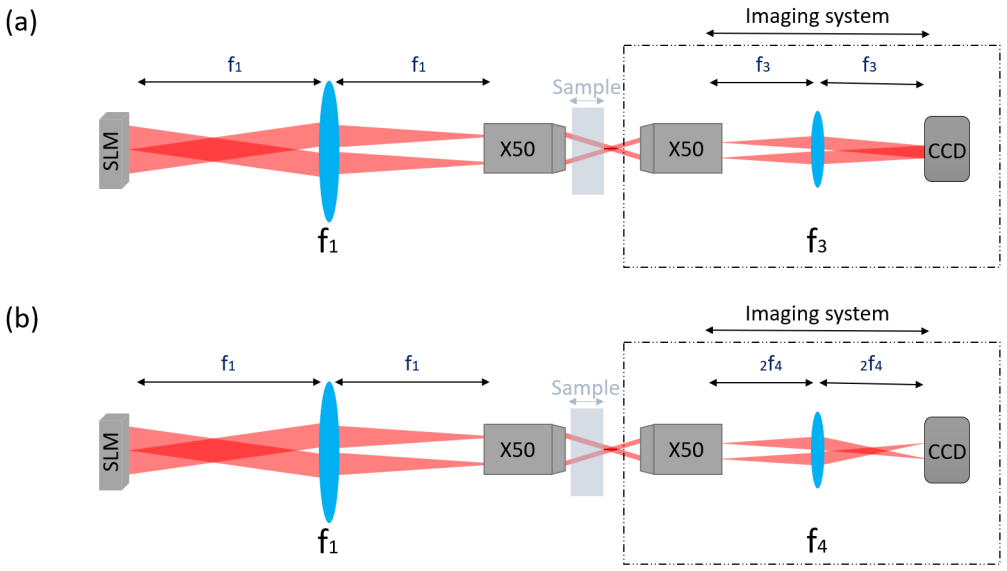


Figure 3.8: Single-shot setup detailed in chapter 1 figure 1.17 and the imaging system to observe Bessel beam at the sample back surfaces: (a) in the near-field using $f_3$ = 400 mm, and (b) in the far-field using $f_4$ = 200 mm.

The target of the experimental work is to extract two different information; the fluence profile in the near field, and the far field (Fourier) fluence distribution. Therefore, the lens in front of the camera has been placed on a magnetic mount that enables collecting the far-field pattern using the same imaging system by exchanging that lens with another one with half focal length (i.e. $f_3 = 2f_4$), as shown in figure 3.8(b). In this second case, the lens images the back focal plane of the microscope objective that collects the light after the sample. Because of the high magnification of the imaging system, the near field of the Bessel beam is not entirely imaged onto the camera surface. Therefore, to integrate the fluence distribution and measure the pulse energy on the camera, we use the far field distribution.

### 3.3.3/ POSITIONING ACCURACY ISSUE

Thanks to additional numerical simulations, we could understand that a small error in the positioning of the imaging system leads to a significant modification of the recorded fluence distribution, which hides the information about the wave-turning phenomenon.

#### 3.3.3.1/ SIMULATION OF THE IMAGED FIELDS

Remo Giust, in our group, has simulated the effect of mismatching the focal plane of the imaging system and the sample back-surface. In the configuration shown in figure 3.9, the back surface is not perfectly imaged onto the detector, and this leads to a deformation of the measured fluence distribution. For this, he has numerically simulated the propagation of the electromagnetic fields from the sample back surface to the CCD detector (note that this implies transferring the fields from the nonparaxial regime to the paraxial one). In this operation, he has taken into account the finiteness of the numerical aperture.

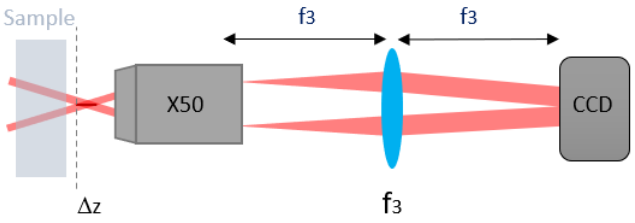


Figure 3.9: A mismatch between the imaging system plane [the vertical dashed line (¦)] and the sample back-surface with a shift distance $\Delta$ z ($\mu m$).

Figure 3.10 shows the results of a simulation for a variable mismatch $\Delta$z, where the fields are taken from the PIC simulation. In the simulations, he did not take into account the effect of the length of the plasma nor of the glass/air interface. The numerical scan shows that, at the center (dz = 0 $\mu$m), the lobe shift is there and we can see a hole in the axis of the distribution. This progressively disappears when $\Delta$z is just above 0.5 to 1 $\mu$m from the perfectly centered position.

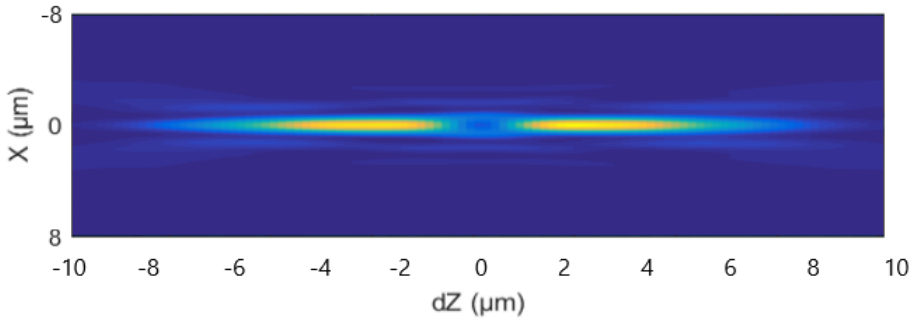


Figure 3.10: Numerical $\Delta$z-scan.

In figure 3.11, we show the same information for a selection of values of the mismatch $\Delta$z. We see that the position of the sample with respect to the microscope's objective focal plane is crucial. In the case of $\Delta$z = 0, we can see that the finiteness of the numerical aperture slightly blurs the central dip of the fluence computed with the PIC in the sample, but does not completely erases it. Because of the diffraction of the light, the hole within the central lobe disappears for $\Delta$z more than 0.5 $\mu$m, as shown in figure 3.11 (d). This is typically the error made on the positioning of our experimental imaging system. This

error originates first from the visualization of what is the ”perfect focus”, because it cannot be performed better than the Rayleigh range (0.5 $\mu$m in our case); and second, the repeatability of the positioning systems is typically 0.2 $\mu$m. Thus, the beam is imaged at the wrong position, for instance in air, the lobes will be shifted back as in the linear case, such that no lobe shift can be observed.

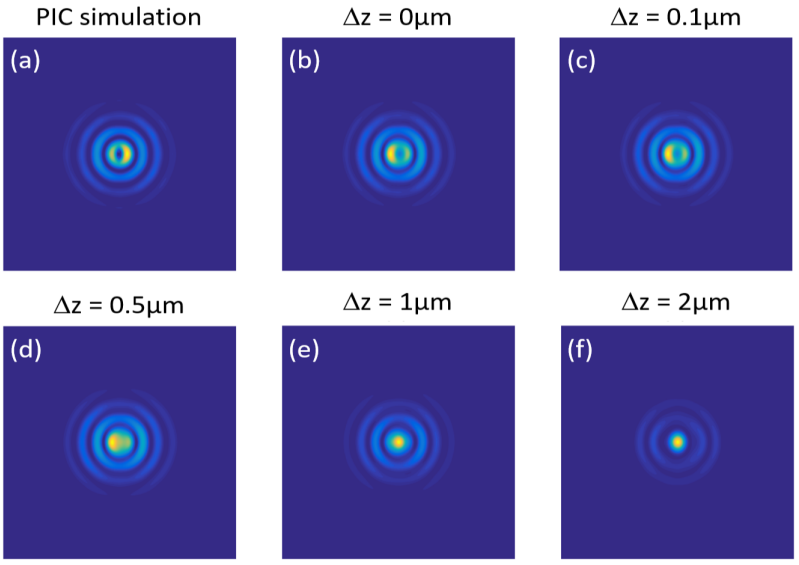


Figure 3.11: Mismatching effect on the collected data. (a) PIC data, (b-f) mismatching distance $\Delta z$ = 0, 0.1, 0.5, 1, and 2 $\mu$m, respectively.

#### 3.3.3.2/ EXPERIMENTAL INVESTIGATION OF THE POSITIONING IMPACT

In the experimental investigation, since we need to circumvent the positioning error mentioned above and shown in figure 3.10 for detecting the wave-turning phenomenon (i.e. the central lobe and the outer lobes shifting in PIC simulations), we have developed a strategy to scan with high resolution the beam around a fixed position of the sample.

We performed $\Delta z$-scan to detect the impact of the position on the observation of the Bessel beam-plasma interactions, as shown in figure 3.12(b). In the $\Delta z$-scan, we disable the sample movement (i.e. only the imaging system moves). Thus, to observe the interaction, we initially move the sample and the imaging system with the same distance in the direction that inserts the Bessel beam 10-20 $\mu$m inside the sample, i.e. at a distance where strong absorption occurs which corresponds to an expected high plasma density formation, as shown in figure 3.12(b).

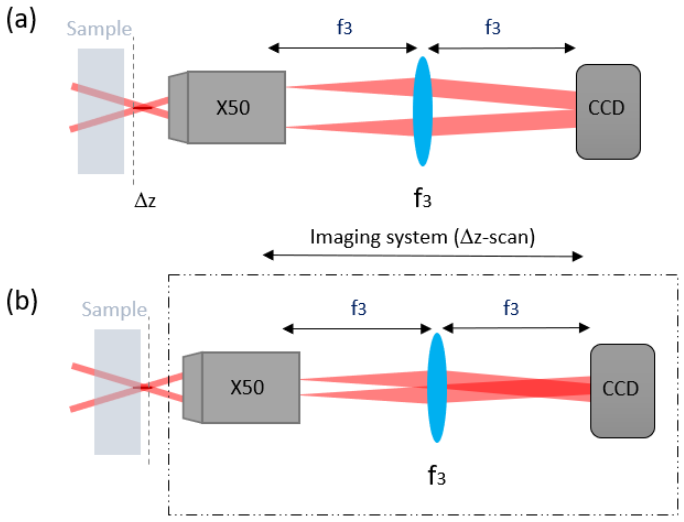


Figure 3.12: The positioning impact on the experimental result. (a) focusing on an ink mark, (b)Δz-scan to observe the positioning impact.

Around this configuration, we launched Δz-scans in a range of $\pm 4\mu$m with a movement step of 0.2 $\mu$m (guaranteed motion limit of our translation stage). We observed an interesting region (red dashed squares region in figure 3.13) away 2-3 $\mu$m from Δz = 0, which approximately corresponds to the ink height used for coarse alignment of the back surface. In the Bessel beam longitudinal Δz-scan, we detected a slight lobe shifting in the XZ-profile (figure 3.13(b)), where a blurred region in the YZ-profile (figure 3.13(d)) seen as a drop in the on-axis intensity (figure 3.13(c)).

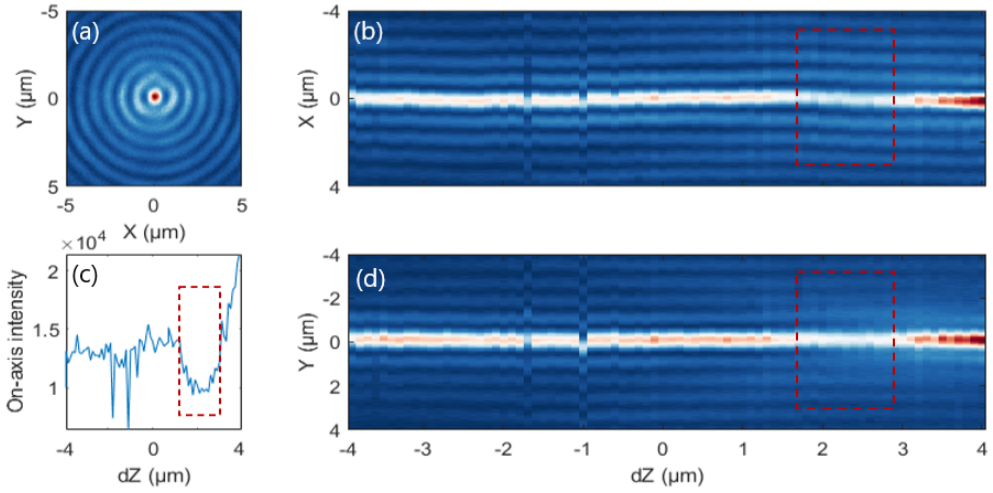


Figure 3.13: Δz-scan for the sample's initial position (focusing position on the ink where the Bessel beam starts to propagate). (a) XY cross-section at Δz = 2.6 $\mu$m (frame where the minimum on-axis intensity), (b) XZ cross-section along the Δz-scan, (c) on-axis intensity along the Δz-scan, and (d) YZ cross-section along the Δz-scan.

Comparing the numerical (figure 3.10) and experimental (figure 3.13) Δz-scans, we assumed that this region is the sample back surface. Therefore, we changed the sample's

initial position for shifting the dashed-square region in figure 3.13 toward the zero-dz position to compensate for the mismatch positioning. We optimized the sample's position by performing several $\Delta$z-scans and bringing the on-axis intensity's drop to $\Delta z = 0$.

Importantly, this characteristic behaviour disappears when the beam insertion corresponds to positions where no plasma is expected, from the absorption curve.

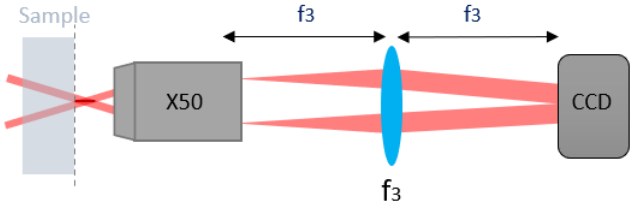


Figure 3.14: Shifting the red dashed squares region in figure 3.13 to $\Delta z = 0$ by changing the sample's initial position and repeat $\Delta$z-scan.

To confirm that the slight lobe shift seen in figure 3.13(b) is the wave-turning phenomenon we are searching, we traced the shift with different pulse energies by performing several $\Delta$z-scans at the new sample's position in figure 3.14.

Figure 3.15 shows a typical 8 $\mu$m range $\Delta$z-scan within sapphire after minimizing the positioning mismatch below 1 $\mu$m at pulse energies (a) 1 $\mu$J, (b) 2 $\mu$J, and (c) 2.5 $\mu$J. In figure 3.15, we can observe the fluence in the central core is low in the range from -4 to 0 $\mu$m, then it increases suddenly. From that, we can confirm that the sample back surface is at $\approx$ 0 $\mu$m. Because the low intensity is due to the occurred absorption within the sapphire and the high-intensity part is outside the sample because there, the central core is not absorbed.

Moreover, we can see clearly that the first outer lobe of the Bessel beam is getting broader in the X-direction (parallel to the pulse polarization) by scanning the beam closer to the sample back surface (i.e. dz = 0 $\mu$m), as predicted from the numerical $\Delta$z-scan (figure 3.10). In figure 3.16, we plot the evolution of the lobe shift with the pulse energy in the X-direction with an error bar of $\pm$ 40 nm.

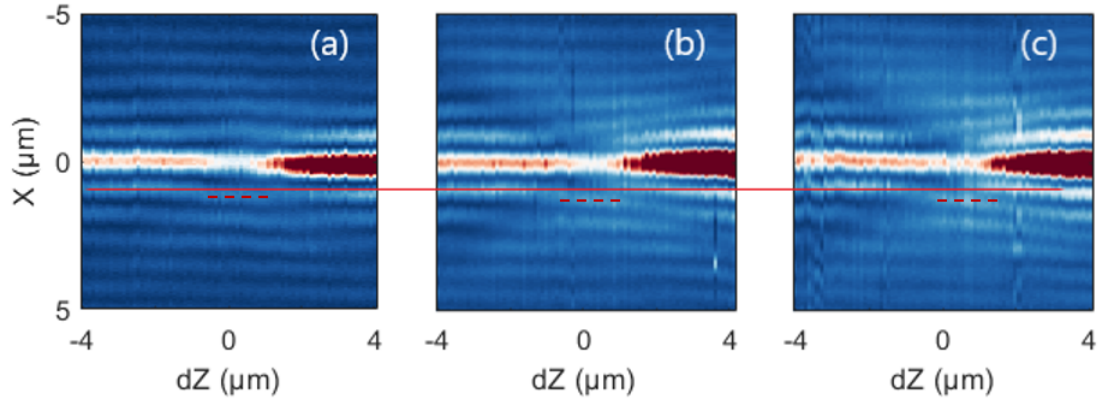


Figure 3.15: The effect of the pulse energy on the $\Delta$z-scan. (a) 1 $\mu$J, (b) 2 $\mu$J, and (c) 2.5 $\mu$J. the color map is saturated to see the Bessel lobes clearly.

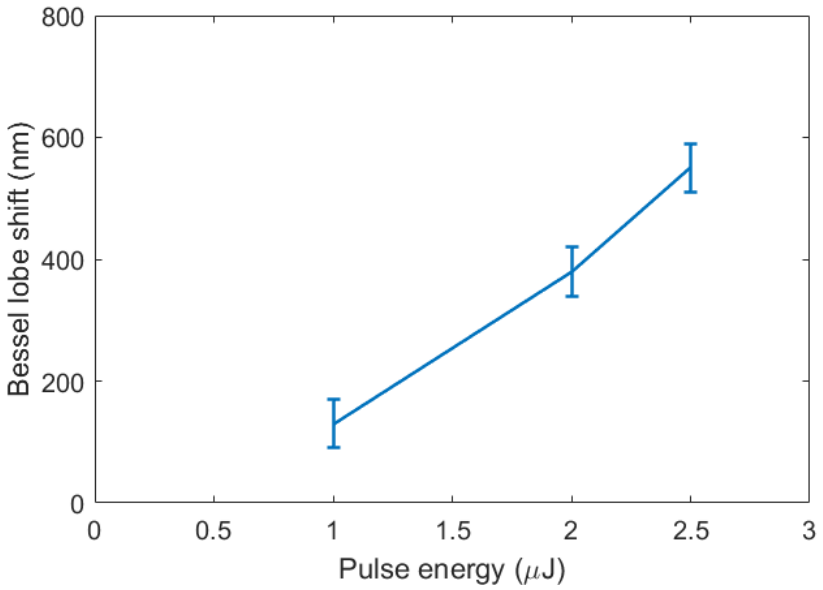


Figure 3.16: The evolution of the lobe shift in X-direction with the pulse energy.

From the lobe shift and the absorption observation, we can say that the sample is placed at a good position, where the mismatch $\Delta z \approx 0$ $\mu$m $\pm$100 nm.

## 3.4/ DIAGNOSTICS

In this section, we present the acquired data after following the high accurate positioning procedure. In the beginning, we verified the generation of over-critical dense plasma by observing the wave-turning phenomenon. In this experimental results, we used 150 $\mu$m thick C-cut sapphire $Al_2O_3$ interacting with Bessel pulse using several pulse energies up to 3 $\mu$J with different polarization states. The absorbed energies we obtained were enough to generate and emit second harmonic signal.

### 3.4.1/ WAVE-TURNING

After we ensured that the imaging system is focusing on the sample's back surface in a precision of less than 1 $\mu$m, as shown in figure 3.15, we performed the single-shot-sectioning scan to observe the nonlinear interaction of the Bessel pulse with the plasma rod that was generated with the front of the pulse.

We propagated a 120 fs horizontally polarized Bessel beam with pulse energy of 2 $\mu$J within a 150 $\mu$m thick C-cut sapphire $Al_2O_3$. In figure 3.17, we present an experimental XZ cross-section of the near field fluence imaging without (figure 3.17 (a)) and with (figure 3.17(b)) considering the new strategy of sample positioning. (i.e. old and recent results). The difference is apparently relatively weak, but we will see that the analysis of the transverse cross-section can demonstrate the existence of lobe shift between linear and nonlinear regimes.

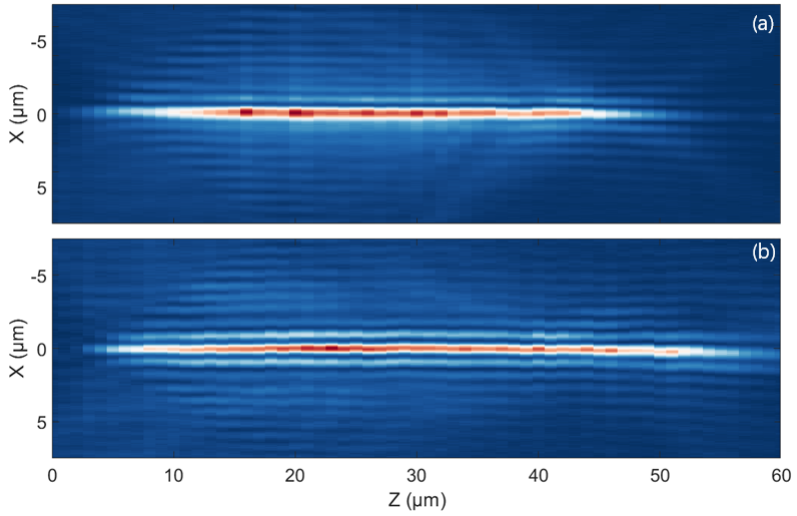


Figure 3.17: Comparison of the experimental near field fluence of a femtosecond Bessel pulse propagating in sapphire before (a) and after (b) considering the positioning impact.

Figure 3.18 show XY cross-section of the Bessel beam during its propagation in linear (i.e. very weak energy) and nonlinear regime figure 3.18 (a) and (b), respectively, for the same position of the sample. We can see clearly that, in the nonlinear case, the outer Bessel lobe is elongated with a relative decrease of the fluence in the direction perpendicular to the polarization.

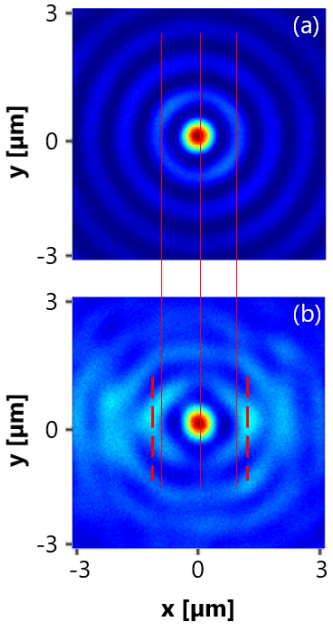


Figure 3.18: XY cross-section of the Bessel beam propagating within sapphire in linear (a), and nonlinear regime (b) to show the wave-turning phenomenon which is predicted by PIC simulations.

These results allow us to confirm that plasmas generated by the Bessel beam in the nanochannel drilling configuration are effectively over-critical and that the energy deposition process is due to the resonance absorption.

However, we could never observe the ”hole”, that was predicted by the PIC simulation within the central lobe. This can be due to the positioning accuracy (±100 nm) as well as due to the dynamical effect since the ionization dynamics is not taken into account in the PIC simulation. Just recently, Pierre-Jean Charpin, PhD student in our group, simulated the fluence considering the ionization dynamics and he obtained that the central hole disappears in one of the simulations.

### 3.4.2/ SECOND HARMONIC GENERATION

Second harmonic generation is conventionally an important diagnostic in the study of laser-plasma interaction. Remi Meyer could observe for the first time the emission of the second harmonic, which is a good complementary confirmation that the plasma generated by the Bessel beam is over-critical. Therefore, this work is focusing on the study of the second harmonic generation during the interaction of an ultrafast Bessel beam pulse with a plasma rod. We are using the same setup in figure 1.17(b). For the data acquisition, as shown in figure 3.19, we use the far-field imaging configuration as in figure 3.8 (b) to collect the entire emitted signal by inserting a bandpass filter for the spectral range of 400±20 nm in front of the camera.

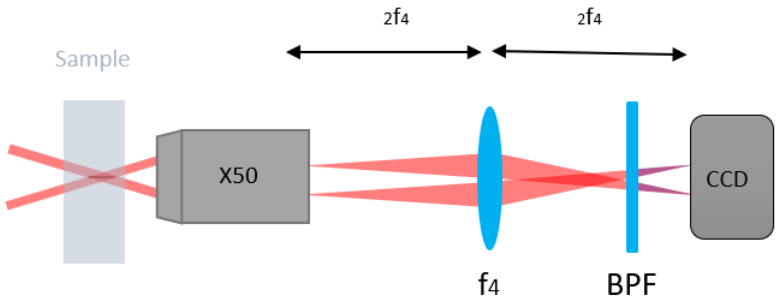


Figure 3.19: Experimental setup to characterize the presence of second harmonic generation in a single shot.

The second harmonic signal generated from a single pulse is too weak to be detected by our imaging system. Therefore, we integrate the obtained signal over ≈ 500 shots by using the laser in the continuous mode (1 kHz repetition rate) and moving the sample, simultaneously, along 10 mm in X or Y direction. The distance between neighbouring shots is ≈ 20 $\mu$m (i.e. they are quasi-independent of each other). Moreover, as shown in figure 3.19, the Bessel beam is longitudinally placed in the centre of the sample to maximize the nonlinear interactions.

Figure 3.20 shows a typical experimental result obtained using a horizontally polarized Bessel pulse with an incident energy of 2 $\mu$J and 120 fs pulse duration. The distribution is limited by the numerical aperture of the microscope objective and composed of a low-intensity background that is unpolarized and that we attribute to blackbody radiation, and of a thin second harmonic emission at an angle quasi-identical to the 800 nm pattern.

Moreover, we observed a black line (red dashed squares) at the centre that originates from the neighbouring channels. In figure 3.20 (a) and (b), we show identical pictures obtained, one with translation along the y and the other with translation along the x-direction, respectively. The dark pattern will change its direction, but the thin lobe pattern is maintained. We have remarked that the second harmonic signal disappears when the input pulse is stretched to ps pulse durations.

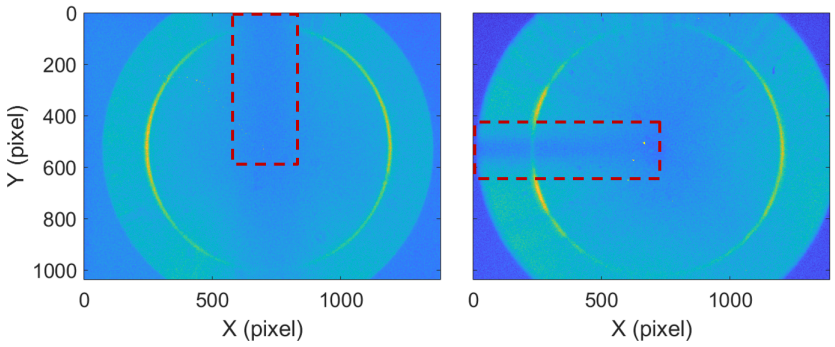


Figure 3.20: The capture of 400 nm signal, averaged over ≈ 500 pulses and detected by the imaging setup in figure 3.19 with different direction of sample's translation, along (a) y-axis and (b) x-axis.

### 3.4.2.1/ Evolution of the second harmonic generation with pulse energy

The second harmonic emission is affected by the incident pulse intensity. From the equation of motion and continuity equation for electrons coupled with the Maxwell equations, we can obtain the associated second-order current density as follow [Shen, 1984]:

$$\mathbf{J}^{(2\omega_0)} = -\frac{jne^3}{4m^2\omega_0^3}\left[4\frac{\nabla ln\, n.\mathbf{E}}{\epsilon}\mathbf{E} + \nabla(\mathbf{E}.\mathbf{E})\right] \tag{3.10}$$

We detected different emission intensities by using several pulse energies 1, 2, and 3 $\mu$J. It is not possible to detect the signal using pulse energy less than 1 $\mu$J probably because of the absence of overcritical plasma. Equation 3.10 shows that the current is proportional to energy, but the signal that we measure on the camera is the square of the current. Therefore, we expect a quadratic dependence. As shown in figure 3.21, as expected from Eq. 3.10, we found that the second harmonic signal intensity increases with the incident pulse energy.

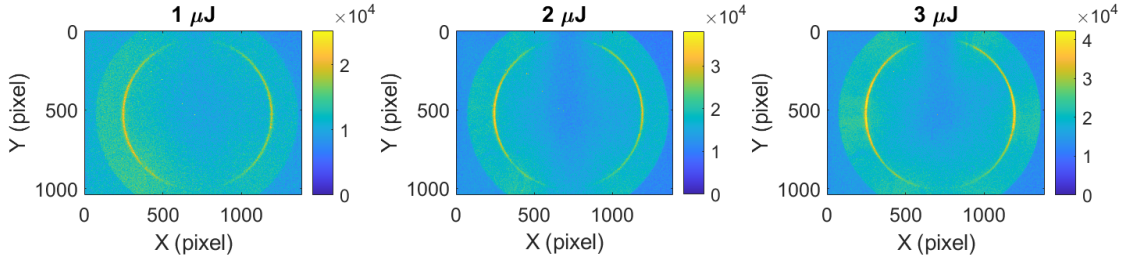


Figure 3.21: Second harmonic generation signals obtained using different incident pulse energies 1, 2, and 3 $\mu$J from left to right, respectively

#### 3.4.2.2/ EVOLUTION OF THE SECOND HARMONIC SIGNAL AS A FUNCTION OF THE INPUT POLARIZATION

We study, in this sub-section, the direction of the second harmonic signal with changing the polarization state of the incident beam. We found that second-harmonic lobes are oriented parallel to the incident beam polarization, as shown in figure 3.22. In the horizontally polarized incident pulse case, we observed two parallel lobes are oriented on the horizontal axis, as shown in figure 3.22(a). The two parallel lobes are rotating with the incident pulse polarization. By using a vertically polarized pulse, the lobes rotated to the vertical axis (figure 3.22(b)). In figure 3.22(c), the signal is obtained by rotating the pulse polarization at 45°. Moreover, we acquired a complete ring by using a circular polarized Bessel beam, as shown in figure 3.22(d).

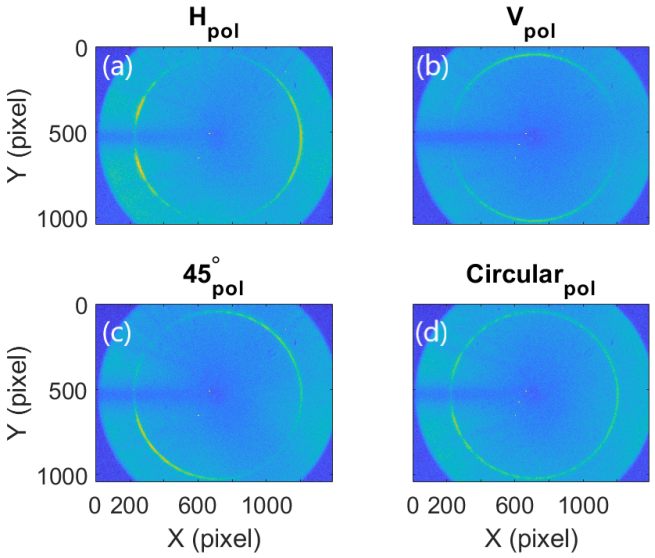


Figure 3.22: second harmonic generation patterns obtained by using different incident pulse polarization: (a) horizontal polarization, (b)vertical polarization, (c)45° polarization, and (d) circular polarization

#### 3.4.2.3/ ANALYSIS OF THE POLARIZATION STATE OF THE SECOND HARMONIC SIGNAL

From Eq.3.10, the first term gives a second harmonic emission with parallel polarization relative to the input laser by using a linearly polarized laser that interacts with a radial density plasma profile $P^{(2\omega_0)} \propto \mathbf{E}(r.E)$. On the other hand, the second term in the $P^{(2\omega_0)}$ expression gives second-harmonic with polarization determined by the gradient of intensity distribution, whatever the polarization of the input laser. Thus, we studied the polarization of the acquired second harmonic signals.

In the emission pattern in figure 3.23(a), the two parallel lobes are oriented along with the direction ±E of the input laser. To determine the polarization of the lobes, we inserted a polarizer in the imaging system. For the component filtered by a horizontal polarizer ($H_{Pol}$), in 3.23(b), we obtained the same pattern as without a polarizer, but with less intensity leading to the SH-pattern having a dominant component polarized as the input laser pulse. However, there is also a faint component that is polarized perpendicular to the input laser pulse (vertical polarization) with a quadrupole-shape pattern, figure 3.23(c). The average power of the second-harmonic with the horizontal and vertical polarizations are 80 and 20% of the $I^{(2\omega_0)}$, respectively.

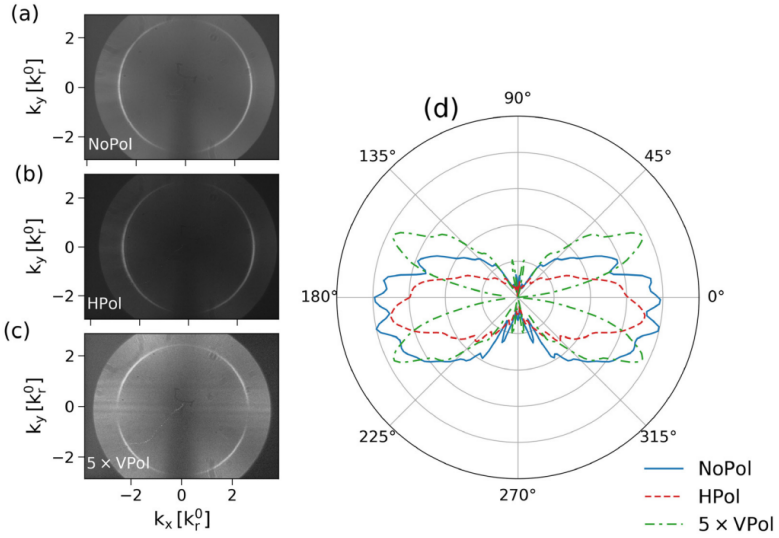


Figure 3.23: Far-field emission at $2\omega_0$ from the experiments: (a) without polarizer ($No_{Pol}$), (b) using a horizontal polarizer ($H_{Pol}$), and (c) using a vertical polarizer ($V_{Pol}$). The axes are normalized to $k_0 r = k_0 sin\theta_0$. The angular distribution for each distribution is shown in panel (d), blue solid for $No_{Pol}$, red dashed for horizontal polarization, and green dashed-dotted for vertical polarization. Figure from [Ardaneh et al., 2022b]

#### 3.4.2.4/ SECOND HARMONIC SIGNALS USING PIC SIMULATIONS

The PIC simulations predicted the second harmonic pattern that we obtained experimentally and presented in the previous sections. Ardaneh has performed the simulations by defining the plasma with Gaussian and step density profiles provided to use a plasma with an elliptical beam shape oriented perpendicular to the input polarization [Ardaneh et al., 2022b]. The second harmonic patterns from both profiles were close and in excellent agreement with the experimental pattern, as shown in figure 3.24. Sub-figures

3.24 (a), (b), and (c) show a comparison between the angular distributions experiments and two different transverse density profiles (Gaussian and step) for the cases No$_{Pol}$, horizontal polarization, and vertical polarization, respectively.

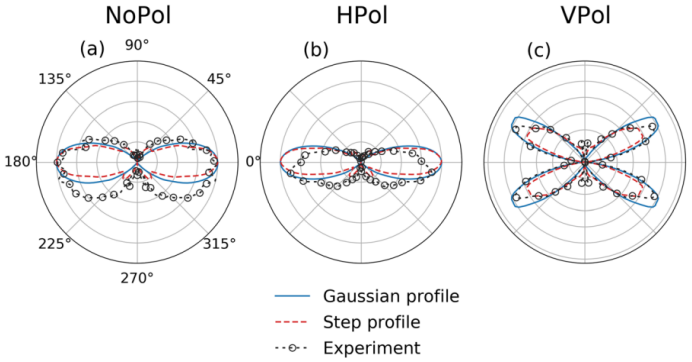


Figure 3.24: The angular distributions are shown in panel (a) for No$_{Pol}$, (b) for horizontal polarization, and (c) for vertical polarization, blue solid for Gaussian density profile, red dashed for step density profile, and black dotted with empty circles for the experiment.

In figure 3.25, we present the experimental and numerical far-field emissions in the left, and right columns, respectively. The $2\omega_0$ emission patterns are shown: (a) and (d) for mixed polarization (No$_{Pol}$), (b) and (e) for horizontal polarization, (c) and (f) for vertical polarization. The axes are normalized to $k_0 r = k_0 sin\theta_0$ of the Bessel beam. The colorbars are normalized by the average power of input pulse.

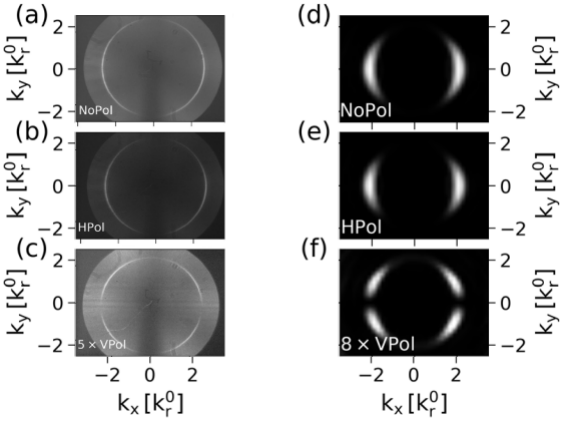


Figure 3.25: Far-field emission at $2\omega_0$ from the experiment (left column), and PIC simulations for the Gaussian density profile (right column).

As shown in the previous results, we obtained an excellent quantitative agreement on the amplitude of the signals but also on the spatial patterns. This shows that we have captured correctly the plasma density shape.

## 3.5/ CONCLUSION

In this chapter, we have solved key remaining issues on optical diagnostics: we could quantitatively evaluate the position of the wave turning point inside the plasma generated by the Bessel beam, and show that the plasma is very thin. The excellent agreement obtained for the near field distribution of the pump as well as those obtained for the second harmonic generation confirms that we have captured the physics at play during energy deposition by the femtosecond Bessel pulse propagating inside sapphire.

We have demonstrated, for the first time to our knowledge, single ultrafast Bessel pulses, with energy ranges exceeding the nanochannel formation threshold, generate overcritical nanoplasma within the bulk of sapphire. The generated plasma interacts with the pulse tail and induces resonance absorption accounting for most of the 50% absorption, hence which is the key process for energy deposition. Moreover, we confirmed the resonance absorption by observing the second harmonic emission from the bulk of sapphire and studying the second harmonic pattern direction and polarization.

Yet powerful, this technique requires heavy numerical simulations to compare with experiments. In addition, the diagnostics used in this chapter cannot provide information on the plasma buildup during the pulse. Therefore, the next chapter will be dedicated to the development of a new approach to measure the dynamics of the plasma buildup within Bessel beams.

# 4

# PUMP-PROBE MEASUREMENT OF NANO-PLASMA DENSITY

The generation of plasma is inherent to a number of applications of ultrafast laser pulses. As mentioned earlier, the generated plasma is essential to transfer the laser energy into the solid, which is crucial for various applications. It is also essential for fundamental investigations on the generation of extreme pressures such as the one of warm dense matter that is the state of matter in the core of several astrophysical objects, e.g., planets and stars.

However, to understand these fundamental processes it is crucial to the quantify the distribution of the laser-generated plasma density in space and time. The measurements presented in the previous chapter show the result of interacting ultrafast Bessel beam with dielectrics without the dynamics with time. Thus, this chapter concerns the next step in this direction. After confirming the generation of overcritical plasma density, we are carrying out a pump-probe imaging experiment to determine the parameters of the generated plasma by Bessel beams. Moreover, we can circumvent the opaqueness of the plasma rod by illuminating it ”from the sides”, i.e. using a probe shaped as a Bessel beam. Assuming invariance of the distribution along the propagation direction, we are mainly interested in two quantities: density and spatial extent.

The imaging used in this experiment allows for measuring the diameter of the generated plasma. The first section discusses some current techniques for plasma imaging and their limitations. After that, we present our approach, followed by the challenges we faced during implementing the new setup and how to solve them. Finally, we provide preliminary results obtained using this new approach.

## 4.1/ CURRENT TECHNIQUES

Imaging of laser-induced phenomena in glass is of interest to several research groups due to the need to determine suitable irradiation conditions in femtosecond laser processing. Most of the current techniques are based on pump-probe imaging. This section discusses some of these imaging techniques and their limitations.

One of the techniques is called shadowgraphy. In this technique, the plasma is transversely illuminated with a probe pulse, as shown in figure 4.1(left) [Yu et al., 2015]. It

is well adapted to evaluate propagation speeds, such as shock waves emitted. In this approach, the refractive index change $\Delta(n)$ is calculated from the transmission $T = e^{-4\pi\Im[\Delta(n)]L/\lambda_{probe}}$ of the probe through plasma of thickness $L$. The limitation of this technique is that it is still required to estimate the plasma thickness [Papazoglou et al., 2007], which is one of the targets in the plasma parameters measuring work.

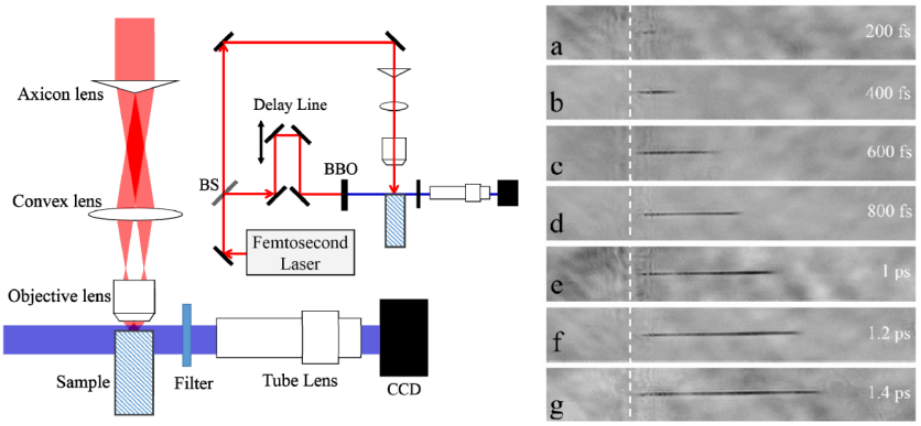


Figure 4.1: Pump-probe shadowgraphy technique: (left) the setup scheme and (right) the dynamics of Bessel beam drilling within PMMA. Figure from [Yu et al., 2015]

In 2004, Mao et al. reported a spectral interferometry technique that uses a probe pulse and a reference pulse separated with a delay of more than their duration using a Michelson interferometer, as shown in figure 4.2, [Mao et al., 2004]. The idea is to probe the system by the first pulse before the pump, thus used as a reference pulse. Then, the second pulse probes the pump's effect on the system leading to a relative phase $\Delta\Phi(t)$ between the two probes. Although this technique is precise, it is limited by characterising one spatial dimension. It also fails when the plasma is over-critical since the amplitude of the fringes would decrease to zero.

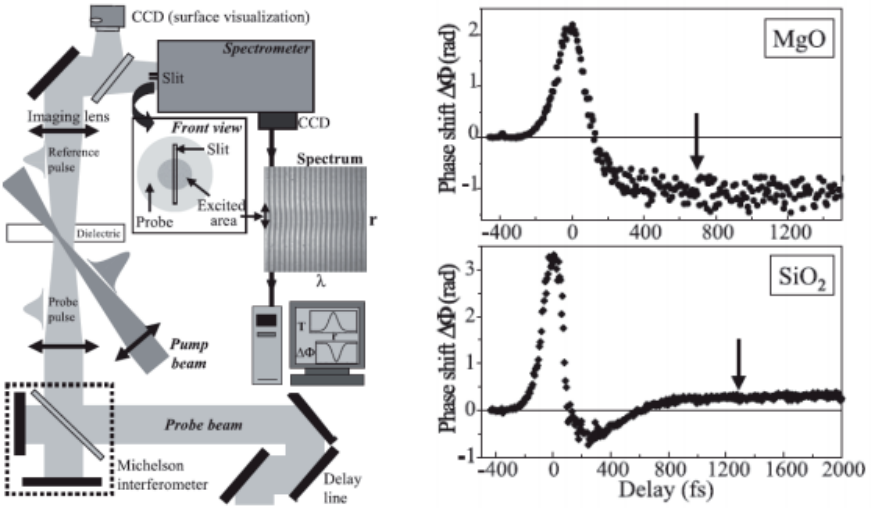


Figure 4.2: Pump-probe spectral interferometry technique: (left) the setup scheme and (right) the phase shift in delay profiles in fused silica ($SiO_2$) and magnesium oxide (MgO). Figure from [Mao et al., 2004].

Hayasaki et al. proposed another interferometry approach [Hayasaki et al., 2017]. This time their interferometer is placed after the interaction. They also use two probe beams, each leading to an interferometric measurement. In this technique, the excitation is observed from the side, as shown in figure 4.3. Thanks to holography, it is possible to decouple the sample's phase and absorption information and then exploit the absorption ratio at 800 and 400 nm to retrieve the plasma collision time. They then measure the plasma decay and extract the glass's characteristic time of 150 fs.

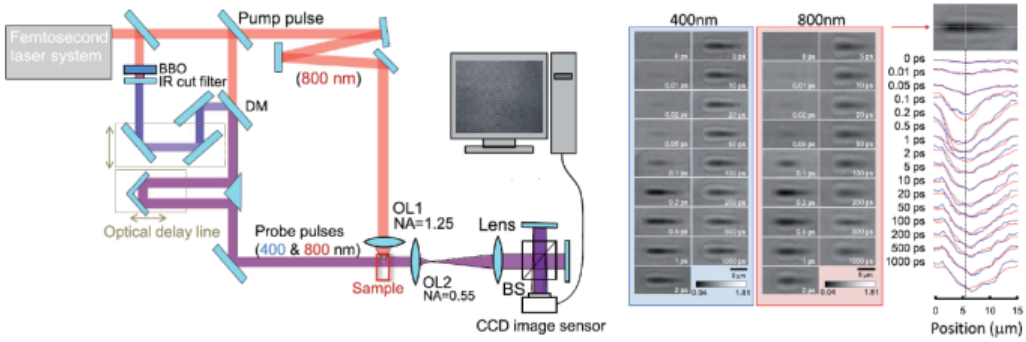


Figure 4.3: Two-color pump-probe interferometry technique: (left) the setup scheme and (right) the constructed absorption profiles by 400 and 800nm. Figure from [Hayasaki et al., 2017].

Recently, using a similar interferometry concept, Bergner et al. combined the plasma-related absorption information with a time-resolved side-view mapping of the refractive index variation, as shown in figure 4.4, using Wollaston prisms to form the interferogram on the camera [Bergner et al., 2018]. The knowledge of the refractive index is of pronounced interest and allows to decouple of the physical effects at play at a given time (e.g., $\Delta n > 0$ for the Kerr effect and $\Delta n < 0$ for the plasma).

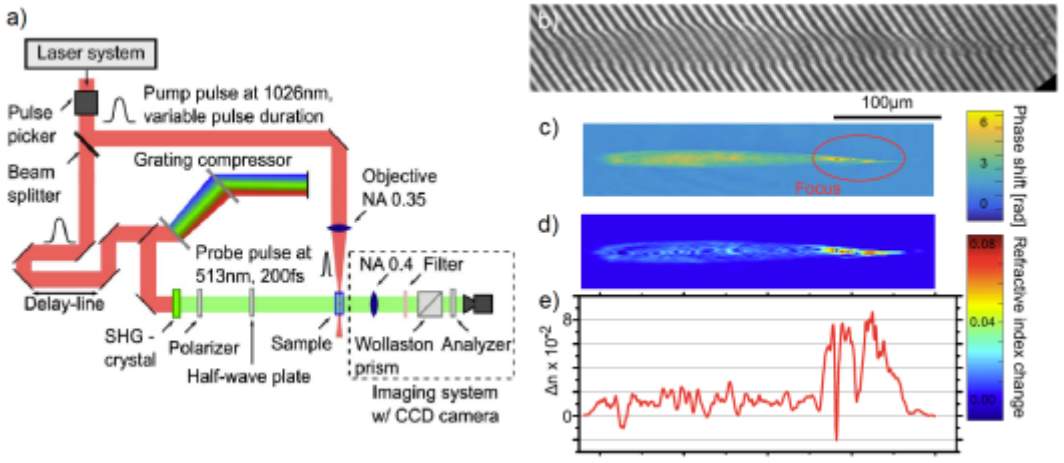


Figure 4.4: Hologram formation interferometry technique: a) the setup scheme, b) pump-probe interference imaging, c) reconstructed phase shift, d) two-dimensional refractive index and e) reconstruction for different pump-probe delays. Figure from [Bergner et al., 2018].

However, due to the limitations for the phase reconstruction, especially when the collected intensity is zero, leading to a phase ambiguity. The self-referenced interferometry in [Hayasaki et al., 2017, Bergner et al., 2018] fails to describe our plasma density and dimension.

In our group, Meyer has designed, built and started to operate an interferometric pump-probe experiment with a pump pulse shaped into a Bessel beam [Meyer, 2020]. He imaged the hologram of the probe pulse propagating in the medium collinearly to the Bessel beam axis, for different pump-probe delays and at different positions, as shown in figure 4.5. By digital demodulation, Meyer extracted the complex amplitude of the probe pulse passing through the medium to be studied. And then, from the propagation equation in an inhomogeneous medium, he established an approximate Helmholtz equation for the probe wave. Spatially, the measurements seemed relevant because the velocities of the shock waves generated by the laser pulse are in good agreement with the literature (see figure 4.5(bottom)). On the other hand, the index extracted from the reconstruction algorithm seems quantitatively unreliable. In practice, the measurement of the index is quite complex because of the sensitivity to noise in the experiment. Therefore, the technique was unable to provide us with the necessary quantitative information to evaluate the plasma density distribution.

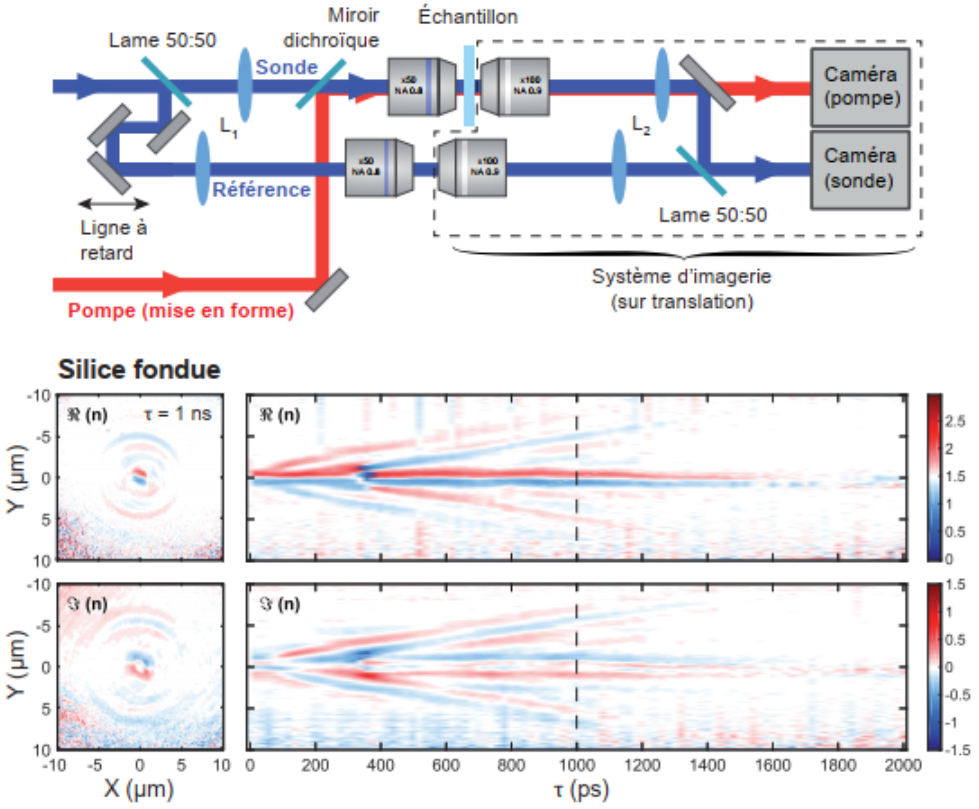


Figure 4.5: Hologram formation interferometry technique by our group: (top) the setup scheme, (bottom) the refractive index reconstruction for different pump-probe delays. Figure from [Meyer, 2020].

Moreover, in parallel to the interferometry measurements, Meyer worked on another complementary experiment to overcome the quantitative lack of the density of the plasma

reached. The experiment is based on measuring, by solving Maxwell's equations, the change of index diameter attributed to the plasma, realized thanks to the pump-probe experiment. A comparative approach experiment-simulation on the signal of self-reflection of the pump wave on the generated plasma allows us to estimate the order of magnitude of this density and to place it for the energy of 1 $\mu$J between 0.5 and 1.5 times the critical density.

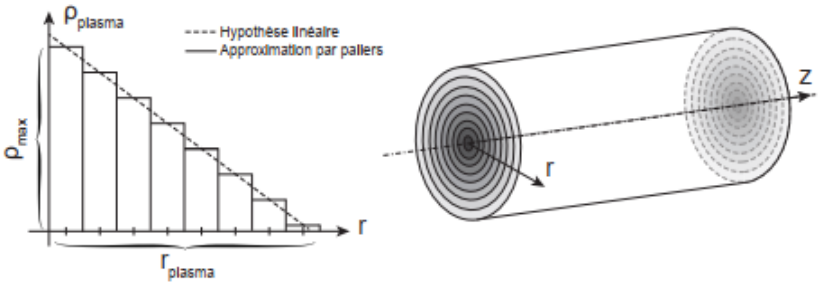


Figure 4.6: Solving Maxwell's equations for a given plasma density in cylindrical volume. Figure adapted from [Meyer, 2020].

## 4.2/ Our approach: probing the plasma using ultrafast higher-order Bessel beams

Since one of the key problems of probing nanoplasmas that have an over-critical density is that they block the propagation of the probe, we used the fact that Bessel beams propagate from the sides toward the center. The complex reflectivity of probe pulses shaped as Bessel beams is expected to provide information on the plasma distribution.

In this section, we provide a novel technique to retrieve the peak plasma density, plasma radius and collision time ($\tau_c$), that are generated by a single pulse of circularly polarized Bessel beam.

### 4.2.1/ The concept

Remo Giust, in our group, has developed the code that solves Maxwell's equation in cylindrical coordinates, shown in figure 4.6, for a pre-defined plasma density distribution, to obtain the reflection coefficient in amplitude and phase of a probe shaped into a Bessel beam knowing the input Bessel angle and order. The plasma permittivity is modelled by the Drude model and the concept is to solve the multi-layer system in cylindrical geometry.

The fundamental modes of interaction between a conical wave and a cylindrical plasma density distribution are based on either radial or azimuthal polarization. This is equivalent to the TE and TM modes to analyze the interaction of plane waves with one-dimensional plasma gradients.

Therefore, here, we use a series of higher-order Bessel beam-shaped probes to improve the pump-probe imaging resolution, as shown in figure 4.7. The Bessel beam parameters, such as its angle and order, will control the overlap between the pump and the probe beams. Thus, we expect that probing the laser-generated plasma with the Bessel beam

will significantly improve the sensitivity of imaging the change in amplitude by acquiring the probe absorption as a function of Bessel (order, angle).

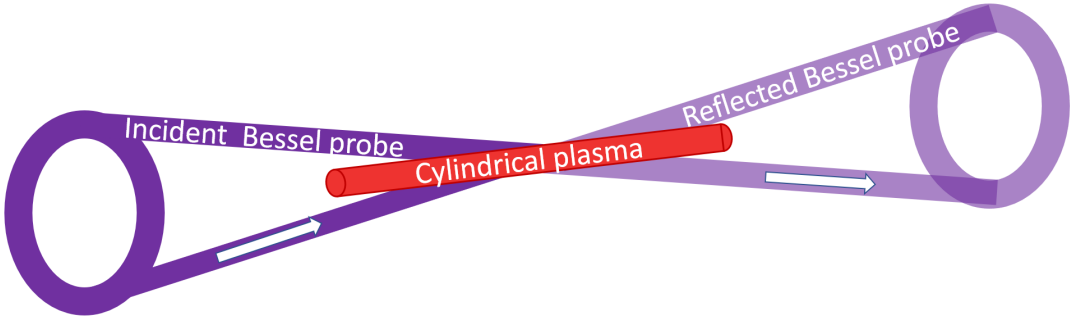


Figure 4.7: The concept of interacting a Bessel probe beam with a cylindrical plasma obtained with a 26° Bessel pump beam.

Remo Giust showed that using a higher-order Bessel probe symmetrically polarized (radial or azimuthal) interacting with a cylindrical plasma will change its local polarization phase. This is seen as a rotation of the far-field pattern after a polarizer, and the amount of rotation depends on the Bessel order. Indeed, the higher order Bessel beam, because the optical rays are twisted, is not perfectly pure radial or azimuthal polarization. A key aspect is that the phase of the reflection coefficient is different for the two polarization components. The dephasing can be observed by a modification of the pattern observed after a polarizer. This manifests as a rotation of the two lobes. In figure 4.8, we show a simulation where we see the rotation induced by an azimuthally polarized Bessel probe that interacts with a cylindrical plasma obtained by a 26° Bessel pump beam, where (a) without and (b) with the plasma. We filter the horizontal component using an analyzer, its axis is fixed at 0 ° in figure 4.8 (a) and (b). The result in figure 4.8 provides both information amplitude (absorption) and phase (rotation).

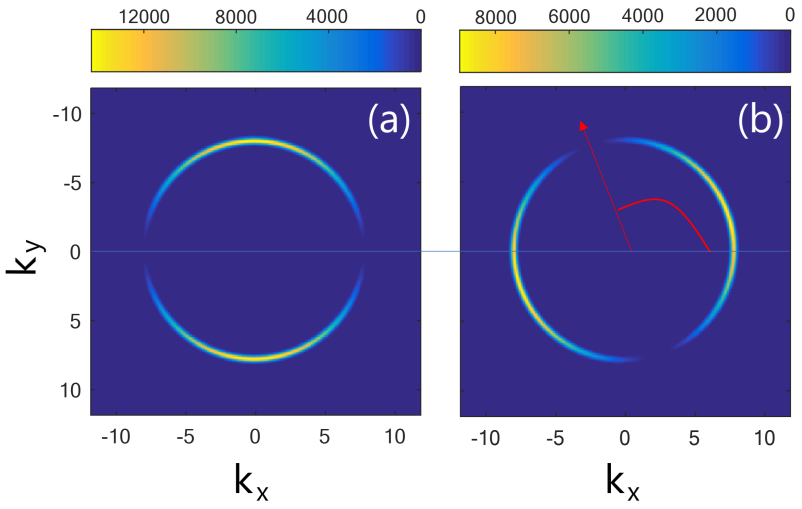


Figure 4.8: The far-field rotation concept. (numerical simulation)

Thus, for several Bessel beams $(m, \theta)$ interacting with the plasma, we can build a numerical map of absorption and phase change as a function of the Bessel's angle and order using a fixed plasma profile, i.e. fixed pump-probe delay and fixed energy, as shown in figure 4.9.

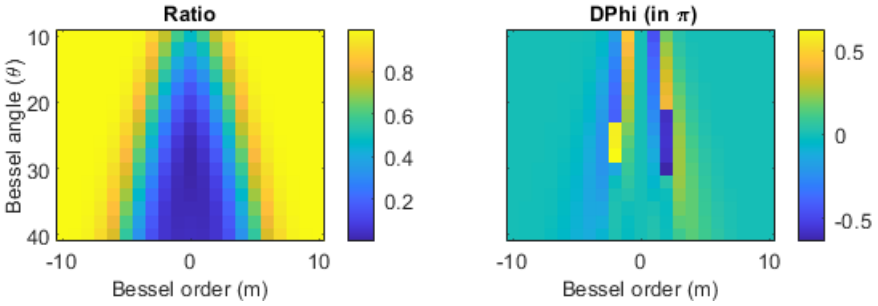


Figure 4.9: Absorption (left) and rotation (right) numerical map due to the interaction of a symmetrically polarized Bessel probe beam $(m, \theta)$ with a cylindrical rod plasma with waist of 300 nm and collision time $\tau_c$=200 fs.

Figure 4.10 shows the overlapping regions between a cylindrical plasma obtained by a 26° Bessel pump beam and Bessel probe beams $(m, \theta)$. The Bessel order $m$ varies to $0$, $3$, $and\, 6$ in the vertical direction from left, respectively. At the same time, the Bessel angle $\theta$ varies at $13°$, $22°$, $and\, 31°$ on the horizontal axis. As we can see, for the same Bessel order, increasing the Bessel angle increases the area probe volume interacting with the plasma. In contrast, the overlapping volume is reversely proportional with the Bessel order (with the same incident Bessel angle).

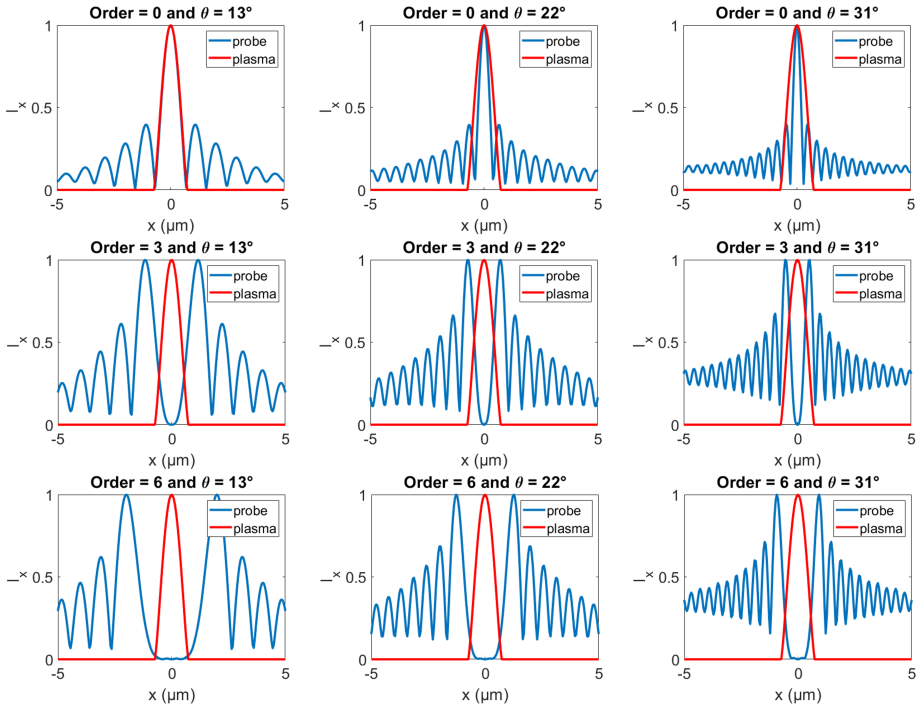


Figure 4.10: The overlapping between a cylindrical plasma obtained by a 26° Bessel pump beam and Bessel probe beams $(m, \theta)$.

Our strategy to retrieve the plasma parameters (density profile and collision time) is to compare the experimental "signature", corresponding to the reflectivity of the plasma for a series of illumination conditions, to a "database" using a machine learning approach provided by University of Lyon (S. Chretien) in a collaboration to predict the experimental plasma parameters by matching the experimental maps with the numerical ones. The database is made by computing the reflectivity maps for the same series of illumination conditions.

To understand the dynamics of laser-matter interactions, we can change the pump parameters and repeat the retrieval algorithm for each delay.

### 4.2.2/ EXPERIMENTAL SETUP OVERVIEW

In our experimental setup, the pump beam shaping is almost the same as the setup presented in chapter 3, figure 3.8. The final experimental setup (presented after in subsection 4.3.5) is different than the initial setup in figure 4.11 due to the challenges we faced during the work (explained in detail in the following section). Therefore, we assume, for now, that the probe setup is identical to the pump. Only we insert a nonlinear crystal at the beginning to generate the probe 400nm beam. We target measuring the absorption and the rotation of the entire Bessel beam. Thus, both measurements are obtained from the far-field configuration, as shown in figure 3.8(b). Figure 4.11 shows the experimental setup concept for the two Bessel pump-probe beams imaging. The red colour represents the $\omega$ pump arm, i.e. 800nm wavelength beam, while the violet arm is the $2\omega$ probe beam, i.e. 400nm wavelength beam. We generate the $2\omega$ beam using a 50 $\mu$m-thick nonlinear BBO crystal to create the probe pulse. The low thickness of the BBO crystal ensures the full conversion of the input spectrum to ensure a short pulse duration of the probe. Then, we shape the beams into Bessel beams using two different SLM models, according to the working wavelength of each.

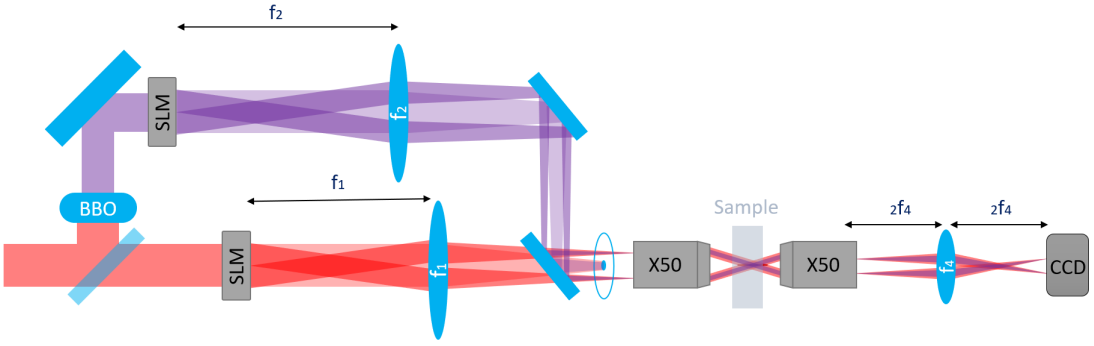


Figure 4.11: The initial experimental setup for two Bessel pump and Bessel probe beams imaging.

## 4.3/ CHALLENGES

The numerical model is based on two assumptions: the generated plasma has a cylindrical profile (for that, simply, we use a quarter wave plate (QWP) to change the pump

polarization into circular polarization), and the probe Bessel beam is either radially or azimuthally polarized. Moreover, the basic pump-probe setup consists of two beams having different parameters, such as wavelength and optical path. Therefore, the pump-probe experiments are usually arduous due to obstacles encountered. This section presents the challenges we faced during the experimental work and how we overcame them, as follows:

1. Probe pulse polarization.
2. Control of the pump-probe delay.
3. Probe pulse compression.
4. Overlap pump and probe in space.

### 4.3.1/ PROBE PULSE POLARIZATION

As we have seen in the concept section, the polarization of the Bessel probe beam has to be radial or azimuthal polarization. Therefore, we used a commercial radial polarization converter (RPC) by ARCoptix.

**Principle of the RPC:** The RPC is made of two parts of a liquid crystal with a symmetric axis. It rotates the incident linearly polarized beam direction by a twist angle [Stalder and Schadt, 1996]. As shown in figure 4.12, the two parts have a different sense of rotation. While on the top half, the rotation is clockwise, the lower part is characterized by counterclockwise rotation. In this case, see figure 4.12, a defect line running along the diameter parallel to the cell axis arises.

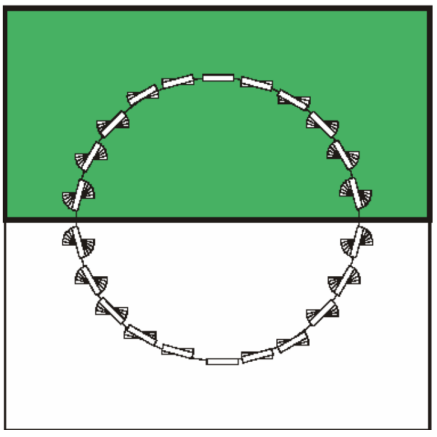

Figure 4.12: Liquid crystal alignment in the polarization converter for a stable configuration. The line in the center represents a defect line present because of the different twisted senses of the upper and lower part. The arrow represents the entrance polarization. Figure from [Stalder and Schadt, 1996]

RPC converts the linear polarized light into radial or azimuthal polarization according to the entrance polarization direction to the cell axis [Stalder and Schadt, 1996]. If the

incident beam polarization direction is parallel to the cell axis, it results in an azimuthal polarization. On the contrary, the radial polarization is doable using an incident beam linearly polarized and the polarization direction perpendicular to the cell axis, as shown in figure 4.13.

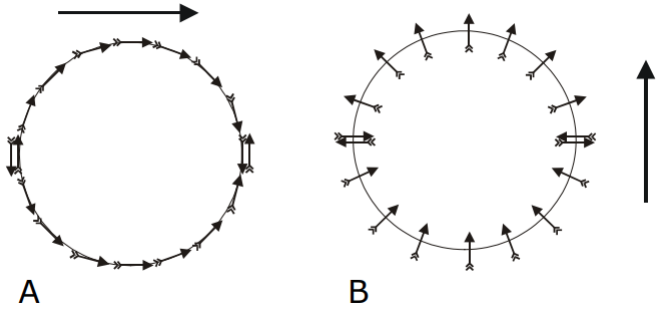


Figure 4.13: Production of azimuthally and radially polarizations. The big arrows represent the entrance polarization. A) Azimuthally polarized light is achieved for light incidents parallel to the cell axis. B) Radially polarized light is achieved for light incident perpendicular to the cell axis. Figure from RPC user manual, ARCoptix.

Importantly, because of the singularity of the polarization at the center of the cell, a dark spot appears when the RPC is illuminated with a flat intensity distribution.

**Insertion of the RPC:** To avoid the singularity of the RPC, we decided to place the RPC close to one of the Fourier planes of the probe beam, where the higher-order Bessel beam appears as an annulus. Nevertheless, the configuration for shaping the probe beam into a Bessel beam in figure 4.11 is not doable for two reasons; first, the far-field plane where to insert RPC is at the back-focal plane of the microscope objective (ideally $f_b = -8mm$, i.e. inside the microscope objective's package). Second, in the presented configuration, the far-field plane is the focal plane of the entire field on the SLM. Thus, we will have a high risk of exceeding the RPC's damage threshold and damaging it.

Therefore, we used another way to shape the probe into Bessel, as explained in chapter 1, figure 1.16 (b). In this configuration, the reflected modulated part of the beam is only the ring presented on the SLM, and then we use a 1:1 imager, as in chapter 2 figure 2.12, to repeat the SLM plane where to place the RPC, as shown in figure 4.22.

### 4.3.2/ CONTROL OF THE PUMP-PROBE DELAY

Good management of the relative pump-probe delay guarantees the fidelity and temporal accuracy of the measurement. In an optical experiment, the control of the relative pump-probe delay is simple, even for delays of the order of ten femtoseconds: a simple delay line, consisting of two pairs of mirrors and a micrometric translation plate, can perform this function (figure 4.14). However, determining the delay in an absolute way is more delicate because it gives the coincidence of pump and probe pulses within the sample is challenging.

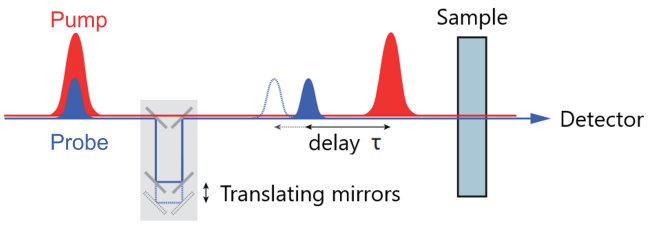


Figure 4.14: Illustration of adding a variable delay between the pump and probe pulses by moving a pair of mirrors. Figure from [Meyer, 2020].

In 2021, our group proposed a highly-sensitive in-situ diagnostic technique for probe pulses [Xie et al., 2021]. As shown in figure 4.15 (a), the concept is to induce a transient index grating by the Kerr effect on which the probe beam diffracts when the pump and probe are temporally coincident. The Kerr-index grating does not impose any polarization condition between the pump and probe pulses, allowing it to work in an isotropic medium and without imposing any condition on the energy of the probe pulse. Figure 4.15 (b) shows a typical diffracted signal intensity, which is a cross-correlation between pump and probe pulses collected on the camera.

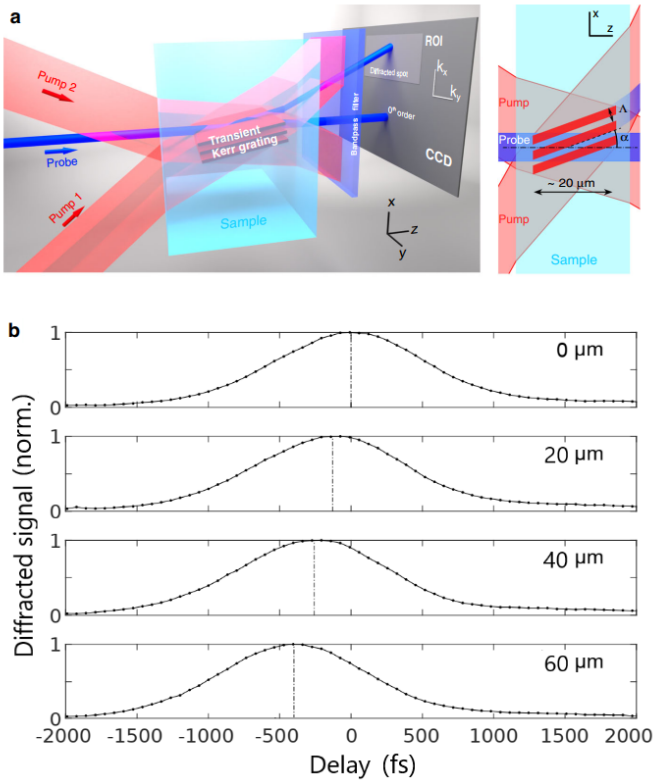


Figure 4.15: Transient grating technique. **a** Concept of the transient grating induced by the shaped infrared pump pulse in a transparent dielectric [Xie et al., 2021]. **b** Study of the pump-probe synchronization for different translating stage positions of 0, 20, 50, and 60 $\mu$m. This series of curves shows the importance of the positioning of the sample relative to the beam, to determine the zero delay. Experimentally, we perform this nondestructive measurement at the sample position that will be used further.

This signal allows us to evaluate the pump-probe delay within the sample, precisely at the position where further measurements will be made. Importantly, this measurement is non-destructive. Therefore, it can be repeated as many times as required before running the pump-probe experiment.

### 4.3.3/ PROBE PULSE COMPRESSION

The diffracted signal in the transient grating experiment is a cross-correlation: therefore, it carries information on the temporal profiles $I_{probe}(t)$ and $I_{pump}(t)$. We can evaluate one of the pulse durations assuming the other is known.

This technique allowed us to evaluate that the microscope objective is highly dispersive (the probe pulse duration is stretched from 50 to 700 fs). Therefore, we pre-compensate the second-order dispersion due to the microscope objective using a 4 prism compressor system, as shown in figure 4.16. The insertion depth of the prisms is evaluated using the transient grating signal.

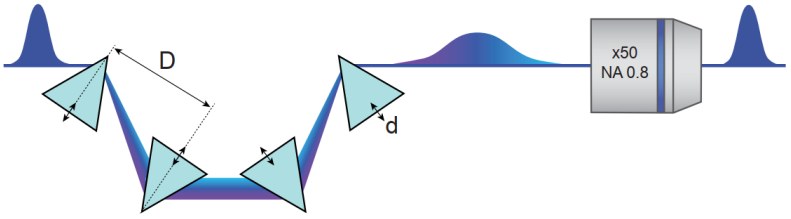


Figure 4.16: Four prisms compressor system to compensate the microscope objective's dispersion. In reality, the compressor is folded using a mirror to exploit the symmetry of the system. Figure from [Meyer, 2020].

### 4.3.4/ OVERLAPPING PUMP-PROBE BESSEL BEAMS IN SPACE

In principle, we generate a cylindrical plasma rod with a diameter of typically 200 nm (see the previous chapter) using a Bessel pump beam, and then we probe it using other Bessel beams. Thus, we aim to overlap all Bessel beams in two directions; in the XY-plane, which targets matching the Bessel cores' centre. In addition, we aim at probing the same region of the plasma rod in the z-direction with a precision of typically 5 $\mu$m, which corresponds to the typical scale at which the Bessel beam generated plasma can be considered uniform. Therefore, the overlapping accuracy needed for this experiment is exceptionally high.

#### 4.3.4.1/ SUPERPOSITION IN THE TRANSVERSE PLANE

The precision of matching the Bessel beams centre is crucial in our work. The mismatch does not affect the absorption maps in a few microns precision, but the main problem is seen in the rotation ones due to the phase change becoming unsymmetric around the Bessel annulus. The $\approx$ 60 nm matching precision required is manually impossible with the optical alignment.

Therefore, after matching the pump-probe zero-order Bessel centres by fine alignment and setting the delay between the two arms to zero, we shoot a dielectric sample with a high-power pump pulse to induce absorption in the Bessel probe core. The occurred absorption, as expected, is not usually centered within the probe core. We optimize the matching by shifting the SLM phase mask to obtain a doughnut shape in the Bessel profile centre. A single-pixel sensitivity is observed.

#### 4.3.4.2/ SUPERPOSITION IN THE LONGITUDINAL DIRECTION

In our work, we target probing the same region of the plasma (i.e. the same part of the Bessel pump beam longitudinal profile) within ± 5 $\mu$m. In the setups used since the beginning of the thesis, we were using only the 800 nm beam. Thus, chromatic aberration was a negligible factor. On the contrary, here, we use two beams with different wavelengths of 400 and 800 nm central wavelengths. Therefore, we simulated the experimental setup to quantify the chromatic aberration we have in the setup by studying the path of the optical rays using ZEMAX OpticStudio. Two factors of interest affect the overlap between the beams in the longitudinal direction: the observation with our imaging system and the insertion of the dielectric sample.

**Imaging system:** We studied our imaging system's chromatism. The imaging system is a magnifying telescope consisting of a microscope objective ×50 and a lens with a focal distance of 400 or 200 mm for near-field and far-field imaging, respectively. Using Zemax, as shown in figure 4.17, we found the microscope objective's chromatic aberration leads to a longitudinal shift of about 2 $\mu$m. This value is below the constraint of 5 micrometres.

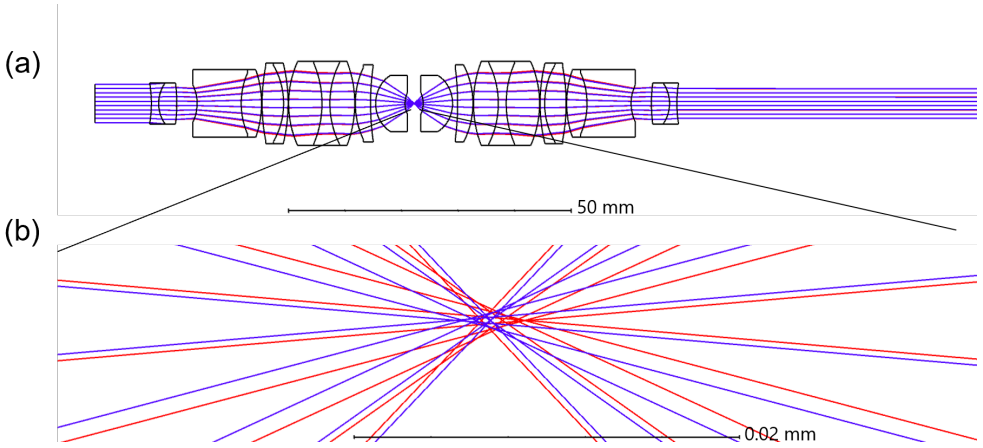


Figure 4.17: The chromatic aberration by microscope objective ×50. (a) Two plane waves focused by the microscope objective and collected again using another flipped identical microscope objective (b) Zooming in the focusing zone in (a). The 800 nm beam is represented in red, while the blue is for the 400nm beam.

We performed a similar evaluation with the conventional focusing 400 mm lens and obtained, due to the chromatism, a focal position shift between 800 and 400 nm beams of 11.2 mm at the camera plane, which is a huge aberration for our experiment. Therefore, we exchanged the imaging lenses for near-field and far-field with achromatic doublet

ones with the same focal lengths of 400 mm and 200 mm, respectively, and obtained focal position shift less than the simulation resolution of Zemax, i.e.<20 $\mu$m at the camera plane.

**Dielectric sample:** We simulated the case where the two Bessel beams overlap in a vacuum, and the dielectric sample is inserted. Besides the chromatic aberration due to the dielectric, the most important issue is related to a different longitudinal focal position for the different Bessel probe angles.

Figure 4.18 presents the propagation of the pump (red) and probe (blue) Bessel beams with $\theta = 26^\circ$ and $13^\circ$, respectively. As we see in figure 4.18 (a), at the microscope objective's focal plane, the centre of the probe beam overlaps the pump onset. This is because of the different configurations of shaping the beam into a Bessel beam, i.e. direct space for the pump and Fourier space for the probe. However, we observe from figure 4.18 that inserting a Sapphire sample with 150 $\mu$m thickness shifts the Bessel pump beam 90 $\mu$m more than the $13^\circ$ probe Bessel, as shown in figure 4.18 (b).

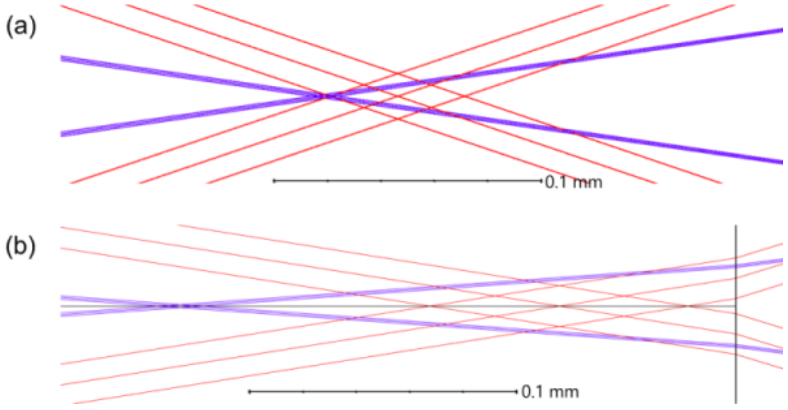


Figure 4.18: The chromatic aberration by a 150 $\mu$m thick Sapphire sample on pump-probe Bessel beams propagate inside the sample. (a) without the sample, the probe focused at the beginning of the Bessel pump. (b) with the sample, we observe that the probe is focused 90 $\mu$m before the beginning of the Bessel pump beam. Three rays present the beam to show the beginning, middle, and end of the Bessel beam.

Furthermore, depending on the probe incident angle $\theta$, we observe different displacements $\Delta$d of the Bessel probe beams by inserting the sapphire sample. In figure 4.19, we propagate three probes with incident angles $\theta$ covering our work plan of $13^\circ$, $22^\circ$, and $31^\circ$. In the sample absence case, as shown in figure 4.19 (a), the three probes are almost centred at the same point with $\Delta$d less than 2 $\mu$m. While in figure 4.19 (b), inserting the sample induces $\Delta$d 11 $\mu$m from the $13^\circ$ beam to the $22^\circ$ beam and 30 $\mu$m for the $13^\circ$ beam to the $31^\circ$ beam.

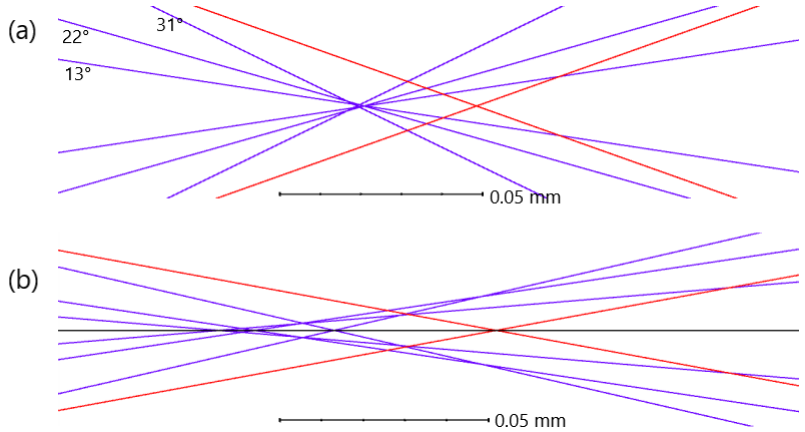


Figure 4.19: The probe displacement according to the incident angle $\theta$. (a) without the sample. (b) with the sample. The beams are represented by only the central ray to simplify the figure.

The different angles are focused at different longitudinal positions because of the presence of the interface in the propagation. As we can see in figure 4.20, the refraction of the different beams modifies the longitudinal position at which they cross the optical axis. Moreover, the sample's position with respect to the beam changes the focal depth differently for each incident angle.

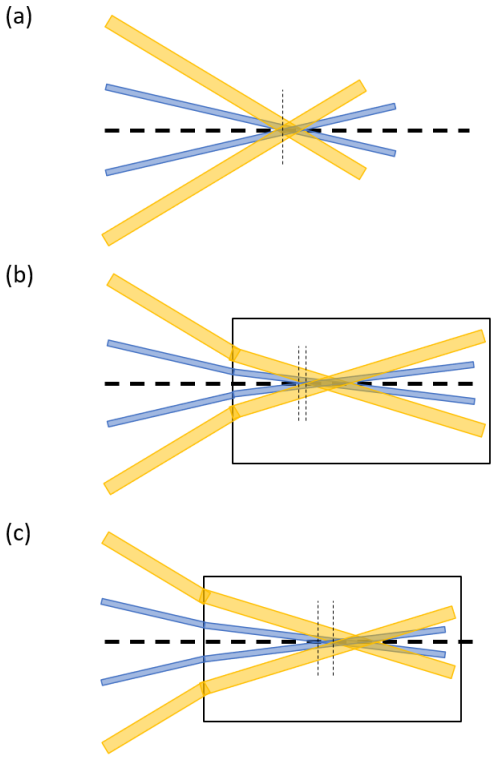


Figure 4.20: The effect of the sample insertion on the focal longitudinal position for different incident angles $\theta$. (a) without the sample. (b-c) with the sample and at the different sample positions. The beams are represented with typical incident angles of 13° (blue) and 31° (orange) and the refracted angles are calculated from Snell's law taking into consideration a sapphire sample. The dashed line represents the onset of the Bessel beams.

To circumvent this problem, we added a defocus term in the simulations at the SLM plane to control the probe's longitudinal position. Figure 4.21 shows that we optimized the defocus values to probe the pump's centre for the cone angles 13°, 22°, and 31°. Unfortunately, we can not fix absolute defocus values for the experiment because they depend on the sample thickness and its related position to the beams.

We use the same approach to superimpose the pump to the crossing of all probe beams. Experimentally, we have optimized the values of the defocus to maximize the absorption of each probe beam.

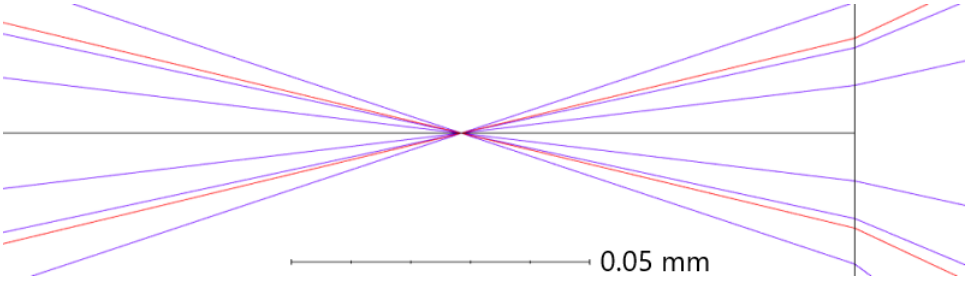


Figure 4.21: Probing the pump's centre using $\theta$ of 13°, 22°, and 31°.

### 4.3.5/ FINAL EXPERIMENTAL SETUP

In the experiment, we use the same Ti-Sapphire laser source with central wavelength ~ 800nm. Using a beam splitter, we propagate the beam in two paths, pump and probe. Figure 4.22 presents a scheme of the actual experimental setup after solving the different challenges. We shape the beams differently into Bessel beams using two SLMs. For the probe pulse, all the intensity that is rejected is sent to the first order and is blocked in the Fourier space. For the pump beam, in contrast, it is the first order of diffraction which carries the information of the beam shape. However, in contrast with the previous approach [Froehly et al., 2014], we do not use an additional linear phase ramp to separate the different orders of diffraction since this was inducing a small cylindrical asymmetry due to the difference in diffraction efficiency. For this case, the filtering is performed using a mirror blocking the zeroth order at the centre of the Bessel ring just before the microscope objective. Therefore, the pump is shaped as usual (in the previous chapters) in the direct space with a conical phase mask. On the other hand, we use a ring phase mask to shape the probe into a Bessel beam to insert the RPC in the far-field plane while minimizing the risk of damaging it. Moreover, we inserted a prism compressor and an optical delay line in the probe path to control its pulse duration and pump-probe delay, respectively.

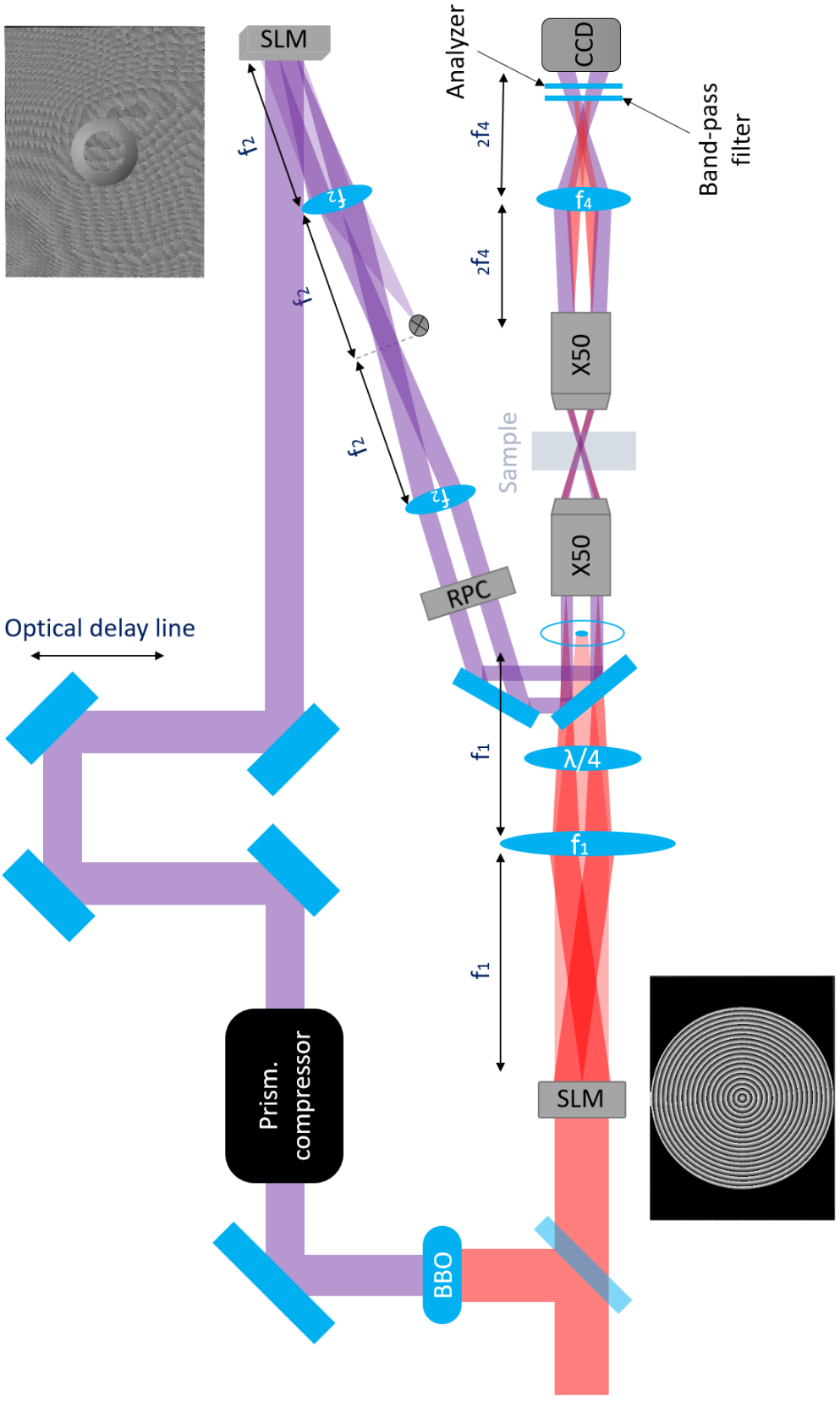


Figure 4.22: A scheme of the pump-probe setup. The pump is presented in red while the probe is in violet. In the probe path, a BBO-crystal, a prisms compressor to control, a delay line consisting of pair of 90° mirrors, SLM with an annulus phase mask, a 1:1 telescope, and a radial polarization converter RPC. On the other hand, the pump beam is shaped by SLM with a conical phase mask and circularly polarized using a quarter wave plate.

## 4.4/ ACHIEVEMENTS

At the time of the thesis writing, we managed to build the setup in figure 4.22. We obtained a high-quality Bessel probe beam covering a reasonable range of Bessel angles and orders. Moreover, we acquired several absorption maps as a function of the pump pulse energy and pump-probe delay. Unfortunately, we faced some problems with the laser source stability. The needed alignment was valid for less than half an hour, which makes it challenging to get trusted rotation maps for which more than 100 different configurations are needed. Ongoing and future work will solve the stability of the pointing.

### 4.4.1/ HIGH-QUALITY PROBE BEAM

Initially, we switch off the SLM to keep the Gaussian beam for the pulse duration measurements. Using the transient grating technique, we compress the probe pulse duration to $\sim$ 130 fs and set the pump-probe delay in the fs range. After, we turn on the SLM for the Bessel beam shaping. To get comparable data by changing the Bessel angles, we ensure that the Bessel beam length is maintained constant by adjusting the width of the Fourier annulus on the SLM mask. For the Bessel order, we add to the phase mask a vortex phase $e^{im\theta}$ where m is the Bessel order. Figure 4.23 presents the Bessel probe beam centre on the CCD camera. As shown in figure 4.23, we obtained excellent Bessel probe beams profile for Bessel angles 13°, 18°, 23°, 28°, and 31° on the vertical axis from top to down, respectively, and Bessel orders of 0, 5, 10, and 15 on the horizontal axis.

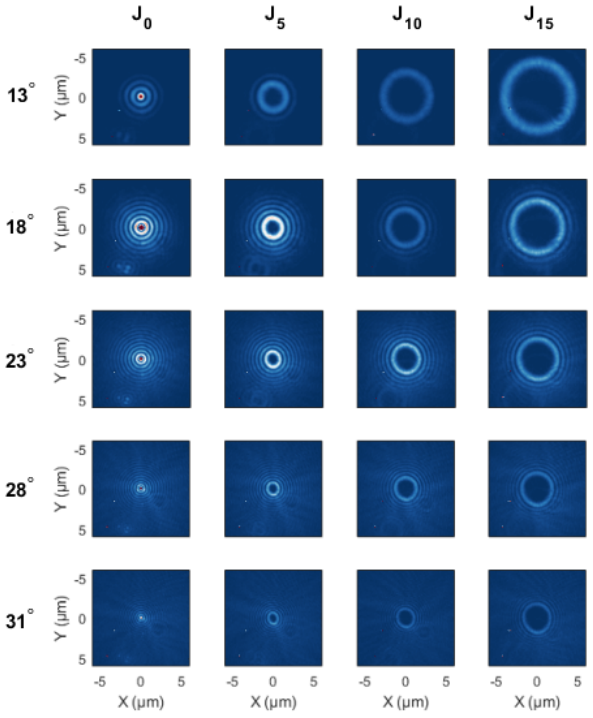


Figure 4.23: Experimental images of Bessel probe beam center (m,$\theta$) for Bessel orders **m =** 0, 5, 10, and 15 and Bessel angle $\theta$ **=** 13°, 18°, 23°, and 31°. Special care for the alignment has been performed to ensure the high degree of cylindrical symmetry of the different probe beams.

### 4.4.2/ ABSORPTION MAPS

We built 2D absorption maps for different Bessel pump beam parameters as shown in figure 4.25. For one map, we used a fixed pump parameter and delay 105 Bessel probe beams as a [21×5] matrix representing the different Bessel probe beams with one order step for $J_m$ with m = -10:10 and $\theta$ of $\theta$ = 13°, 17°, 22°, 27°, and 31°. To measure the absorption, we shoot the Bessel probe pulse twice for each matrix cell, with and without the pump pulse, as data and reference, respectively. An example of the results is shown in figure 4.24: in the Fourier space, the different Bessel beam orders have the same annulus shape, and that is preserved even after the interaction with the plasma. This shows that the scattering is reasonably small.

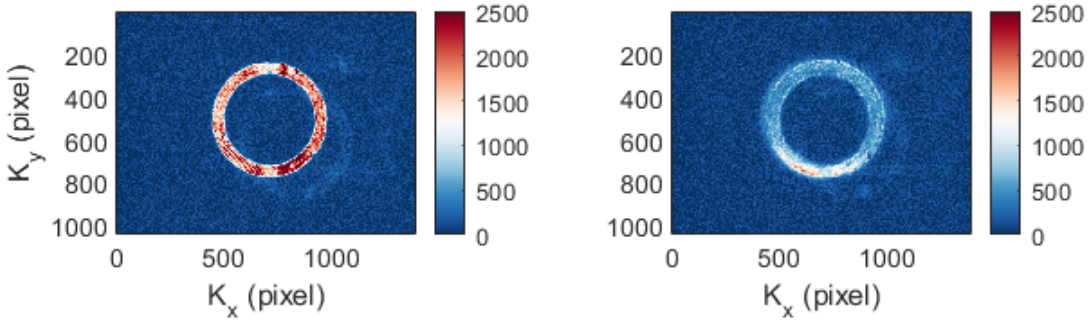


Figure 4.24: Experimental images of a Bessel probe beam, in the Fourier space, to calculate the occurred absorption. The left sub-figure is with the absence of the pump, i.e. without plasma, and is saved as a reference (ref.), while on the right the data acquired after the interaction with the plasma.

Then, we calculate the absorption as the complement of the ratio between the data and the reference, i.e. $Abs = 1 - (data/ref.)$. Importantly, between each measurement, the sample is translated in X-direction by a distance of 20 $\mu$m, to ensure that the pump pulse is always illuminating a fresh area of the sample. This imposes that the flatness of the sample must be controlled to ensure that the position of the beam inside the sample is always the same.

In the set of maps in figure 4.25, we studied the effect of the Bessel pump beam energy on the Bessel probe beam absorption and fixed the rest of the pump parameters. We used pump energies of 0.5, 1, 2, and 3 $\mu$J and a pump-probe delay of 300 fs. As we can see, we obtained a high absorption of the probe pulses that occurs for energies above 2 $\mu$J. In the case of pump energy 3 $\mu$J, the absorption can reach up to 60% for the zeroth-order Bessel probe with a cone angle of 22°. As expected from figure 4.10, the highest overlap is for the Bessel orders that are close to zero, hence the absorption is the highest for those orders. Moreover, we see that between 2 and 3 $\mu$J, the plasma diameter increases because the affected probe orders are increasing.

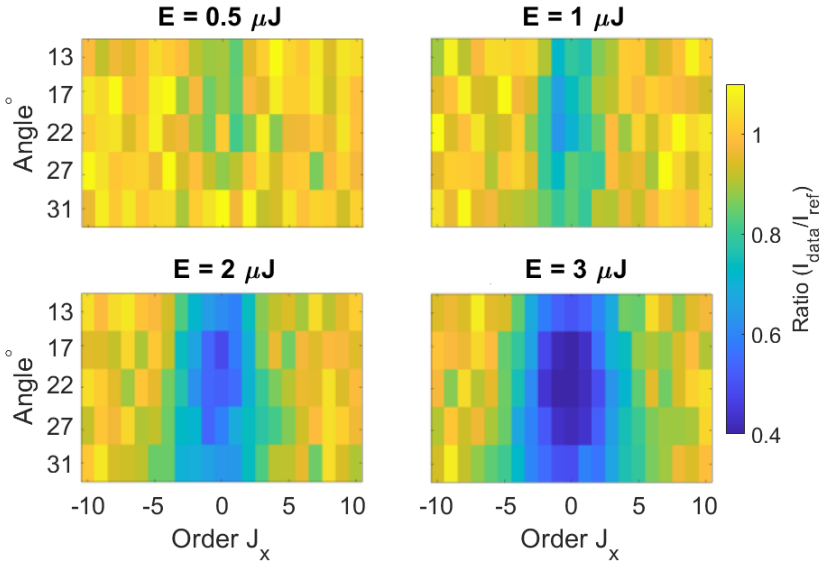


Figure 4.25: The absorption maps of 130 fs probe pulse obtained within sapphire by changing the 120 fs pump pulse energies to 0.5, 1, 2, and 3 $\mu$J and a pump-probe delay of 300 fs.

In figure 4.26, we acquired another set of absorption maps by fixing the pump energy at 2 $\mu$J (corresponds typically to the threshold for nanochannel formation inside sapphire) and varied the pump-probe delay to 100 fs, 300 fs, 700 fs, 1 ps, and 10 ps. The figure shows, apparently, the dynamics of generating plasma still going after the pump pulse. With time, the plasma density increases leading to higher absorption. This can be expected from the avalanche phenomenon which cools down the highly excited electron gas by multiplying the number of electrons.

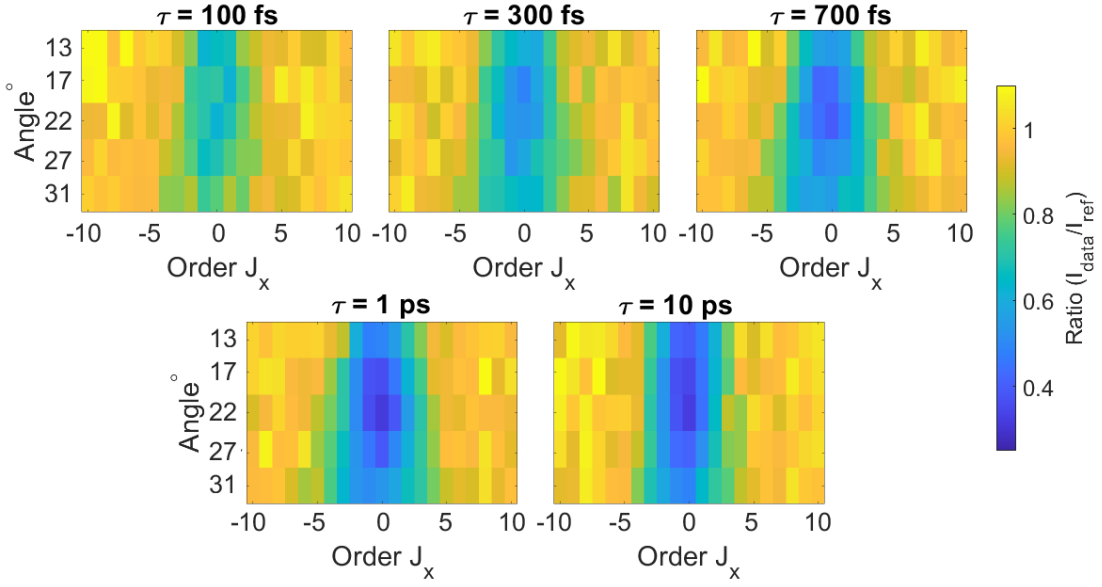


Figure 4.26: The absorption maps of 130 fs probe pulse obtained by changing the pump-probe delay ($\tau$) to 100 fs, 300 fs, 700 fs, 1 ps, and 10 ps and the 120 fs pump pulse energy is 2 $\mu$J.

## 4.5/ CONCLUSION

After confirming the generation of overcritical plasma with a diameter of 200 nm, we designed and built a pump-probe imaging system to retrieve the generated plasma parameters. We presented a novel pump-probe technique in which both beams are shaped into Bessel beams to improve the sensitivity of the pump-probe imaging. We show the ability to control the overlapping between the pump and the probe beams by changing the Bessel probe beam order and angle.

We managed to overcome the obstacles we faced during the experimental work. First, we fulfil the numerical model provided by Remo Giust that solves Maxwell's equation and calculates the absorption and phase change that occur to radially or azimuthally polarized Bessel probe beam interacts with a cylindrical plasma profile. Using the transient grating technique, we controlled the pump-probe delay and optimized the probe pulse duration using a two-prisms compressor. Moreover, we precisely overlapped in space both pump and probe; in XY-plane by shifting the pump SLM phase mask and in the z-direction by adding a defocus term to the probe phase mask. As proof of principle, we acquired several absorption maps for different pump energies and pump-probe delays after obtaining high-quality Bessel probe beams. This technique will be soon fully implemented using both absorption and rotation information.

# CONCLUSION AND PERSPECTIVES

This thesis work focused on the study of femtosecond laser-matter interaction in dielectrics, particularly for spatially shaped pulses as Bessel beams. After introducing, in Chapter 1, the challenges in the measurement and modelling of the interaction of zeroth-order Bessel beam with matter, we studied, in chapter 2, the effect of the Bessel beam polarization on the laser-structuring process. Besides, in the third and forth chapters, we concentrate on the laser-generated plasma, which is responsible for transferring the energy into the medium in laser processing for a given interaction medium. For this purpose, we studied the laser-plasma interactions to evaluate the plasma parameters with two different approaches.

In chapter 2, we designed, implemented and operated a polarization-shaped Bessel beam technique whose final objective is to provide a new technique to inscribe optical elements within glass via laser writing of nanogratings. We controlled the Bessel beam core polarization along its propagation axis. We obtained linear polarization continuously rotates from zero to 180 degrees along beam length exceeding 60 $\mu$m. Using such a polarized-shaped beam, we can induce a permanent rotating modification of silica. As proof of principle, we processed a structure where strong circular rotation was observed with minimal birefringence. This paves the way to the writing of complex optical elements that cannot be easily produced using conventional material deposition and lithography techniques.

We confirmed in chapter 3 the generation of overcritical plasma with a typical transverse scale of 200 nm within the bulk of sapphire by a single ultrafast Bessel pulse. Our strategy was based on comparing different diagnostics to evaluate numerically what could be the plasma profile, but the key aspect of wave turning was expected and could not be observed experimentally. We showed numerically and experimentally that the incompatibility between the profiles was technical due to the sample and imaging system need high-accuracy positoning in the hundred nanometer scale. We observed Bessel beam lobes shifting in the single Bessel pulse with energies in the channel formation threshold level, which is in agreement with the numerical prediction of the wave-turning phenomenon. Moreover, we verified the occurred resonance absorption by studying the detected second harmonic emission signal from the sapphire. Our findings open a new route to generating high energy density matter inside solids and the control of the energy deposition by ultrafast pulses within the bulk of solids, which is particularly crucial in the laser micro-/nano- structuring of materials. Our results, therefore, provide new avenues for generating new material phases, for investigating the transformations of transparent dielectrics and semiconductors, for nonlinear photonics, and our configuration can be considered a convenient new platform for exploring warm dense matter physics.

In the last chapter, we proposed a new pump-probe technique that allows retrieving the transverse plasma density distribution with temporal resolution. This is performed via measuring the reflectivity of a series of probe pulses, shaped as higher order Bessel beams with different incidence angles. Therefore, we shaped both pump and probe beams into Bessel to improve the sensitivity of the pump-probe imaging by controlling the overlap between pump-induced cylindrical plasma and probe beams with different order and angle. We constructed phase change and absorption maps experimentally and numerically. The numerical ones are obtained using the model based on solving Maxwell's equations for a plasma profile interacting with the Bessel probe pulse. During the experimental work, we faced several challenges, such as changing the polarization of the probe pulse into radial or azimuthal, and the precise overlap between the two beams in space. Hitherto, as proof of principle, we acquired several absorption maps for different pump energies and pump-probe delays after obtaining high-quality Bessel probes.

At the end of this thesis, several lines of work are open for us. Our polarization-shaped Bessel beam experiment has shown encouraging first results. This work will be continued this adapting the parameters of the writing Bessel beam to maximize optical thickness and maximize chiral properties. Our new technique for the measurement of the plasma density profile has shown that it has a capability of being very accurate but is very sensitive to beam pointing stability, particularly or the measurement of the phase of the reflection coefficients. This work will be continued in the future and will be an enabling platform to study laser-plasma interaction dynamics in a wide range of parameters, materials, and temporal scales.

# BIBLIOGRAPHY


**[Amako et al., 2003]** Amako, J., Sawaki, D., and Fujii, E. (2003). Microstructuring transparent materials by use of nondiffracting ultrashort pulse beams generated by diffractive optics. *Journal of the Optical Society of America B*, 20(12):2562.

**[Arber et al., 2015]** Arber, T. D., Bennett, K., Brady, C. S., Lawrence-Douglas, A., Ramsay, M. G., Sircombe, N. J., Gillies, P., Evans, R. G., Schmitz, H., Bell, A. R., and Ridgers, C. P. (2015). Contemporary particle-in-cell approach to laser-plasma modelling. *Plasma Physics and Controlled Fusion*, 57(11):113001.

**[Ardaneh et al., 2022a]** Ardaneh, K., Meyer, R., ***Hassan, M.***, Giust, R., Morel, B., Couairon, A., Bonnaud, G., and Courvoisier, F. (2022a). Femtosecond laser-induced subwavelength plasma inside dielectrics: I. field enhancement. *Physics of Plasmas*, 29(7):072715.

**[Ardaneh et al., 2021]** Ardaneh, K., Meyer, R., ***Hassan, M.***, Giust, R., Xie, C., Morel, B., Ouadghiri-Idrissi, I., Furfaro, L., Froehly, L., Couairon, A., Bonnaud, G., and Courvoisier, F. (2021). A new route to high energy density inside the bulk of transparent materials. *arXiv*, page 2109.00803.

**[Ardaneh et al., 2022b]** Ardaneh, K., ***Hassan, M.***, Morel, B., Meyer, R., Giust, R., Couairon, A., Bonnaud, G., and Courvoisier, F. (2022b). Femtosecond laser-induced subwavelength plasma inside dielectrics. ii. second-harmonic generation. *Physics of Plasmas*, 29(7):072716.

**[Bärsch et al., 2003]** Bärsch, N., Körber, K., Ostendorf, A., and Tönshoff, K. (2003). Ablation and cutting of planar silicon devices using femtosecond laser pulses. *Applied Physics A*, 77(2):237–242.

**[Beresna et al., 2011]** Beresna, M., Gecevičius, M., Kazansky, P. G., and Gertus, T. (2011). Radially polarized optical vortex converter created by femtosecond laser nanostructuring of glass. *Applied Physics Letters*, 98(20):201101.

**[Beresna et al., 2013]** Beresna, M., Gecevičius, M., Lancry, M., Poumellec, B., and Kazansky, P. (2013). Broadband anisotropy of femtosecond laser induced nanogratings in fused silica. *Applied Physics Letters*, 103(13):131903.

**[Bergner et al., 2018]** Bergner, K., Seyfarth, B., Lammers, K. A., Ullsperger, T., Döring, S., Heinrich, M., Kumkar, M., Flamm, D., Tünnermann, A., and Nolte, S. (2018). Spatiotemporal analysis of glass volume processing using ultrashort laser pulses. *Applied Optics*, 57:4618.

**[Bhuyan et al., 2010]** Bhuyan, M. K., Courvoisier, F., Lacourt, P. A., Jacquot, M., Salut, R., Furfaro, L., and Dudley, J. M. (2010). High aspect ratio nanochannel machining using single shot femtosecond Bessel beams. *Applied Physics Letters*, 97(8):081102.

**[Bhuyan et al., 2015]** Bhuyan, M. K., Jedrkiewicz, O., Sabonis, V., Mikutis, M., Recchia, S., Aprea, A., Bollani, M., and Trapani, P. D. (2015). High-speed laser-assisted cutting of strong transparent materials using picosecond Bessel beams. *Applied Physics A: Materials Science and Processing*, 120:443–446.

**[Bhuyan et al., 2017]** Bhuyan, M. K., Velpula, P. K., Somayaji, M., Colombier, J. P., and Stoian, R. (2017). 3D nano-fabrication using controlled Bessel-glass interaction in ultra-fast modes. *Journal of Laser Micro Nanoengineering*, 12:274–280.

**[Bitman et al., 2012]** Bitman, A., Moshe, I., and Zalevsky, Z. (2012). Improving depth-of field in broadband THz beams using nondiffractive bessel beams. *Optics Letters*, 37(19):4164.

**[Boucher et al., 2018]** Boucher, P., Hoyo, J. D., Billet, C., Pinel, O., Labroille, G., and Courvoisier, F. (2018). Generation of high conical angle Bessel–Gauss beams with reflective axicons. *Applied Optics*, 57(23):6725.

**[Braun et al., 1995]** Braun, A., Korn, G., Liu, X., Du, D., Squier, J., and Mourou, G. (1995). Self-channeling of high-peak-power femtosecond laser pulses in air. *Optics Letters*, 20(1):73.

**[Bricchi et al., 2002]** Bricchi, E., Mills, J. D., Kazansky, P. G., Klappauf, B. G., and Baumberg, J. J. (2002). Birefringent fresnel zone plates in silica fabricated by femtosecond laser machining. *Optics letters*, 27(24):2200–2202.

**[Bulgakova et al., 2013]** Bulgakova, N. M., Zhukov, V. P., and Meshcheryakov, Y. P. (2013). Theoretical treatments of ultrashort pulse laser processing of transparent materials: toward understanding the volume nanograting formation and “quill” writing effect. *Applied Physics B*, 113(3):437–449.

**[Cao et al., 2019]** Cao, J., Lancry, M., Brisset, F., Mazerolles, L., Saint-Martin, R., and Poumellec, B. (2019). Femtosecond laser-induced crystallization in glasses: growth dynamics for orientable nanostructure and nanocrystallization. *Crystal Growth & Design*, 19(4):2189–2205.

**[Cardona and Peter, 2005]** Cardona, M. and Peter, Y. Y. (2005). *Fundamentals of semiconductors*, volume 619. Springer.

**[Chattrapiban et al., 2003]** Chattrapiban, N., Rogers, E. A., Cofield, D., Wendell T. Hill, I., and Roy, R. (2003). Generation of nondiffracting Bessel beams by use of a spatial light modulator. *Optics Letters*, 28(22):2183.

**[Chichkov et al., 1996]** Chichkov, B. N., Momma, C., Nolte, S., Von Alvensleben, F., and Tünnermann, A. (1996). Femtosecond, picosecond and nanosecond laser ablation of solids. *Applied physics A*, 63(2):109–115.

**[Clerici et al., 2015]** Clerici, M., Hu, Y., Lassonde, P., Milian, C., Couairon, A., Christodoulides, D. N., Chen, Z., Razzari, L., Vidal, F., Legare, F., Faccio, D., and Morandotti, R. (2015). Laser-assisted guiding of electric discharges around objects. *Science Advances*, 1(5):e1400111–e1400111.

**[Couairon et al., 2011]** Couairon, A., Brambilla, E., Corti, T., Majus, D., de J. Ramírez-Góngora, O., and Kolesik, M. (2011). Practitioner’s guide to laser pulse propagation models and simulation. *The European Physical Journal Special Topics*, 199(1):5–76.

**[Couairon and Mysyrowicz, 2007]** Couairon, A. and Mysyrowicz, A. (2007). Femtosecond filamentation in transparent media. *Physics Reports*, 441(2-4):47–189.

**[Dausinger et al., 2004]** Dausinger, F., Lichtner, F., and Lubatschowski, H. (2004). *Femtosecond technology for technical and medical applications*, volume 96. Springer Science & Business Media.

**[Davis et al., 1993]** Davis, J. A., Guertin, J., and Cottrell, D. M. (1993). Diffraction-free beams generated with programmable spatial light modulators. *Applied optics*, 32(31):6368–6370.

**[Davis et al., 1996]** Davis, K. M., Miura, K., Sugimoto, N., and Hirao, K. (1996). Writing waveguides in glass with a femtosecond laser. *Optics letters*, 21(21):1729–1731.

**[del Hoyo et al., 2020]** del Hoyo, J., Meyer, R., Furfaro, L., and Courvoisier, F. (2020). Nanoscale confinement of energy deposition in glass by double ultrafast Bessel pulses. *Nanophotonics*, 10(3):1089–1097.

**[Denisov, 1957]** Denisov, N. (1957). On a singularity of the field on an electromagnetic wave propagated in an inhomogeneous plasma. *Journal of Experimental and Theoretical Physics*, 4(4):544.

**[Drevinskas and Kazansky, 2017]** Drevinskas, R. and Kazansky, P. G. (2017). High-performance geometric phase elements in silica glass. *APL Photonics*, 2(6):066104.

**[Dudley et al., 2013]** Dudley, A., Li, Y., Mhlanga, T., Escuti, M., and Forbes, A. (2013). Generating and measuring nondiffracting vector bessel beams. *Optics letters*, 38(17):3429–3432.

**[Durfee et al., 1995]** Durfee, C. G., Lynch, J., and Milchberg, H. M. (1995). Development of a plasma waveguide for high-intensity laser pulses. *Physical Review E*, 51(3):2368–2389.

**[Durnin et al., 1987]** Durnin, J., Miceli, J. J., and Eberly, J. H. (1987). Diffraction-free beams. *Physical Review Letters*, 58(15):1499–1501.

**[Dusser et al., 2010]** Dusser, B., Sagan, Z., Soder, H., Faure, N., Colombier, J.-P., Jourlin, M., and Audouard, E. (2010). Controlled nanostructrures formation by ultra fast laser pulses for color marking. *Optics express*, 18(3):2913–2924.

**[Eliezer, 2002]** Eliezer, S. (2002). *The Interaction of High-Power Lasers with Plasmas*. CRC Press, 1st edition.

**[Emmony et al., 1973]** Emmony, D., Howson, R., and Willis, L. (1973). Laser mirror damage in germanium at 10.6 $\mu$m. *Applied Physics Letters*, 23(11):598–600.

**[Florea and Winick, 2003]** Florea, C. and Winick, K. A. (2003). Fabrication and characterization of photonic devices directly written in glass using femtosecond laser pulses. *Journal of lightwave technology*, 21(1):246–253.

**[Forslund et al., 1975]** Forslund, D., Kindel, J., Lee, K., Lindman, E., and Morse, R. (1975). Theory and simulation of resonant absorption in a hot plasma. *Physical Review A*, 11(2):679.

**[Froehly et al., 2014]** Froehly, L., Jacquot, M., Lacourt, P. A., Dudley, J. M., and Courvoisier, F. (2014). Spatiotemporal structure of femtosecond Bessel beams from spatial light modulators. *Journal of the Optical Society of America A*, 31(4):790.

**[Gattass and Mazur, 2008]** Gattass, R. R. and Mazur, E. (2008). Femtosecond laser micromachining in transparent materials. *Nature Photonics*, 2(4):219–225.

**[Groothoff et al., 2015]** Groothoff, N., Hongler, M.-O., Kazansky, P., and Bellouard, Y. (2015). Transition and self-healing process between chaotic and self-organized patterns observed during femtosecond laser writing. *Optics Express*, 23(13):16993–17007.

**[Grunwald et al., 2004]** Grunwald, R., Neumann, U., Kebbel, V., Kühn, H.-J., Mann, K., Leinhos, U., Mischke, H., and Wulff-Molder, D. (2004). Vacuum-ultraviolet beam array generation by flat micro-optical structures. *Optics Letters*, 29(9):977.

**[Guo et al., 2004]** Guo, H., Jiang, H., Fang, Y., Peng, C., Yang, H., Li, Y., and Gong, Q. (2004). The pulse duration dependence of femtosecond laser induced refractive index modulation in fused silica. *Journal of Optics A: Pure and Applied Optics*, 6(8):787.

**[Hayasaki et al., 2017]** Hayasaki, Y., Fukuda, S. I., Hasegawa, S., and Juodkazis, S. (2017). Two-color pump-probe interferometry of ultra-fast light-matter interaction. *Scientific Reports*, 7.

**[Hernandez-Rueda et al., 2017]** Hernandez-Rueda, J., Clarijs, J., van Oosten, D., and Krol, D. M. (2017). The influence of femtosecond laser wavelength on waveguide fabrication inside fused silica. *Applied Physics Letters*, 110(16):161109.

**[Hnatovsky et al., 2006]** Hnatovsky, C., Taylor, R., Simova, E., Rajeev, P., Rayner, D., Bhardwaj, V., and Corkum, P. (2006). Fabrication of microchannels in glass using focused femtosecond laser radiation and selective chemical etching. *Applied Physics A*, 84(1):47–61.

**[Hora, 1986]** Hora, H. (1986). Y. r. shen, the principles of nonlinear optics, john wiley & sons, new york, 1984, 576 pages. *Laser and Particle Beams*, 4(2):318–319.

**[Iwasaki et al., 2003]** Iwasaki, A., Aközbek, N., Ferland, B., Luo, Q., Roy, G., Bowden, C., and Chin, S. (2003). A LIDAR technique to measure the filament length generated by a high-peak power femtosecond laser pulse in air. *Applied Physics B: Lasers and Optics*, 76(3):231–236.

**[Jain et al., 1981]** Jain, A. K., Kulkarni, V., Sood, D., and Uppal, J. (1981). Periodic surface ripples in laser-treated aluminum and their use to determine absorbed power. *Journal of Applied Physics*, 52(7):4882–4884.

**[Jarutis et al., 2000]** Jarutis, V., Paškauskas, R., and Stabinis, A. (2000). Focusing of Laguerre–Gaussian beams by axicon. *Optics Communications*, 184(1-4):105–112.

**[Juodkazis et al., 2006]** Juodkazis, S., Nishimura, K., Tanaka, S., Misawa, H., Gamaly, E. G., Luther-Davies, B., Hallo, L., Nicolai, P., and Tikhonchuk, V. T. (2006). Laser-induced microexplosion confined in the bulk of a sapphire crystal: Evidence of multimegabar pressures. *Physical Review Letters*, 96(16):166101.

**[Karimelahi et al., 2013]** Karimelahi, S., Abolghasemi, L., and Herman, P. R. (2013). Rapid micromachining of high aspect ratio holes in fused silica glass by high repetition rate picosecond laser. *Applied Physics A*, 114(1):91–111.

**[Kazansky et al., 1999]** Kazansky, P., Inouye, H., Mitsuyu, T., Miura, K., Qiu, J., Hirao, K., and Starrost, F. (1999). Anomalous anisotropic light scattering in ge-doped silica glass. *Physical Review Letters*, 82(10):2199.

**[Kazansky et al., 2007]** Kazansky, P. G., Yang, W., Bricchi, E., Bovatsek, J., Arai, A., Shimotsuma, Y., Miura, K., and Hirao, K. (2007). "quill" writing with ultrashort light pulses in transparent materials. *Applied physics letters*, 90(15):151120.

**[Kelley, 1965]** Kelley, P. (1965). Self-focusing of optical beams. *Physical Review Letters*, 15(26):1005.

**[Komatsu and Honma, 2019]** Komatsu, T. and Honma, T. (2019). Laser patterning and growth mechanism of orientation designed crystals in oxide glasses: A review. *Journal of Solid State Chemistry*, 275:210–222.

**[Kruer, 2003]** Kruer, W. (2003). *Physics of laser plasma interactions*. CRC Press.

**[Lancry et al., 2013]** Lancry, M., Poumellec, B., Canning, J., Cook, K., Poulin, J.-C., and Brisset, F. (2013). Ultrafast nanoporous silica formation driven by femtosecond laser irradiation. *Laser & Photonics Reviews*, 7(6):953–962.

**[Lapointe, 1992]** Lapointe, M. (1992). Review of non-diffracting bessel beam experiments. *Optics & Laser Technology*, 24(6):315–321.

**[Li et al., 2016]** Li, P., Zhang, Y., Liu, S., Han, L., Cheng, H., Yu, F., and Zhao, J. (2016). Quasi-bessel beams with longitudinally varying polarization state generated by employing spectrum engineering. *Optics Letters*, 41(20):4811–4814.

**[Liao et al., 2015]** Liao, Y., Ni, J., Qiao, L., Huang, M., Bellouard, Y., Sugioka, K., and Cheng, Y. (2015). High-fidelity visualization of formation of volume nanogratings in porous glass by femtosecond laser irradiation. *Optica*, 2(4):329–334.

**[Lü et al., 2020]** Lü, J.-Q., Wang, X.-L., Zhang, G.-L., Tu, C., Li, Y., and Wang, H.-T. (2020). Bessel-like beams with controllable rotating local linear polarization during propagation. *Optics Letters*, 45(7):1738–1741.

**[Luo et al., 2001]** Luo, L., Wang, D., Li, C., Jiang, H., Yang, H., and Gong, Q. (2001). Formation of diversiform microstructures in wide-bandgap materials by tight-focusing femtosecond laser pulses. *Journal of Optics A: Pure and Applied Optics*, 4(1):105–110.

**[Mao et al., 2004]** Mao, S., Quéré, F., Guizard, S., Mao, X., Russo, R., Petite, G., and Martin, P. (2004). Dynamics of femtosecond laser interactions with dielectrics. *Applied Physics A: Solids and Surfaces*, 79(7):1695–1709.

**[Meyer, 2020]** Meyer, R. (2020). *Contrôle du dépôt d'énergie par laser femtoseconde dans les diélectriques par faisceaux de Bessel : profil spatio-temporel de densité plasma et applications au clivage du verre.* Theses, Université Bourgogne Franche-Comté.

**[Meyer et al., 2019]** Meyer, R., Froehly, L., Giust, R., Hoyo, J. D., Furfaro, L., Billet, C., and Courvoisier, F. (2019). Extremely high-aspect-ratio ultrafast Bessel beam generation and stealth dicing of multi-millimeter thick glass. *Applied Physics Letters*, 114(20):201105.

**[Meyer et al., 2017]** Meyer, R., Giust, R., Jacquot, M., Dudley, J. M., and Courvoisier, F. (2017). Submicron-quality cleaving of glass with elliptical ultrafast Bessel beams. *Applied Physics Letters*, 111(23):231108.

**[Milione et al., 2014]** Milione, G., Dudley, A., Nguyen, T. A., Chakraborty, O., Karimi, E., Forbes, A., and Alfano, R. R. (2014). Experimental measurement of the self-healing of the spatially inhomogeneous states of polarization of radially and azimuthally polarized vector bessel beams. *arXiv preprint arXiv:1412.2722*.

**[Mills et al., 2002]** Mills, J. D., Kazansky, P. G., Bricchi, E., and Baumberg, J. J. (2002). Embedded anisotropic microreflectors by femtosecond-laser nanomachining. *Applied physics letters*, 81(2):196–198.

**[Mitra et al., 2015]** Mitra, S., Chanal, M., Clady, R., Mouskeftaras, A., and Grojo, D. (2015). Millijoule femtosecond micro-Bessel beams for ultra-high aspect ratio machining. *Applied Optics*, 54:7358.

**[Mitri, 2008]** Mitri, F. (2008). Acoustic scattering of a high-order bessel beam by an elastic sphere. *Annals of Physics*, 323(11):2840–2850.

**[Miura et al., 2000]** Miura, K., Qiu, J., Mitsuyu, T., and Hirao, K. (2000). Space-selective growth of frequency-conversion crystals in glasses with ultrashort infrared laser pulses. *Optics letters*, 25(6):408–410.

**[Momma et al., 1996]** Momma, C., Chichkov, B. N., Nolte, S., von Alvensleben, F., Tünnermann, A., Welling, H., and Wellegehausen, B. (1996). Short-pulse laser ablation of solid targets. *Optics communications*, 129(1-2):134–142.

**[Moreno et al., 2015]** Moreno, I., Davis, J. A., Sánchez-López, M. M., Badham, K., and Cottrell, D. M. (2015). Nondiffracting bessel beams with polarization state that varies with propagation distance. *Optics letters*, 40(23):5451–5454.

**[Müller et al., 2017]** Müller, A., Wapler, M. C., and Wallrabe, U. (2017). Segmented bessel beams. *Optics Express*, 25(19):22640–22647.

**[Niv et al., 2004]** Niv, A., Biener, G., Kleiner, V., and Hasman, E. (2004). Propagation-invariant vectorial bessel beams obtained by use of quantized pancharatnam–berry phase optical elements. *Optics letters*, 29(3):238–240.

**[Nolte et al., 2013]** Nolte, S., Zimmermann, F., Richter, S., Plech, A., Peschel, U., and Tünnermann, A. (2013). Ultrashort pulse induced nanogratings. In *MATEC Web of Conferences*, volume 8, page 03001. EDP Sciences.

**[Ornigotti and Aiello, 2013]** Ornigotti, M. and Aiello, A. (2013). Radially and azimuthally polarized nonparaxial bessel beams made simple. *Optics express*, 21(13):15530–15537.

**[Ouadghiri Idrissi, 2018]** Ouadghiri Idrissi, I. (2018). *Nonlinear instabilities and filamentation of Bessel beams*. Theses, Université Bourgogne Franche-Comté.

**[Papazoglou et al., 2007]** Papazoglou, D. G., Zergioti, I., and Tzortzakis, S. (2007). Plasma strings from ultraviolet laser filaments drive permanent structural modifications in fused silica. *Optics Letters*, 32(14):2055.

**[Polesana et al., 2008]** Polesana, P., Franco, M., Couairon, A., Faccio, D., and Trapani, P. D. (2008). Filamentation in Kerr media from pulsed Bessel beams. *Physical Review A*, 77(4):043814.

**[Porras et al., 2004]** Porras, M. A., Parola, A., Faccio, D., Dubietis, A., and Trapani, P. D. (2004). Nonlinear unbalanced Bessel beams: Stationary conical waves supported by nonlinear losses. *Physical Review Letters*, 93(15).

**[Poumellec et al., 2011]** Poumellec, B., Lancry, M., Chahid-Erraji, A., and Kazansky, P. G. (2011). Modification thresholds in femtosecond laser processing of pure silica: review of dependencies on laser parameters. *Optical Materials Express*, 1(4):766–782.

**[Poumellec et al., 2008]** Poumellec, B., Lancry, M., Poulin, J.-C., and Ani-Joseph, S. (2008). Non reciprocal writing and chirality in femtosecond laser irradiated silica. *Optics express*, 16(22):18354–18361.

**[Rapp et al., 2016]** Rapp, L., Meyer, R., Giust, R., Furfaro, L., Jacquot, M., Lacourt, P. A., Dudley, J. M., and Courvoisier, F. (2016). High aspect ratio micro-explosions in the bulk of sapphire generated by femtosecond Bessel beams. *Scientific Reports*, 6(1):34286.

**[Rethfeld et al., 2017]** Rethfeld, B., Ivanov, D. S., Garcia, M. E., and Anisimov, S. I. (2017). Modelling ultrafast laser ablation. *Journal of Physics D: Applied Physics*, 50(19):193001.

**[Richter et al., 2012]** Richter, S., Heinrich, M., Döring, S., Tünnermann, A., Nolte, S., and Peschel, U. (2012). Nanogratings in fused silica: Formation, control, and applications. *Journal of Laser Applications*, 24(4):042008.

**[Richter et al., 2015]** Richter, S., Zimmermann, F., Eberhardt, R., Tünnermann, A., and Nolte, S. (2015). Toward laser welding of glasses without optical contacting. *Applied Physics A*, 121(1):1–9.

**[Sakabe et al., 2009]** Sakabe, S., Hashida, M., Tokita, S., Namba, S., and Okamuro, K. (2009). Mechanism for self-formation of periodic grating structures on a metal surface by a femtosecond laser pulse. *Physical Review B*, 79(3):033409.

**[Salter and Booth, 2012]** Salter, P. and Booth, M. (2012). Dynamic control of directional asymmetry observed in ultrafast laser direct writing. *Applied Physics Letters*, 101(14):141109.

**[Sanner et al., 2007]** Sanner, N., Huot, N., Audouard, E., Larat, C., and Huignard, J.-P. (2007). Direct ultrafast laser micro-structuring of materials using programmable beam shaping. *Optics and Lasers in Engineering*, 45(6):737–741.

**[Self, 1983]** Self, S. A. (1983). Focusing of spherical gaussian beams. *Appl. Opt.*, 22(5):658–661.

**[Shen, 1975]** Shen, Y. (1975). Self-focusing: Experimental. *Progress in Quantum Electronics*, 4:1–34.

**[Shen, 1984]** Shen, Y.-R. (1984). The principles of nonlinear optics, john wiley & sons, new york, 1984, 576 pages. *Laser and Particle Beams*, 4(2):318–319.

**[Shimotsuma et al., 2003]** Shimotsuma, Y., Kazansky, P. G., Qiu, J., and Hirao, K. (2003). Self-organized nanogratings in glass irradiated by ultrashort light pulses. *Physical review letters*, 91(24):247405.

**[Somayaji et al., 2020]** Somayaji, M., Bhuyan, M. K., Bourquard, F., Velpula, P. K., D'Amico, C., Colombier, J. P., and Stoian, R. (2020). Multiscale electronic and thermomechanical dynamics in ultrafast nanoscale laser structuring of bulk fused silica. *Scientific Reports*, 10:15152.

**[Sowa et al., 2005]** Sowa, S., Watanabe, W., Nishii, J., and Itoh, K. (2005). Filamentary cavity formation in poly(methyl methacrylate) by single femtosecond pulse. *Applied Physics A*, 81(8):1587–1590.

**[Stalder and Schadt, 1996]** Stalder, M. and Schadt, M. (1996). Linearly polarized light with axial symmetry generated by liquid-crystal polarization converters. *Optics letters*, 21(23):1948–1950.

**[Sudrie et al., 2002]** Sudrie, L., Couairon, A., Franco, M., Lamouroux, B., Prade, B., Tzortzakis, S., and Mysyrowicz, A. (2002). Femtosecond laser-induced damage and filamentary propagation in fused silica. *Physical Review Letters*, 89(18):4135.

**[Sugioka and Cheng, 2014]** Sugioka, K. and Cheng, Y. (2014). Ultrafast lasers—reliable tools for advanced materials processing. *Light: Science & Applications*, 3(4):e149–e149.

**[Tervo and Turunen, 2001]** Tervo, J. and Turunen, J. (2001). Generation of vectorial propagation-invariant fields by polarization-grating axicons. *Optics communications*, 192(1-2):13–18.

**[Tian, 2020]** Tian, J. (2020). *Femtosecond laser direct writing of circular optical properties in silica glass*. Theses, Université Paris-Saclay.

**[Tičkūnas et al., 2017]** Tičkūnas, T., Perrenoud, M., Butkus, S., Gadonas, R., Rekštytė, S., Malinauskas, M., Paipulas, D., Bellouard, Y., and Sirutkaitis, V. (2017). Combination of additive and subtractive laser 3d microprocessing in hybrid glass/polymer microsystems for chemical sensing applications. *Optics express*, 25(21):26280–26288.

**[Tiwari et al., 2012]** Tiwari, S. K., Mishra, S. R., Ram, S. P., and Rawat, H. S. (2012). Generation of a bessel beam of variable spot size. *Applied Optics*, 51(17):3718–3725.

**[Tzortzakis et al., 2006]** Tzortzakis, S., Papazoglou, D. G., and Zergioti, I. (2006). Long-range filamentary propagation of subpicosecond ultraviolet laser pulses in fused silica. *Optics Letters*, 31(6):796.

**[Tzortzakis et al., 2001]** Tzortzakis, S., Sudrie, L., Franco, M., Prade, B., Mysyrowicz, A., Couairon, A., and Bergé, L. (2001). Self-guided propagation of ultrashort IR laser pulses in fused silica. *Physical Review Letters*, 87(21):213902.

**[Vitek et al., 2010]** Vitek, D. N., Adams, D. E., Johnson, A., Tsai, P. S., Backus, S., Durfee, C. G., Kleinfeld, D., and Squier, J. A. (2010). Temporally focused femtosecond laser pulses for low numerical aperture micromachining through optically transparent materials. *Optics Express*, 18(17):18086.

**[Vogel et al., 2008]** Vogel, A., Linz, N., Freidank, S., and Paltauf, G. (2008). Femtosecond-laser-induced nanocavitation in water: Implications for optical breakdown threshold and cell surgery. *Physical Review Letters*, 100(3).

**[Xie et al., 2016]** Xie, C., Giust, R., Zhang, J., Jukna, V., Meyer, R., Furfaro, L., Jacquot, M., Froehly, L., Dudley, J. M., Couairon, A., et al. (2016). Enhanced absorption and plasmon excitation in the bulk of fused silica with femtosecond bessel beams. In *CLEO: Science and Innovations*, pages STh3Q–2. Optical Society of America.

**[Xie et al., 2015]** Xie, C., Jukna, V., Milián, C., Giust, R., Ouadghiri-Idrissi, I., Itina, T., Dudley, J. M., Couairon, A., and Courvoisier, F. (2015). Tubular filamentation for laser material processing. *Scientific Reports*, 5:8914.

**[Xie et al., 2021]** Xie, C., Meyer, R., Froehly, L., Giust, R., and Courvoisier, F. (2021). In-situ diagnostic of femtosecond laser probe pulses for high resolution ultrafast imaging. *Light: Science & Applications*, 10(1):1–13.

**[Yanik et al., 2004]** Yanik, M. F., Cinar, H., Cinar, H. N., Chisholm, A. D., Jin, Y., and Ben-Yakar, A. (2004). Functional regeneration after laser axotomy. *Nature*, 432(7019):822–822.

**[Yu et al., 2015]** Yu, Y., Jiang, L., Cao, Q., Xia, B., Wang, Q., and Lu, Y. (2015). Pump-probe imaging of the fs-ps-ns dynamics during femtosecond laser bessel beam drilling in pmma. *Optics Express*, 23(25):32728–32735.

**[Zhang et al., 2013]** Zhang, F., Yu, Y., Cheng, C., Dai, Y., and Qiu, J. (2013). Fabrication of polarization-dependent light attenuator in fused silica using a low-repetition-rate femtosecond laser. *Optics Letters*, 38(13):2212–2214.

**[Zhang et al., 2014a]** Zhang, F., Zhang, H., Dong, G., and Qiu, J. (2014a). Embedded nanogratings in germanium dioxide glass induced by femtosecond laser direct writing. *JOSA B*, 31(4):860–864.

**[Zhang et al., 2014b]** Zhang, J., Gecevičius, M., Beresna, M., and Kazansky, P. G. (2014b). Seemingly unlimited lifetime data storage in nanostructured glass. *Physical review letters*, 112(3):033901.

**[Zhu et al., 2007]** Zhu, B., Dai, Y., Ma, H., Zhang, S., Lin, G., and Qiu, J. (2007). Femtosecond laser induced space-selective precipitation of nonlinear optical crystals in rare-earth-doped glasses. *Optics Express*, 15(10):6069–6074.

Document generated with LaTeX and:
the LaTeX style for PhD Thesis created by S. Galland — http://www.multiagent.fr/ThesisStyle
the tex-upmethodology package suite — http://www.arakhne.org/tex-upmethodology/